

Functional metal-organic framework based separator for  
lithium-sulfur batteries

Graduate School of Systems and Information Engineering  
University of Tsukuba

March 2017

Bai Songyan

Functional metal-organic framework based separator for  
lithium-sulfur batteries

March 2017

Bai Songyan

## ABSTRACT

A novel Metal-Organic Frameworks (MOF) based separator is designed for lithium-sulfur batteries. More importantly, these perfectly high-ordered micropores ( $\sim 9 \text{ \AA}$ ) are significantly smaller than the diameters of lithium polysulfide ( $\text{Li}_2\text{S}_n$ ,  $4 < n \leq 8$ ). On the basis of the open metal sites with ligand's functional groups, the infiltrating metal-organic compounds can act as a high-efficient selective carrier, displaying outstanding molecular/ionic transferring capability in lithium-sulfur battery. The self-assembly Cu(II)/Zn(II)-based MOF@GO separator inserted between the sulfur cathode and lithium metal anode has been assembled. This dissertation originally explores a series of novel MOF@GO separators which has been designed to function towards the dissolved polysulfide ions migrating to the anode and further enhance its cycling performance in lithium-sulfur batteries.

The Zn(II) metal-organic framework (MOF) based separator for lithium-sulfur batteries is able to play an efficient role as an ionic sieve for the soluble polysulfide ions. More importantly, when a sulfur-containing mesoporous carbon material (approximately 70 wt% sulfur content) is used as a cathode composite without elaborate synthesis or surface modification, the battery with Zn(II)-MOF based separator exhibited much lower capacity decay of 0.041% per cycle at 1C over 1000 cycles.

In addition, a Cu(II)-metal-organic framework (MOF)-based battery separator has been designed to act as an ionic sieve in lithium-sulfur batteries, which selectively sieves  $\text{Li}^+$  ions while efficiently suppressing undesired polysulfides migrating to the anode side. A lithium-sulfur battery with a Cu(II)-MOF-based separator exhibits a low capacity decay rate (0.019% per cycle over 1,500 cycles). Moreover, there is almost no capacity fading after the initial 100 cycles. Our approach demonstrates the potential for MOF-based materials as separators for energy-storage applications.

## TABLE OF CONTENTS

ABSTRACT.....	III
TABLE OF CONTENTS.....	IV
LIST OF FIGS.....	VII
Chapter 1. General Introduction .....	1
1.1 Lithium-sulfur battery.....	1
1.1.1 Advantages of lithium-sulfur battery .....	1
1.1.2 Mechanism of lithium-sulfur battery .....	2
1.2 The challenges of lithium-sulfur batteries .....	5
1.2.1 Demerits of sulfur .....	5
1.2.2 Demerits of the intermediate lithium polysulfide .....	5
1.2.3 Shuttle effects.....	5
1.2.4 Electrolyte for lithium-sulfur batteries.....	5
1.3 Cathode design for lithium-sulfur batteries .....	9
1.3.1 Porous carbon as sulfur host .....	10
1.3.2 Carbon nanotube (CNTs) as sulfur host.....	11
1.3.3 Graphene as sulfur host.....	13
1.3.4 Polymer coating as sulfur host.....	15
1.3.5 Oxide materials as additive .....	16
1.4 Functional separator for lithium-sulfur batteries .....	18
1.4.1 Porous carbon paper as separator.....	18
1.4.2 Graphene oxide paper as separator .....	18
1.4.3 Conductive carbon coating on the Celgard separator .....	20
1.4.4 Coating graphene on polypropylene-supported separator .....	20
1.5 Metal-organic frameworks based separator .....	21
1.5.1 The chemical affiliation of Metal-organic frameworks .....	22
1.5.2 The porosity of Metal-organic frameworks .....	23
1.5.3 The ionic sieving effects of MOF based materials .....	25
1.5.4 The MOF based separator for lithium-sulfur batteries.....	26

1.6 Reference .....	28
Chapter 2. A zinc(II)-metal-organic framework based separator.....	33
2.1 Introduction.....	33
2.2 Experiment and Characterization.....	35
2.2.1 Chemicals.....	35
2.2.2 Preparation of Sulfur cathode (CMK-3@S) .....	35
2.2.3 The Fabrication of coin cells and CV measurement in lithium-sulfur batteries .....	40
2.2.4 Characterization .....	38
2.2.5 Fabrication process of Zn(II)-MOF@GO separator .....	38
2.2.6 Permeation experiments of Zn(II)-MOF@GO separator.....	39
2.3 Results and Discussion .....	42
2.3.1 Confirmation of MOF particles .....	40
2.3.2 Electrochemical stability of Zn-MOF@GO separator.....	41
2.3.3 Molecular properties of Zn-MOF@GO separator .....	42
2.3.4 Electrochemical performance .....	47
2.3.5 Further characterization of the MOF@GO separators.....	49
2.4 Conclusions.....	54
2.5 References.....	55
Chapter 3. A Cu(II)-Metal-Organic Framework-Based Separator.....	58
3.1 Introduction.....	58
3.2 Experiment and Characterization.....	60
3.2.1 Chemicals.....	60
3.2.2 The Fabrication of coin cells and CV measurement in lithium-sulfur batteries .....	60
3.2.3 Characterization of the MOF@GO separator .....	61
3.2.4 Fabrication of Cu(II)-MOF@GO separator .....	62
3.2.5 Permeation experiments.....	64
3.3 Results and Discussion .....	66
3.3.1 Porosity of MOF@GO separator .....	66

3.3.2 Electrochemical stability with/without MOF@GO separator .....	68
3.3.3 Electrochemical stability at different scanning rates .....	70
3.3.4 Ion conductivity of MOF@GO separator .....	74
3.3.5 Stability of MOF@GO separator .....	76
3.3.6 Electrochemical performance .....	82
3.3.7 Further characterization of the MOF@GO separators.....	87
3.4 Conclusions.....	89
3.5 References.....	91
Chapter 4 Conclusions .....	94
Appendix.....	97
List of Research Results.....	99
Acknowledgements.....	100

## LIST OF FIG.S

Fig.1.1. Energy density comparison of commercial lithium-ion batteries and next-generation lithium-sulfur batteries.....	1
Fig.1.2. Electrochemical mechanism of rechargeable lithium-sulfur batteries.....	2
Fig.1.3. The serial electrochemical intermediates at different Discharge/charge stage.....	3
Fig.1.4. The side reaction between the dissolved polysulfide intermediates and traditional carbonate electrolytes.....	7
Fig.1.5. The CMK-3 as the sulfur carrier (a) and the discharge/charge curves of recharge lithium-sulfur batteries (b).....	10
Fig.1.6. The microporous carbon coating on CNT as the sulfur carrier for rechargeable lithium-sulfur batteries.....	11
Fig.1.7. The Graphene coating on the sulfur particles for rechargeable lithium-sulfur batteries.....	13
Fig.1.8. The 3D-Graphene frameworks as the sulfur carrier for rechargeable lithium-sulfur batteries.....	14
Fig.1.9. The TiO <sub>2</sub> coating on the surface of nanosized sulfur particles for rechargeable lithium-sulfur batteries.....	16
Fig.1.10. The Mxene nanosheets as the sulfur carrier for rechargeable lithium-sulfur batteries.....	16
Fig.1.11. The microporous carbon paper as the separator for rechargeable lithium-sulfur batteries.....	17
Fig.1.12. The graphene oxide membrane as the separator for rechargeable lithium-sulfur batteries.....	18
Fig.1.13. The Super-P conductive carbon coating on the Celgard separator for rechargeable lithium-sulfur batteries.....	19
Fig.1.14. The Graphene coating on the polypropylene separator for rechargeable lithium-sulfur batteries.....	20
Fig.1.15. The different coordination mode between the organic ligand and metal	

centers in metal-organic frameworks.....	21
Fig.1.16. The tunable porous structures with different organic ligand in metal-organic frameworks.....	23
Fig.1.17. The simplified different coordination mode (Topo structures) in metal-organic frameworks.....	24
Fig.1.18. The anion sensing MOF with visual colorimetric responses to a series of anions.....	25
Fig.2.1. Synthesizing process of sulfur cathode materials (CMK-3@S sulfur cathode materials).....	35
Fig.2.2. Thermogravimetric analysis. The wt% of sulfur in the CMK-3/S composite was determined to ~70%, respectively.....	36
Fig.2.3. The fabrication of 2032-coin cell in lithium-sulfur batteries.....	37
Fig.2.4. Fabrication process of Zn(II)-MOF@GO separators.....	37
Fig.2.5. (a) Digital photo of upper GO laminates. The inset shows a SEM image along the GO side. (Scale bar, 250 nm). (b) Digital photo of cross-section Zn-based MOF@GO separator. The inset shows a SEM image along the MOF side. (Scale bar, 5 $\mu$ m); (c) The permeation mode with the separator.....	38
Fig.2.6. (a) The permeation with the pristine separators (Celgard 2400 separator); (b) The permeation with the MOF@GO separators.....	39
Fig.2.7. The PXRD patterns of MOF@GO separators. The MOF structural skeleton remains intact during the discharge/charge process over 100 cycles.....	41
Fig.2.8. The CVs in lithium sulfur batteries with (a) a MOF@GO separator at a scan rate of 0.1 mV s <sup>-1</sup> and (b) a pristine separator (Celgard 2400) at a scan rate of 0.1 mV s <sup>-1</sup> .....	42
Fig.2.9. The analyses based on the IR spectra. (a) Before/after the electrochemical process, the IR spectra of the dehydrated MOF particles. (b) The IR spectra have been measured in the higher wavenumbers.....	44
Fig.2.10. Electrochemical performance of the lithium-sulfur cells. (a) Discharge capacity and Coulombic efficiency at the current rate of 0.5C over 350 cycles. (b) Discharge capacity and Coulombic efficiency at the current rate of 1 C over 1,000	

cycles. (c) The voltage profiles at the rate of 1 C at the 1st, 100th, 400th, 800th and 1000th cycle, respectively.....	47
Fig.2.11. The discharge/charge curves at C/10 and 1C with Zn-MOF@GO separators in lithium-sulfur batteries.....	48
Fig.2.12. SEM images of the lithium-metal surface before cycling (a) and after 1000 cycles (c). Photographs of lithium anode before cycling (b) and after 1000 cycles (d) in lithium-sulfur batteries.....	49
Fig.2.13. Schematic of the Zn-based MOF@GO separator. The atomic stack (Right) illustrates the micropores.....	51
Fig.2.14. SEM images of the GO laminates in MOF@GO separator. (After 100 <sup>th</sup> charge/discharge cycles with GO separator) .....	52
Fig.3.1. The fabrication of 2032-coin cell in lithium-sulfur batteries.....	57
Fig.3.2. Fabrication and Structural characteristics of MOF@GO separators. (a) Schematic of the fabrication process of MOF@GO separators. (b) An illustration of the microporous crystalline structures (HKUST-1). (c) The PXRD patterns of MOF@GO separators. (d) The SEM image of the multilayered MOF@GO separator. The inset shows a digital photo along the MOF side. (e) The SEM image of the GO layer.....	61
Fig.3.3. Polysulfide permeation measurements. (a) V-type permeation device with a MOF@GO separator. (b) The V-type permeation device with a GO separator. (c) The permeation mode with the separators.....	63
Fig.3.4. Nitrogen sorption data for MOF@GO separators. N <sub>2</sub> sorption isotherm at 77 K and its analytical pore size distribution.....	65
Fig.3.5. Nitrogen sorption data for MOF@GO separators. N <sub>2</sub> sorption isotherm at 77 K and its analytical pore size distribution. Follow the calculation of the non-local density functional theory (NLDFT) model.....	66
Fig.3.6. (a) CV profiles with a pristine separator at a scan rate of 0.1 mV s <sup>-1</sup> , (b) CV profiles with a MOF@GO separator at a scan rate of 0.1 mV s <sup>-1</sup> .....	67
Fig.3.7. CVs at different scan rates of lithium sulfur batteries. (a) With the pristine separators (Celgard) in lithium sulfur batteries. (b) With Cu(II)-based MOF@GO	

separators in lithium sulfur batteries. (c) The linear fits of the peak currents for the lithium sulfur batteries with/without MOF@GO separators.....71

Fig.3.8. Electrical impedance spectra of (a) Celgard (b) MOF@GO separator. Ion conductivity of (c) Celgard (d) MOF@GO separator.....73

Fig.3.9. The analyses based on the IR and solid UV-Vis spectra. (a) Before the electrochemical process, the IR spectra of the dehydrated MOF particles. (b) After the process over 100 charge/ discharge cycles, the IR spectra of the MOF particles have been measured. (c) The UV-Vis spectra of the MOF particles have illustrated no obvious changes before/after the charge/discharge process over 100 cycles.....75

Fig.3.10. (a) The structural properties of binuclear Cu(II) paddlewheel subunits. (b) The presentation of the dehydration process (removing the water in cavities) and the weak interaction between the restricted open metal sites and polysulfide ions.....78

Fig.3.11. Electrochemical performance of lithium-sulfur batteries. (a) Discharge capacity and coulombic efficiency at the rate of C/2 over 500 cycles with MOF@GO separators. (b) Cycling performance at the rate of 1 C over 1,500 cycles with MOF@GO separators and over 1,000 cycles with GO separators. (c) Discharge/charge voltage profiles at the rate of C/2 with MOF@GO separators. The specific capacities of the cathode are calculated based on the mass of sulfur.....82

Fig.3.12. Rate performance and voltage profiles of lithium-sulfur batteries. (a) Rate performance with MOF@GO and GO separators at various C-rates from C/5 to 3 C. The discharge/charge voltage profiles for batteries with (b) the MOF@GO separator and (c) the GO separator at different current densities. ....83

Fig.3.13. Schematic of MOF@GO separators in lithium-sulfur batteries. The MOF@GO separator acts as an ionic sieve towards the soluble polysulfides. The enlarged image illustrates the MOF pore size (approximately 9 Å), which is reasonably smaller than that of polysulfides ( $\text{Li}_2\text{S}_n$ ,  $4 < n \leq 8$ ).....86

# Chapter 1. General Introduction

## 1.1 Lithium-sulfur battery

### 1.1.1 Advantages of lithium-sulfur battery

Since the first practical lithium-ion (Li-ion) battery was commercialized by Sony company, the rechargeable batteries have been widely used and changed our daily life [1]. The emerging energetic demand has attracted a creasing number of interests in rechargeable batteries [2, 3]. Unlike the other industrial technology, battery industries have illustrated obvious trend of limited capacity enhancement and greatly giant demand from markets in recent decade [3, 4]. The progress in rechargeable batteries has continued bare step forward. On the basis of the mechanism of Li-ion battery, lithium intercalation reactions in transition metal oxides or metal phosphates or other cathode materials resulted in limited theoretical capacity. The significant limitation of cathode materials lies as an obstacle to develop traditional Li-ion battery technology with high energy density.

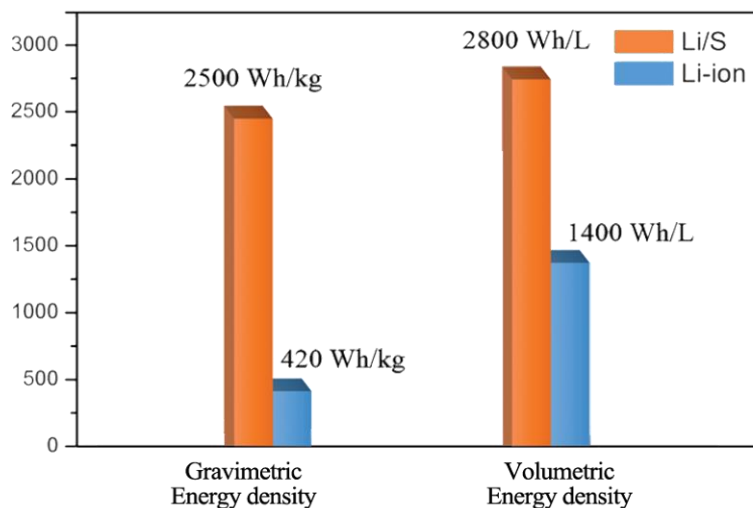


Fig. 1.1. Energy density comparison of commercial lithium-ion batteries and next-generation lithium-sulfur batteries [2].

Therefore, changing the current Li-on battery to other promising battery technology has been ascribed as an inevitable pathway to boost the next-generation batteries with high energy density. Serial criteria such as cost, efficiency, long-life

cycling, environmental friendliness and energy density also need to be considered in developing future electrical transportation and energy storage systems [5].

Lithium-sulfur(Li-S) batteries have a series of advantages among the next-generation battery technologies [6, 7]. There widely exists elemental sulfur in nature. The human beings also produced a huge amount of sulfur as byproducts in industries. Its value of cost/capacity (USD/kAh) can be as low as  $1.0 \times 10^{-3}$ . More important, its higher theoretical specific capacity of  $1,673 \text{ mAh g}^{-1}$  (calculated based on  $\text{S} \leftrightarrow \text{Li}_2\text{S}$ ) and the estimated energy density as high as  $\sim 2500 \text{ Wh kg}^{-1}$ , has far exceeded that of current lithium-ion batteries which has already approached to their theoretical limits [8]. Because of its vitally advantageous low cost, natural abundance, environmental friendliness, safer cut-off voltage range (1.5V ~ 3V) and high-energy density, lithium-sulfur (Li-S) batteries have been regarded as one of the most promising energy-storage candidates.

### 1.1.2 Mechanism of lithium-sulfur battery

Its electrochemical reactions in lithium-sulfur battery occurred between the sulfur cathode and the anode of metallic lithium [9, 10]. The overall redox reactions can be written as follows:

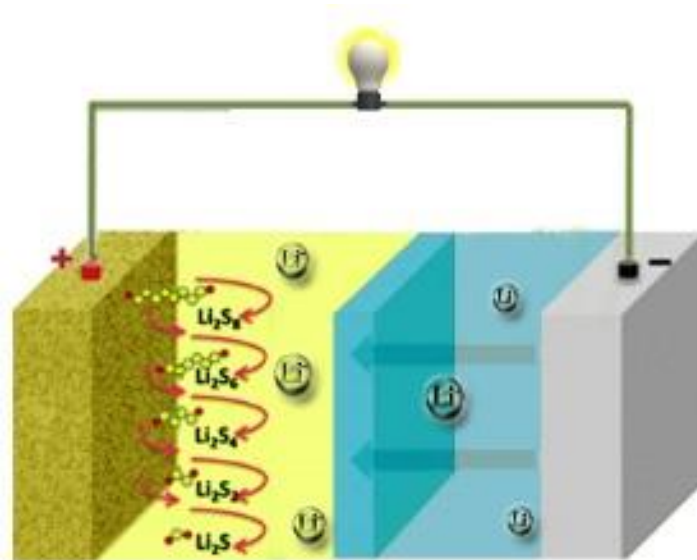
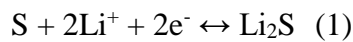


Fig. 1.2. Electrochemical mechanism of rechargeable lithium-sulfur batteries [9].

Its reduction/oxidation reaction responds to the electrochemical discharge process at the positive electrode and the charge process represents reversed oxidation/reduction reactions.

The current sulfur cathode of lithium-sulfur batteries can also be designed with the polysulfide ions ( $\text{Li}_2\text{S}_n$ ) as the sulfur source. After the initial charge process, the  $\text{Li}_2\text{S}_n$  was decomposed into elementary sulfur as the sulfur cathode. As depicted in Fig. 1.3, sulfur reacts with lithium ions ( $\text{Li}^+$ ) to form a series of intermediate polysulfide anions ( $\text{S}_n^{2-}$ ) in electrolyte. The electrochemical reactions experienced lithium polysulfide dissolving into electrolyte during cycling in lithium-sulfur batteries.

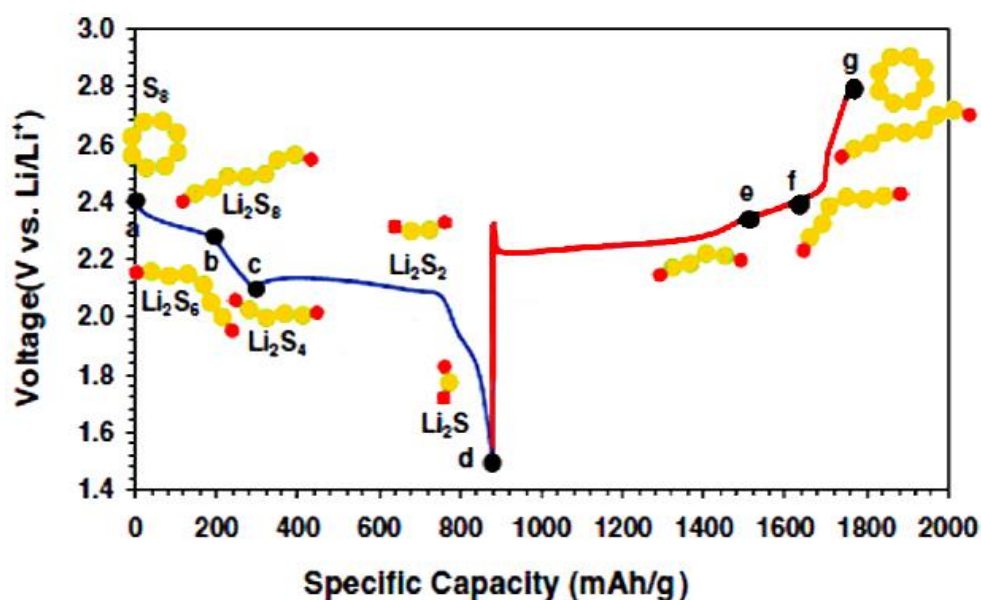


Fig. 1.3. The serial electrochemical intermediates at different discharge/charge process <sup>[10]</sup>.

A typical discharge curve (blue line) and charge curve (red line) are depicted, respectively. Cyclo- $\text{S}_8$  is the most stable allotropes of elemental sulfur in nature. Following its discharge curve, it can be divided into two predominant stages because of these intermediates with different solubility in electrolyte. Initially, the kinetics of reactions happened in the upper plateau ( $\text{S}_8 \leftrightarrow \text{Li}_2\text{S}_8$ ), in the inflection point ( $\text{Li}_2\text{S}_8 \leftrightarrow \text{Li}_2\text{S}_6$ ), and in the sloping region ( $\text{Li}_2\text{S}_6 \leftrightarrow \text{Li}_2\text{S}_4$ ), respectively, have been proved to be a fast electrochemical process. At the initial discharge curve, elemental sulfur combines with lithium ions and then converts into  $\text{Li}_2\text{S}_8$  and  $\text{Li}_2\text{S}_6$  because of these

intermediates with soluble capabilities in electrolyte. The solid sulfur witnessed continuously reduction and dissolution process in the electrolyte. More long-chain soluble polysulfide ( $\text{Li}_2\text{S}_n$ ,  $4 < n \leq 8$ ) ions have been produced and dissolved into the electrolyte, which further resulted from the increased viscosity of the electrolyte. Thereby, it further brings into a series of influence in the sloping region, such as declining voltages, lowering lithium ion transport, increasing impedance and concentration polarization (diffusion overpotential).

Next, the second-stage reactions happened at the lower plateau ( $\text{Li}_2\text{S}_4 \leftrightarrow \text{Li}_2\text{S}_2 \leftrightarrow \text{Li}_2\text{S}$ ) because of these insoluble intermediates. The final products of  $\text{Li}_2\text{S}$  was formed at the end of the discharge process. On the basis of the theoretical calculations, the intermediate  $\text{Li}_2\text{S}$  makes the predominant contributions to its capacity portions.

During the charge process, it experienced the converted electrochemical reactions. Firstly, there observed a rapid rise in the charge curves, representing the oxidation of  $\text{Li}_2\text{S}$  to  $\text{Li}_2\text{S}_2$ .

The following slight drop derives from their solubility difference. After that, the two flat and long plateaus are able to be observed, suggestive of the further oxidation of insoluble short-chain lithium polysulfide ( $\text{Li}_2\text{S}_n$ ,  $1 < n \leq 4$ ) to soluble long-chain lithium polysulfide ( $\text{Li}_2\text{S}_n$ ,  $4 < n \leq 8$ ) in the electrolyte. At last, the intermediate of  $\text{Li}_2\text{S}_8$  has been founded to be transformed into solid elemental sulfur. The whole discharge/charge process has been certificated by a series of experiments such as operando UV-Vis spectra, operando X-ray Absorption Spectra and operando X-ray diffraction analysis.

## 1.2 Motivation of developing rechargeable lithium-sulfur batteries

To develop the next-generation rechargeable battery technologies, lithium-sulfur batteries have been one of the most attractive candidates for its high theoretical capacity, high energy density, competitive cost and environment-friendly properties. In comparison with traditional rechargeable batteries, the limited capacity of Li-ion

batteries hindered the prompted battery energy demand. Besides, its restricted commercial cost, cycling life, gravimetric energy density and pollution because of its widely used transition metal oxide materials, such as expensive cobalt and nickel elements. By utilizing the long-life rechargeable lithium-sulfur battery technology, the battery systems can further considerably support the high demand of portable devices. In comparison, the usage time could be improved by three times at least longer than that of traditional lithium-ion batteries.

In addition, the rechargeable lithium-sulfur batteries can also be applicable in some large-scale stationary energy-storing devices, which can further link with green energy, such as wind, solar, geothermal, and hydropower for renewable electric grids. It may be one of the possible pathways to solve the power-transmission problems that significantly hindered the development of renewable energy sources.

Hence, coupled with the average operating voltage in lithium-sulfur cell (2.15 V vs  $\text{Li}^+/\text{Li}^0$ ) and the theoretical capacity ( $1,675 \text{ mA h g}^{-1}$ , calculated based on the mass of sulfur), the energy density can be estimated as high as  $\sim 2500 \text{ W h kg}^{-1}$ , which is approximately 5 times higher than that of traditional lithium-ion batteries. To develop the possible rechargeable lithium-sulfur batteries, how to commercialize the lithium-sulfur batteries has attracted a series of researchers in the world.

## 1.3 The challenges of lithium-sulfur batteries

### 1.3.1 Demerits of sulfur

When sulfur in cathode materials, a series of materials associated with the physical properties of the sulfur and the related intermediate lithium polysulfide, and the basic electrochemical reactions in lithium-sulfur batteries. Because of sulfur as an electrical insulator with the conductivity as low as  $1 \times 10^{-15} \text{ S/m}$ , much more conductive agent needed to be added. Conductive agents need to be appropriately added into the sulfur cathode, and well-dispersed active sulfur cathode material is desired to ensure the electrical conductivity. Volume expansion of sulfur also hinders the developments of lithium-sulfur batteries.

When the sulfur reacts with lithium ions to form the  $\text{Li}_2\text{S}$ , the predicted volume expansion of  $\text{Li}_2\text{S}$  is approximately 80% of the volume of the original sulfur. However, considering the natural sulfur as the most stable form of cyclo-S<sub>8</sub>, the sulfur cathode tends to witness much larger volume expansion than expected. This brings into a large amount of mechanical stress on the cathode structures, especially on the sulfur host, coupling with significantly structural collapse and mechanical deterioration, suggestive of continuous electrical disconnection with the interfaces of conductive agent and active sulfur materials. The worsening phenomena on the cathode tend to block the electronic path and further prevent the migration of lithium ions to the surface of sulfur particles.

### 1.3.2 Demerits of the intermediate lithium polysulfide

The improper property also involves a host of intermediate lithium polysulfide, composing of soluble long-chain lithium polysulfide ( $\text{Li}_2\text{S}_n$ ,  $4 < n \leq 8$ ) and insoluble short-chain lithium polysulfide ( $\text{Li}_2\text{S}_n$ ,  $1 < n \leq 4$ ) [11-13]. The intermediate products of soluble lithium polysulfide ( $\text{Li}_2\text{S}_n$ ,  $4 < n \leq 8$ ) formed during the initial electrochemical process, are able to be dissolved into the liquid electrolyte. These active dissolved polysulfide anions may witness the intimate interconnection with additive conductive agents, to some extent, rather than that of the insulating sulfur particles. Simultaneously, their dissolution behavior may also result in lower polysulfide re-utilization and significant capacity fading in lithium-sulfur batteries, since they may escape out of the sulfur cathode and migrate to the metallic lithium anode. Some other side reaction may also occur. The highly active dissolved lithium polysulfide enables great threats to the electrolyte and solvent molecules in electrochemical process.

The products of insoluble short-chain lithium polysulfide ( $\text{Li}_2\text{S}_n$ ,  $1 < n \leq 4$ ) also performs with low electrical conductivity and solubility in electrolyte, which also take the negative influence on the output specific capacities and lower sulfur utilization in lithium-sulfur batteries.

In addition, the dissolution of active sulfur materials also resulted from the self-discharge phenomenon in lithium-sulfur batteries. It is an obviously disadvantageous issue, especially in the long-term storage. When the self-discharge phenomena occurred, its initial open circuit voltage (OCV) of the lithium-sulfur batteries would gradually decrease within the time, because soluble lithium polysulfide tends to be spontaneously converted by active sulfur particles, gradually diffuse out of the cathode, dissolve into the electrolyte and migrate to the anode.

The demerits of the intermediate products of lithium polysulfide have further resulted from a wide range of problems, such as low sulfur content, low sulfur utilization, cathode volumetric expansion, self-discharge phenomenon, poor long-life cycling performance, low Coulombic efficiency, and low long-term cycling life. The remaining challenges significantly hamper its potential development of lithium-sulfur batteries in practical applications.

### 1.3.3 Shuttle effects

Shuttle effects, the another side effects, also resulted from the dissolution of active sulfur materials in lithium-sulfur batteries, which significantly hindered its potential development in practical applications <sup>[9, 14, 15]</sup>. These dissolved lithium polysulfide ( $\text{Li}_2\text{S}_n$ ,  $4 < n \leq 8$ ) in the electrolyte are able to move freely through the separator. During the discharge/charge process, these soluble polysulfide anions are able to migrate forward to the anode and backward to the cathode.

This migration behavior is the alleged “shuttle effect,” which can have resulted in series challenges of low coulombic efficiency and corrosion of metallic lithium anode. While the soluble polysulfide ions ( $\text{Li}_2\text{S}_n$ ,  $4 < n \leq 8$ ) migrate through the separator, they would react with metallic lithium anode to form short-chain insoluble polysulfide ions ( $\text{Li}_2\text{S}_n$ ,  $1 < n \leq 4$ ). Because the polysulfide ions can shuttle severely between the cathode and the anode, the overcharged issue and low coulombic efficiency also tend to occur especially at the upper plateau of the charge curves.

### 1.3.4 Electrolyte for lithium-sulfur batteries

Electrolyte systems in lithium-sulfur batteries also play an important role to influence the battery performance. S. H. Zhang has already carried out sufficient researches on explaining the possible mechanism of the liquid electrolyte employed in lithium-sulfur batteries [10, 15, 16]. In fact, on the basis of the researches, the traditional electrolytes do not fit the novel lithium-sulfur battery due to the existence of highly reactive and dissolved lithium polysulfide.

#### Proposed Reactions between Polysulfides and Carbonates

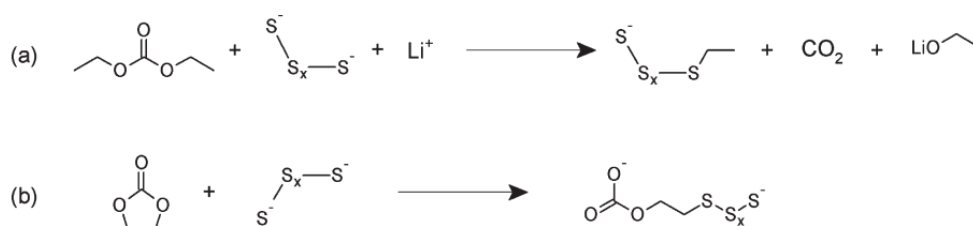


Fig. 1.4. The side reaction between the dissolved polysulfide intermediates and traditional carbonate electrolytes [15, 16].

The widely used organic electrolyte in lithium-sulfur battery adopts the mixed low viscosity ethers solvents as electrolyte, such as 1,3-dioxolane (DOL) and 1,2-dimethoxy ethane (DME).

The choice for the mixed solvents as electrolyte is that DME possesses higher solubility towards dissolved lithium polysulfide than DOL. However, DME is not stable enough and tends to react with lithium metal anode, resulting in poor cycling performance in lithium-sulfur batteries. Simultaneously, DOL can be added to stabilize the mixed electrolyte for its lower evaporation. A trace amount of lithium nitrate (0.1M LiNO<sub>3</sub>) as additive in electrolyte helps the anode surface form a solid electrolyte interface (SEI) [10, 16]. Therefore, the synergistic effects of the mixed solvents as electrolytes take beneficial advantages on the dissolved lithium polysulfide and sulfur utilization in lithium-sulfur batteries.

In contrast, traditional carbonate electrolytes (e.g., ethylene carbonate and diethyl carbonate) were regarded as improper choice for in lithium-sulfur batteries because of

their low polysulfide solubility and high reactivity with dissolved intermediate <sup>[17, 18]</sup>. During the discharge process, the dissolved long-chain lithium polysulfide would react with carbonate based electrolyte irreversibly until the total amount of electrolytes has been consumed up. The consumption represents the poor cycling performance, even witnesses abnormal electrochemical reaction during the discharge-charge process of lithium -sulfur batteries. The possible redox reaction mechanism that employs carbonate-based electrolytes in the lithium -sulfur batteries, has been proposed.

## 1.4 Cathode design for lithium-sulfur batteries

To employ the proper sulfur host has attracted a wide range of researchers' interests <sup>[19]</sup>. In fact, porous carbon materials have been regarded as the suitable candidate for the composite because of their high adsorption and specific surface area <sup>[20-23]</sup>. By the melting methods, the sulfur can be melted and immersed into the pores of carbon materials which can be ascribed as one effective and advantageous pathway. In addition, it can also bring with high sulfur content as sulfur cathode. Hence, a series of functional porous carbon materials, such as mesoporous carbon, microporous carbon, hollow carbon spheres and hierarchical porous carbon, have been adopted and employed as the host to accommodate the sulfur.

Porosity has been reasonably chosen as host to contain sulfur and attempted to prevent soluble lithium polysulfide diffused into the electrolyte <sup>[6, 24]</sup>. In general, the porous carbon materials can be categorized as three main species. Its main classification is ideal but simplified according to the diameters of pore size: 1<sup>st</sup> microporous materials (< 2 nm); 2<sup>nd</sup> mesoporous materials (2 nm ~ 50 nm), and 3<sup>rd</sup> macroporous materials (> 50 nm). Indeed, a huge number of porous materials contain no less than one kind of pores, simultaneously <sup>[25]</sup>.

On the basis of serial calculation, the length of soluble long-chain lithium polysulfide ( $\text{Li}_2\text{S}_n$ ,  $4 < n \leq 8$ ) lie in the range of microporous diameters which play the

role in containing soluble long-chain lithium polysulfide. Microporous carbon materials can act as an ideal host in lithium-sulfur batteries, and then the mesoporous materials. Mesopores can illustrate excellent lithium-ion transport properties because of the abundant pathways between the electrolyte and the sulfur particles. In contrast, due to the large pores, macroporous carbon materials can provide enough interaction between the active sulfur material and electrolyte in lithium-sulfur batteries. However, the macropores are too large to effectively restrict either the sulfur materials or electrolyte and securely suppress soluble lithium polysulfide ( $\text{Li}_2\text{S}_n$ ,  $4 < n \leq 8$ ) diffusion into the electrolyte.

What remained to be demonstrated is whether the host can provide enough spaces for the sulfur particles and the intimate contact between sulfur particles and mesoporous carbon host. Towards the sulfur host, more important is effectively containing the sulfur particles. This is because it plays the key roles in providing sufficient volumetric expansion and ion transport at the cathode. Therefore, a series of materials with high surface area or adsorption properties can also be used as sulfur host.

#### 1.4.1 Porous carbon as sulfur host

Ordered mesoporous carbon (CMK-3) was firstly reported by Ryoo et al. in 1999, produced by SBA-15 silica as the template and sucrose as the carbon source under hydrothermal conditions <sup>[26, 27]</sup>. After that, the most well-known member of the ordered mesoporous carbon family has drawn overwhelming attention for potential applications, such as hydrogen adsorption <sup>[28]</sup>, catalyst carrier <sup>[29]</sup>, lithium storage <sup>[30]</sup> and supercapacitor <sup>[31]</sup>.

Since the *L. F. Nazar* et al. first reported with CMK-3 as cathode sulfur host in 2009 <sup>[19]</sup>, the development of the novel cathode structural design has attracted a huge number of attentions. The potential rechargeable lithium-sulfur batteries can be realized because of the huge desire for high energy density storage systems. By melting and immersing the sulfur into the sulfur host to construct the cathode

structures, a series of materials have been attempted to improve the electrochemical performance in lithium-sulfur batteries.

The host of highly ordered CMK-3 illustrates uniform pore sizes, high pore volume, and high conductivity. The synthesizing methods for sulfur-containing CMK-3@S composites can be classified as sulfur/carbon mixture, sulfur-melting route, and sulfur immersion.

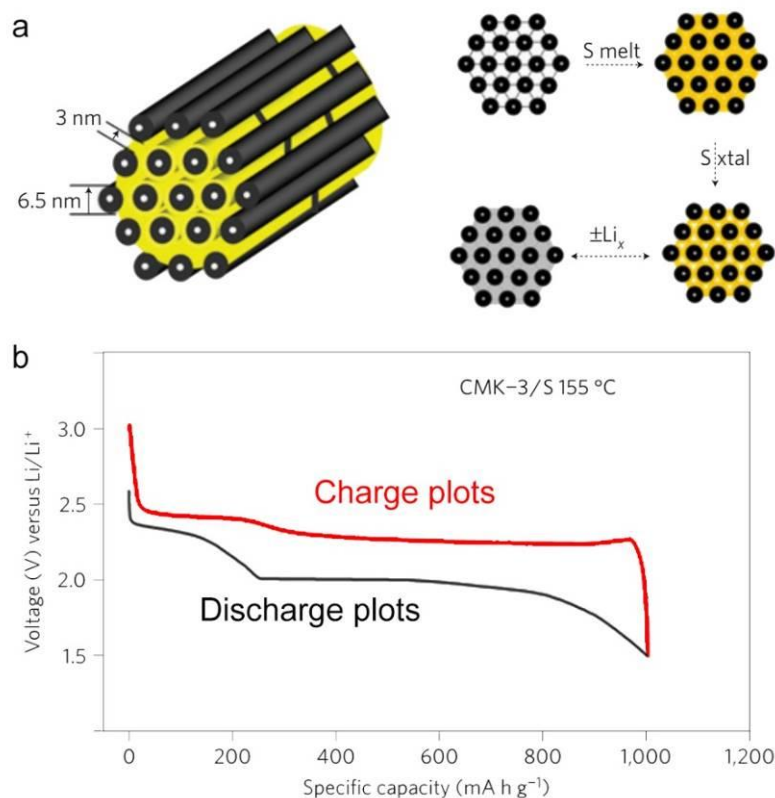


Fig. 1.5. The CMK-3 as the sulfur carrier (a) and the discharge/charge curves of recharge lithium-sulfur batteries (b) <sup>[19]</sup>.

#### 1.4.2 Carbon nanotube (CNTs) as sulfur host

Carbon nanotubes (CNTs) are a large family of carbon molecules with valuable nanotechnology, electronics, optics properties. Nanotubes are members of the structurally cylindrical carbon family. They are famous for their long, hollow structure with the multi-walled (MWNTs) or single-walled tubes (SWNTs). Individual nanotubes are naturally self-assembled by van der Waals forces, more specifically, pi-stacking effects.

Because of their outstanding structural intensity and firmness, CNTs are able to find a lot of applications as additives to various structural materials. In addition, the CNTs also illustrate excellent thermal stability and conductivity, it has been widely researched in the fields of materials science and energy-storing technology.



Fig. 1.6. The microporous carbon coating on CNT as the sulfur carrier for rechargeable lithium-sulfur batteries <sup>[32]</sup>.

Since in 2010, the *Y.G. Guo* et al. reported the single-walled CNTs as the sulfur host, the CNTs@S materials illustrate attractive stability <sup>[32]</sup>. Its long-term cycling performance can arrive at the current density of 0.1 C over 200 cycles. Just the sulfur content of the cathode materials is relatively lower (<50 wt%), which strictly limited the advantageous high energy density of lithium-sulfur batteries.

CNTs can act as the sulfur host with highly reversible capability in rechargeable lithium-sulfur batteries, because there is much more efficiency of storing and utilizing the sulfur and dissolved intermediate lithium polysulfide if compared with traditional sulfur cathode. When CNTs are used to build up the sulfur cathode, the network structures are able to partly suppress the polysulfide migration for the high absorbability.

A series of researches have showed that the CNTs are able to enhance its electrochemical performance with lower sulfur content or in the phase transition stage while the active elemental sulfur has been converted into soluble long-chain lithium polysulfide ( $\text{Li}_2\text{S}_n$ ,  $4 < n \leq 8$ ). Pore structures can also be introduced in CNTs and CNFs via various delicate synthesis methods to obtain improved cycle performance. Because it can function, to some extent, towards these dissolved polysulfide ions

inside the carbon nanotubes in the initial phase and partly suppress them migrating to the anode. Therefore, the CNTs enable to play the contributing factors to impact the cathode performance in the lithium-sulfur battery.

### 1.4.3 Graphene as sulfur host

Graphene is a kind of two-dimensional and atomic-scale layered carbon molecules. It is firstly prepared from the graphite. Its proposed layered structure can be regarded as an indefinitely large aromatic molecule made of flat polycyclic aromatic rings.

Graphene illustrates robustness, light-weight and high conductivity, which has attracted a wide range of interests in recent years. The characteristics with flexibility and high adsorbing capability render it suitable to act as the sulfur host in the lithium-sulfur battery. Its excellent conductivity of graphene can improve the sulfur utilization at the cathode. The graphene coating or wrapping on the cathode can also promote its intimate interaction between the sulfur particles and electrolyte and partly suppress the loss of dissolved lithium polysulfide ( $\text{Li}_2\text{S}_n$ ,  $4 < n \leq 8$ ) during electrochemical cycling.

In addition, graphene oxide (GO), formerly called graphitic oxide, is the family of functional graphene with hydrophilic groups as carboxylic and hydroxyl groups. It can be easily dissolved into water in the black/brown color and retain the layered structure of graphene as graphene oxide sheets. GO has attracted substantial interest as a proper choice for its special chemical and structural properties which also takes an advantage in rechargeable lithium-sulfur batteries.

Since in 2011, the *Y. Cui and H. Dai* et al. reported the graphene-wrapped sulfur particles as the sulfur host, the graphene-sulfur composite materials illustrate attractive stability<sup>[33]</sup>. Its sulfur content of the cathode materials raised up to ~70 wt%. The specific capacities can reach up to ~600 mAh/g over more than 100 cycles at the current density of C/5, representing promising high energy density as cathode material for rechargeable lithium batteries.

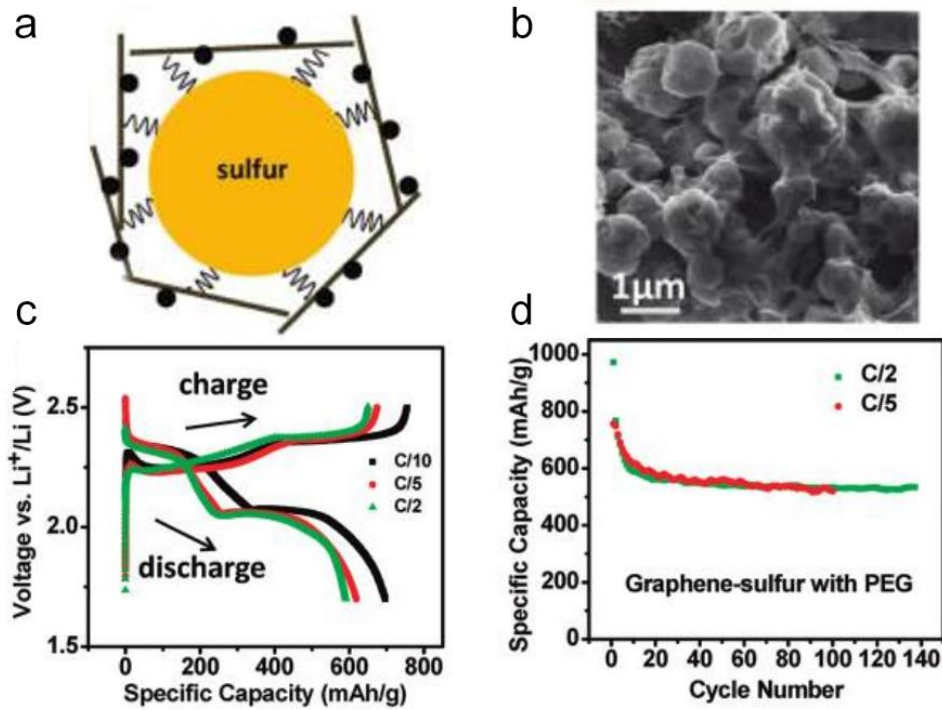


Fig. 1.7. The Graphene coating on the sulfur particles for rechargeable lithium-sulfur batteries [33].

Since in 2014, the *G.J. Hu* et al. reported a 3D graphene-foam nested hierarchical network is synthesized with high sulfur loading for lithium-sulfur batteries [34]. The 3D graphene-foam was grown by chemical vapor deposition (CVD). Its sulfur content of the cathode materials raised up to over 80 wt%. The specific capacities can reach up to ~645 mAh/g over more than 350 cycles at the current density of C/5 with a capacity decay of 0.1% per cycle.

However, the limited discharge/charge process suggests the disadvantageous cycling life for lithium-sulfur batteries. Due to sulfur volumetric expansion, the surface-wrapping graphene laminates gradually malfunction to ensure the intimate interaction between the sulfur particles and electrolyte within the prolonged long-life cycling.

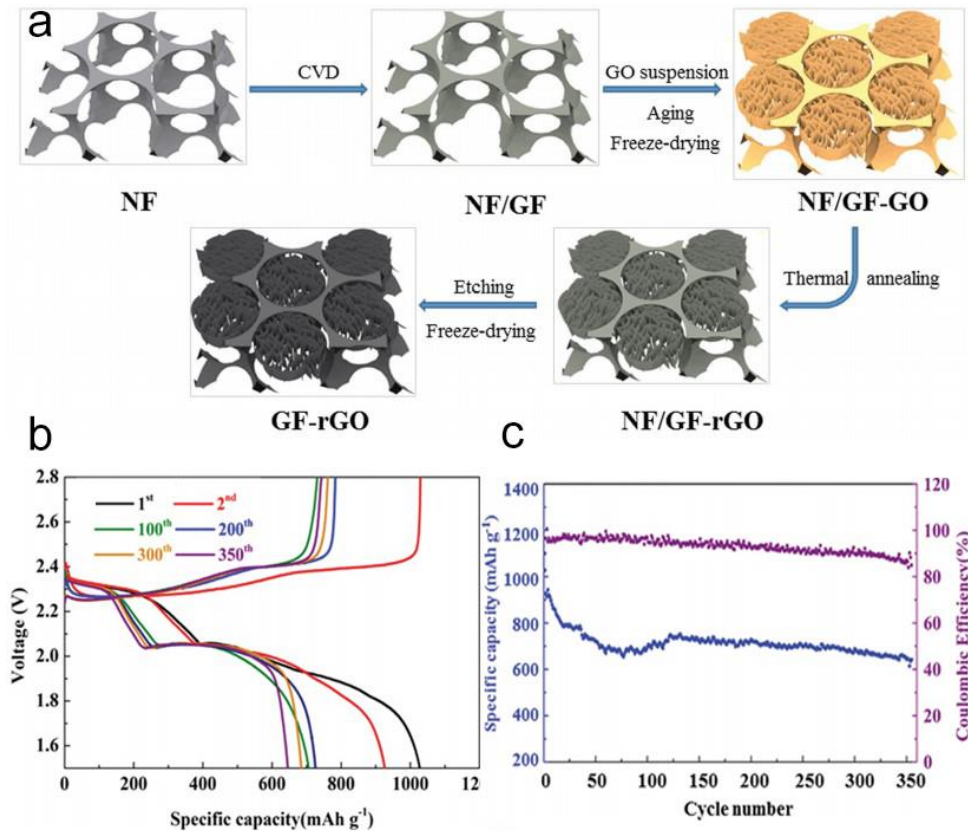


Fig. 1.8. The 3D-Graphene frameworks as the sulfur carrier for rechargeable lithium-sulfur batteries [34].

#### 1.4.4 Polymer coating as sulfur host

Polymer represents a large family of macromolecular materials, composed of many small molecules. Its structure is fabricated *via* polymerization of many elemental subunits, known as monomers. The molecular weight ranges wildly, from large molecular mass to small molecule compounds, which produces unique physical and chemical properties, including toughness, functional groups, and a transition glasses state rather than crystals.

Because of their tunable ranges and structures, polymers play an essential and are fundamental role in rechargeable batteries. Such as commonly used polyvinylidene fluoride (PVDF) can act as the binder to integrate carbon additives and sulfur particles onto a current collector and strength the cathode structures.

Initially, polymer was chosen as the reagent to form sulfur-containing organic

materials and stabilize the sulfur. Some polymer species, such as electro-polymerized polyacetylene, polythiophene, polypyrrole and polyaniline have been chosen to form the conductive organic sulfide at higher temperature ( $\sim 300\text{ }^{\circ}\text{C}$ ) [35-38]. A sulfur-containing polymer was constructed as an electronically conductive polymer matrix in which sulfur atoms can be embedded. A series of attempts have been attempted to improve its electronic conductivity and prevent the dissolved lithium polysulfide ( $\text{Li}_2\text{S}_n$ ,  $4 < n \leq 8$ ).

However, the significantly reducing voltage plateaus tend to lower the high energy density, which does not embody the advantageous high capacity density in lithium-sulfur batteries [35-39]. More notably, their specific capacity densities are generally limited less than 1,000 mAh/g. In addition, no matter whether the traditional organic sulfides or elemental sulfur act as the sulfur cathode, it both suffers from the intermediate dissolved into the electrolyte, further self-discharge and poor electronic conductivity of lithium-sulfur batteries.

#### 1.4.5 Oxide materials as additive

Except these polymer coating methods, a series species of oxide materials have been also used as additives in lithium-sulfur batteries, such as titanium oxide compounds, silicon dioxide, alumina and manganese oxide. Coating a stable thin layer of oxide materials on the nano-sized sulfur particles is another approach to improve the long-life cycling.

These oxide materials employed in lithium-sulfur batteries can be separated into two types: surface coating and non-surface coating materials. In 2013, Y. Cui et.al. reported that an elaborate yolk-shell  $\text{TiO}_2$ -sulfur structure exhibits a long-life cycling [40]. The  $\text{TiO}_2$  coating on the nano-sized sulfur particles and dissolve partial sulfur helps form the yolk-shell  $\text{TiO}_2$ -sulfur structure. These attempts are to reserve proper void or pore space and avoid the collapse of the  $\text{TiO}_2$  spheres. This well-designed structures for sulfur host is desirable not only to cushion the volume expansion of sulfur, but also retain these subsequent dissolved lithium polysulfide ( $\text{Li}_2\text{S}_n$ ,  $4 < n \leq 8$ )

during discharge/charge.

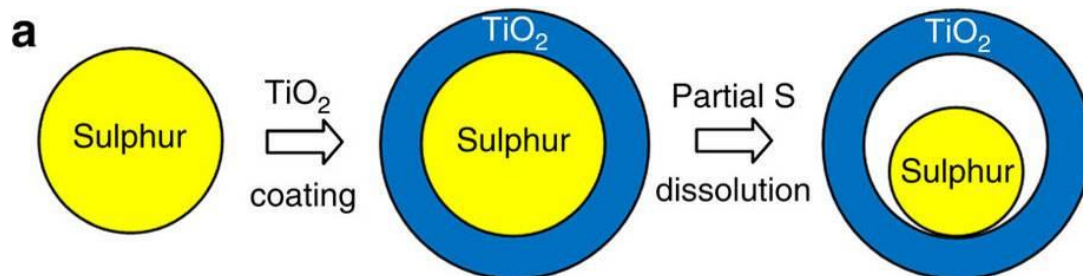


Fig. 1.9. The  $\text{TiO}_2$  coating on the surface of nanosized sulfur particles for rechargeable lithium-sulfur batteries <sup>[40]</sup>.

Its capacity decay over 1000 cycles is as low as 0.033% per cycle at the current of  $C/2$ . That suggests the yolk-shell  $\text{TiO}_2$ -sulfur structure can improve cycle stability and reduce polysulfide shuttle, although its complicated and difficult modification methods need to be further enhanced for possible practical application.

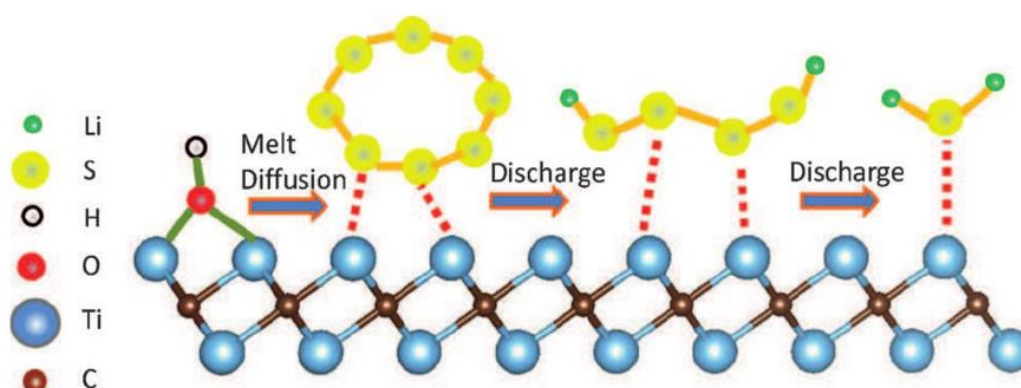


Fig. 1.10. The MXene nanosheets as the sulfur carrier for rechargeable lithium-sulfur batteries <sup>[41]</sup>.

In addition, a series of transition metal oxide materials have also used as additives in lithium-sulfur batteries. Since in 2015, *L.F. Nazar et.al.* reported that a conductive 2D early-transition-metal carbide (titanium carbide) MXene sheet, can perform as an excellent sulfur battery host for their high conductivity of metal-oxide materials and self-functionalized surfaces <sup>[41]</sup>. The MXene nanosheets help stabilize sulfur particles and adsorb these dissolved lithium polysulfide intermediates, because the strong interaction between the polysulfide species and the surface Ti atoms.

The 70 wt% sulfur-containing cathode composites exhibit long-term cycling performance with specific capacity close to 1200 mA h/g at the current rate of C/5. Its remained capacity retention is ~ 80 % over 400 cycles.

## 1.5 Functional separator for lithium-sulfur batteries

### 1.5.1 Porous carbon paper as separator

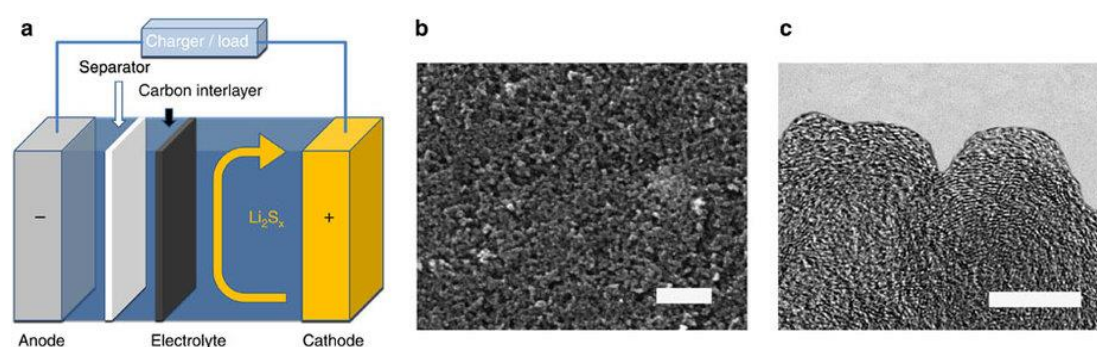


Fig. 1.11. The microporous carbon paper as the separator for rechargeable lithium-sulfur batteries <sup>[42]</sup>.

Since in 2013, A. Manthiram *et. al.* reported a functional carbon interlayer can act as a separator to partially block the dissolved lithium polysulfide and permit lithium ion migration <sup>[42]</sup>. The porous carbon paper serves, to some extent, towards the polysulfide intermediates, resulting in less shuttle effect and better capacity retention. Their design proposed the integrated functional separators for lithium-sulfur batteries to allow lithium ion move freely but hinder polysulfide migration.

### 1.5.2 Graphene oxide paper as separator

Graphene oxide can be easily dissolved into water due to its functional hydrophilic carboxylic and hydroxyl groups. Simultaneously, it retains the layered graphene oxide nano- sheets. GO has attracted substantial interest as a proper choice because its easy fabrication and mechanical robustness takes an advantage for a membrane/separator

in lithium-sulfur batteries.

Since in 2015, the Q. Zhang and F. Wei et al. reported the thin graphene oxide membrane for lithium-sulfur batteries [43-45]. The oxygen electronegative atoms modified GO membrane can remain high stability under electrochemical conditions. Simultaneously, it can help the migration of positively charged species ( $\text{Li}^+$ ) and rejection of the transportation of negatively charged dissolved lithium polysulfide ( $\text{Li}_2\text{S}_n$ ,  $4 < n \leq 8$ ).

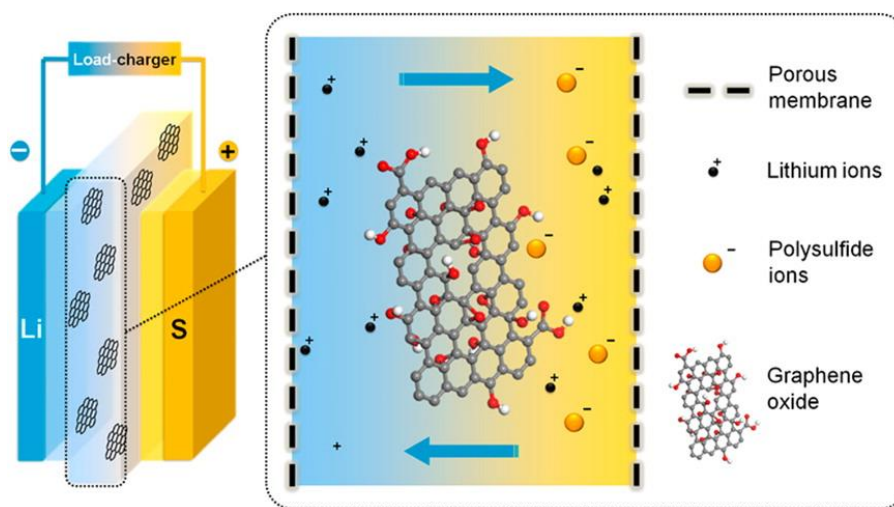


Fig. 1.12. The graphene oxide membrane as the separator for rechargeable lithium-sulfur batteries [43-45].

When the CNTs contains sulfur up to  $\sim 64$  wt% as cathode materials, the lithium-sulfur batteries with GO separator illustrate attractive stability. The specific capacities can reach up to  $\sim 700$  mAh/g over more than 100 cycles at the current density of C/10, representing promising effects towards dissolved polysulfide intermediates for rechargeable lithium batteries.

However, the diffusion of soluble polysulfides causes the function of the GO separator to worsen because of the existence of numerous void cracks among the GO layers [44-46]. According to previous calculations, all the S-S chain lengths estimated among the species of lithium polysulfide ( $\text{Li}_2\text{S}_n$ ,  $4 < n \leq 8$ ) ranged from 2.09 Å to 2.39 Å, and the lithium-sulfur bond lengths tended to be slightly less than 2.6 Å [47]. Moreover, these GO interlayers are unable to function towards polysulfide molecules

because the polysulfide diameters are less than their spacing distances ( $d \leq 13 \pm 1 \text{ \AA}$ )<sup>[44]</sup>.<sup>46]</sup>. The polysulfides can readily permeate through GO layers along these voids.

### 1.5.3 Conductive carbon coating on the Celgard separator

Since in 2014, the Y. Cui et al. reported the thin conductive carbon (Super P) coating on the separator to prevent the migration of dissolved lithium polysulfide ( $\text{Li}_2\text{S}_n$ ,  $4 < n \leq 8$ ) in lithium-sulfur batteries<sup>[48]</sup>. Because of this separator, the lithium-sulfur battery illustrates the improved specific capacity and cycling stability compared to that with a pristine Celgard separator. The prolonged cycling life can reach over 500 cycles at the current of  $C/2$  and a cycle decay as low as 0.09% per cycle.

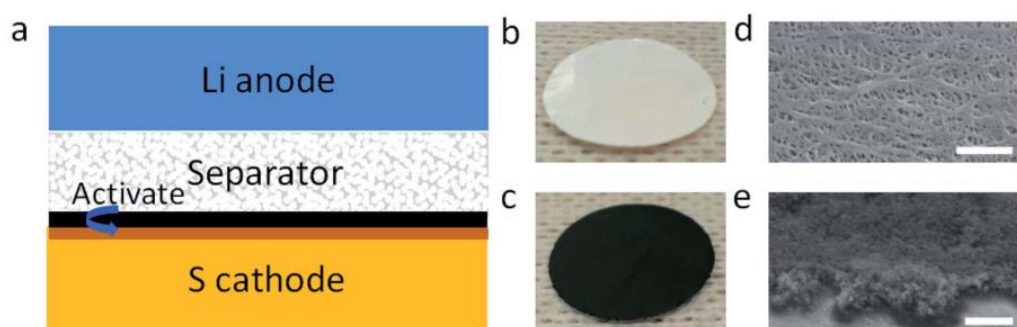


Fig. 1.13. The Super-P conductive carbon coating on the Celgard separator for rechargeable lithium-sulfur batteries<sup>[48]</sup>.

However, the permeation experiments certificated that the separator can't block the dissolved  $\text{Li}_2\text{S}_8$  solutions for a long time. After 30 minutes of diffusion, the  $\text{Li}_2\text{S}_8$  filled the separator. When the diffusion time prolonged to 70 minutes, the  $\text{Li}_2\text{S}_8$  fully filled the pores in the separator. In fact, due to the existing numerous void cracks among the conductive carbon particles, this modified separator is difficult to continuously help the migration of positively charged species ( $\text{Li}^+$ ) and rejection of the transportation of negatively charged dissolved lithium polysulfide ( $\text{Li}_2\text{S}_n$ ,  $4 < n \leq 8$ ).

### 1.5.4 Coating graphene on polypropylene-supported separator

The graphene sheets help adsorb and stabilize these dissolved lithium polysulfide

intermediates, because the strong interaction between the polysulfide species and the graphene surface.

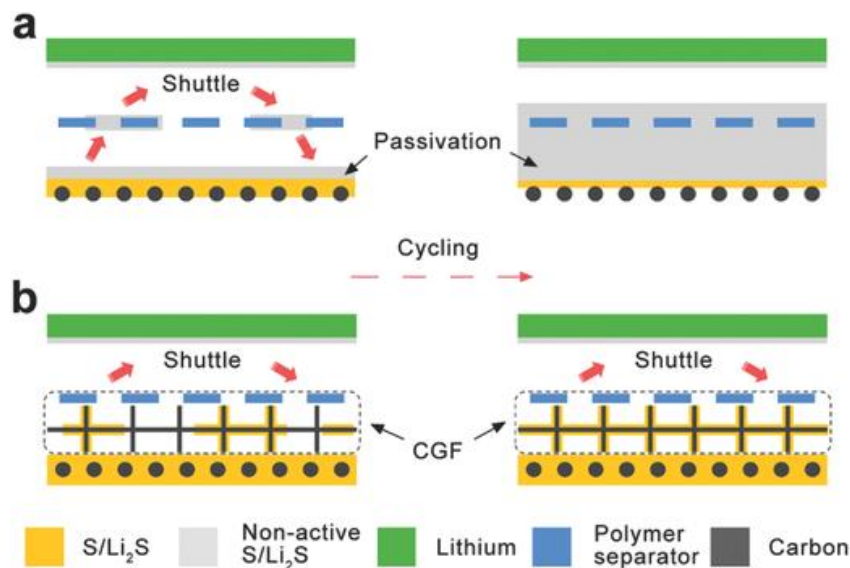


Fig. 1.14. The Graphene coating on the polypropylene separator for rechargeable lithium-sulfur batteries [49].

Since in 2015, the Q. Zhang et al. reported the coating the mesoporous graphene frameworks on polypropylene separator to promote the sulfur utilization [49]. The lithium-sulfur batteries with this graphene/ polypropylene separator illustrates a high initial capacity of 1109 mAh g<sup>-1</sup> and superior capacity preserved over 800 mAh g<sup>-1</sup> after 250 cycles at the current of C/5. The separator can partially suppress the negative impacts of shuttle mechanism and improve the utilization of sulfur and overall energy density in lithium-sulfur batteries.

This idea of the layered by layered hydrophobic/hydrophilic structures introduces integrated electron/ion conductivities. The well-designed functional separators are able to effectively suppress the shuttled dissolved polysulfide intermediates. It may guide the further design principles for improving energy density and prolonged cycling life of lithium-sulfur batteries.

## 1.6 Metal-organic frameworks based separator

Even then a series of functional separators have been designed for liquid

electrolytes in the lithium-sulfur batteries, these separators cannot effectively block the migration of dissolved polysulfide anions which result in the “shuttle effect”. Bai and Zhou conceived an idea of developing a Metal-Organic Frameworks (MOF) based separator lying between the sulfur cathode and anode in lithium-sulfur batteries.

### 1.6.1 The chemical affiliation of Metal-organic frameworks

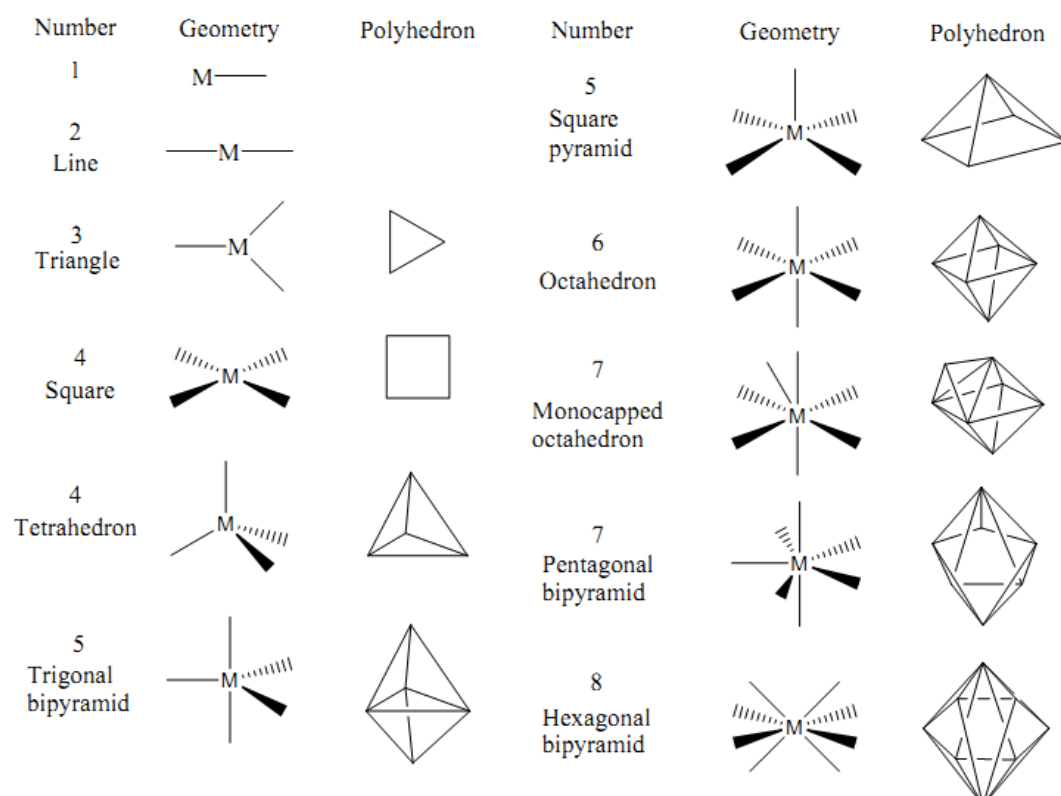


Fig. 1.15. The different coordination mode between the organic ligand and metal centers in metal-organic frameworks [50, 51].

Coordination Chemistry is an important branch of supramolecular chemistry [50, 51]. In general, coordinated compounds consists of serial central atoms or ions and a surrounding array of bound molecules or ions. The coordination center is made up to usually metallic atoms, especially those of transition metallic atoms. Coordination compounds are theoretically constructed by the coordinate covalent bonds (dipolar bonds) between the organic ligands and the central atoms.

Metal ions in the metal-organic frameworks can be seen as connectors, and ligands can be regarded as linkers [52]. Because metal ions have different properties, such as

different radii and sizes, surface charge distribution and electronic configuration among serial metal species, the crystalline structures illustrate unique coordination modes with different coordination metal ions and organic ligand to construct a coordinated metal-organic framework <sup>[53]</sup>. The coordination mode between the transition metal ions and the corresponding coordination ligands ranges lies in a wide range, such as two coordination (linear), three coordination (triangle), four coordination (tetrahedral, square), five coordination (tetragonal pyramid, square planar), six-coordinate (octahedral, triangular prism, anti-triangular prism).

In the self-assembly process, metal-organic complexes with different topological structures, such as interpenetrated metal organic compounds, can be obtained by choosing different metal ions and suitable organic ligands.

### 1.6.2 The porosity of Metal-organic frameworks

Metal-organic frameworks (MOFs) are a large family of coordinated compounds consisting of metal ions or clusters with organic ligands to form versatile structures. The metal-organic framework is also categorized as the SBUs (secondary building units) and the organic linking ligands. They are a subclass of crystalline coordinated materials, with the attractive feature that they are often porous <sup>[53-55]</sup>.

Different structures in metal-organic framework can be divided into the node or connector, linker, expansion, decoration, augmentation, interpenetration, and so on. These subclass units make the spatial structure of MOF more complicated. Secondary building units (SBUs) also expand the nodes in the metal-organic structures, ranging from single-core, dual-core, triple-core, quad-core, eight-core and even larger multi-core molecular clusters.

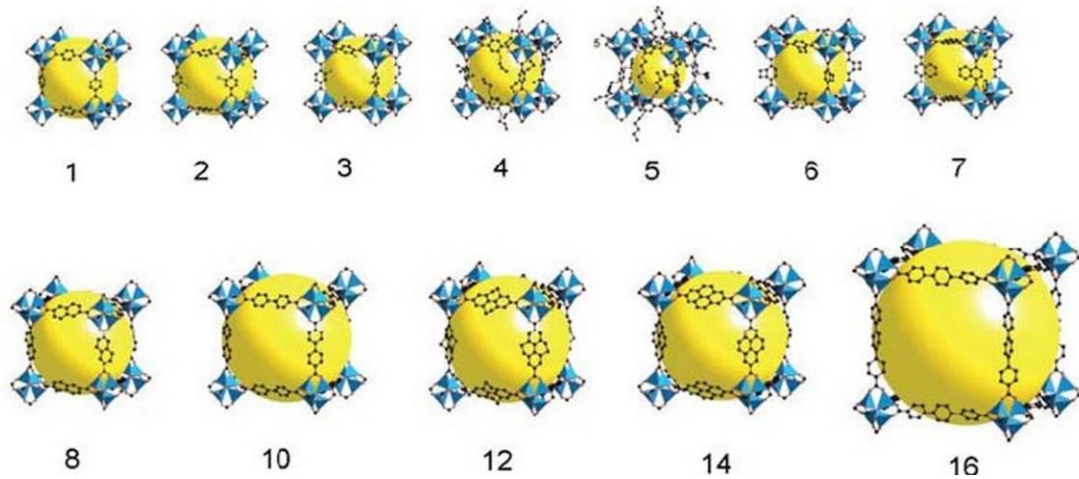


Fig. 1.16. The tunable porous structures with different organic ligand in metal-organic frameworks <sup>[53-55]</sup>.

The study of MOFs developed from the study on the class of zeolites, except for the use of proper organic ligands. In contrast with zeolites, MOFs are constructed with organic ligands that remain intact throughout the synthesis and influence the structure of the growing framework. MOFs are produced frequently under hydrothermal or solvo-thermal conditions, where crystals are slowly grown in solutions.

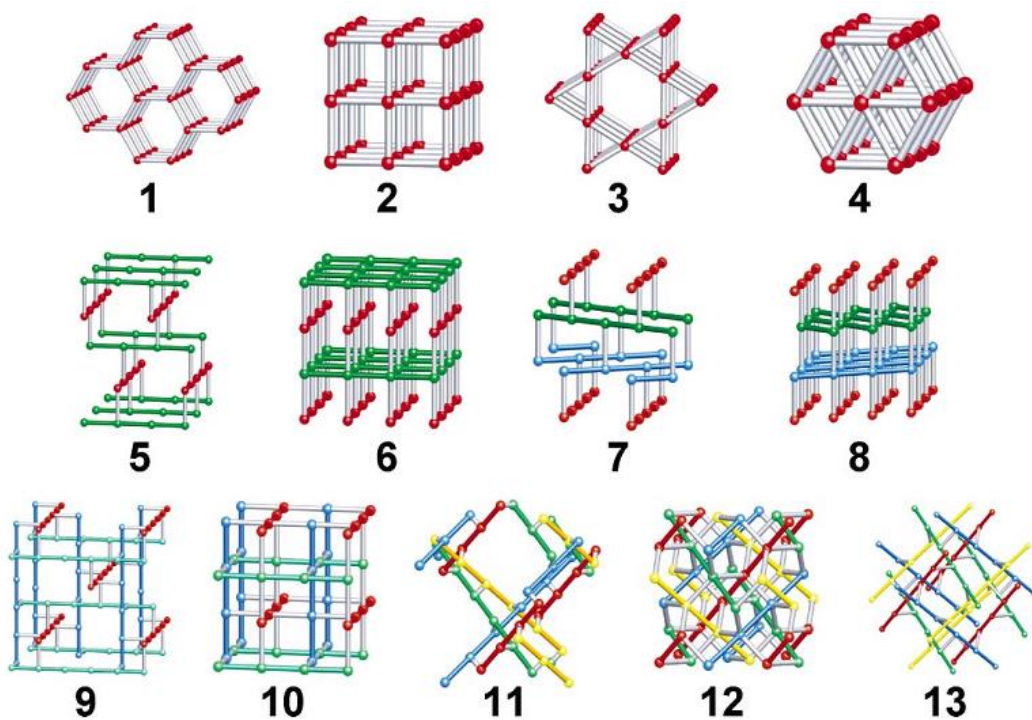


Fig. 1.17. The simplified different coordination mode (Topo structures) in

metal-organic frameworks [53-55].

Hence, the dehydration process is always necessary. When the solvent is evacuated, that is also useful for MOFs intended for its exposed active sites around these metal centers, providing abundant binding at these sites and allowing high specific surface area and gas adsorption/desorption.

More subtly, due to its highly tunable structures, a coordinated compound in a metal-organic framework tends to contain potential voids [56]. The organic ligand is able to link the metal center to form one-dimensional chain and extend the coordination network through repeating coordination entities to form two-dimensional array. Moreover, the complex cross-links can be finally extended in one, two or three dimensions through repeating coordination entities.

The pores in metal-organic frameworks have been widely researched in the gas storage, such as the adsorption of hydrogen and carbon dioxide, in gas purification, in gas separation, in chemical catalysis, as sensors and as supercapacitors.

The stick topology network has been used to simply and analyze the metal-organic structures because of their complicated coordination mode and indefinitely repeating coordination entities along different orientations.

### 1.6.3 The ionic sieving effects of MOF based materials

Porous MOFs have emerged as a new family of hybrid porous materials. In contrast to monotonous tetrahedral building blocks in zeolites, MOF can be constructed by various inorganic clusters and organic linkers. Consequently, MOF as versatile ionic sieving materials possess a wide range of surface areas (up to 6500 m<sup>2</sup>/g), functional groups from organic ligands, and pore sizes (micropores, mesopores and macropores) [57, 58].

In the past decade, a huge number of experiments and simulations have been reported for ionic sieving in MOFs. Because of highly functional pore sizes and active sites around the central metal cluster, MOF has been also explored for the removal of

anions or cations under liquid conditions for purification. For example, Custelcean et al. have reported the selective ionic sieving capability of  $\text{SO}_4^{2-}$  anions from a highly competitive aqueous environment into a Ni-coordination framework functionalized by urea. Fang et al. observed amine-templated MOF illustrates the cationic sieving capability of  $\text{K}^+$  ions [59]. It is investigated the removal capability of sieving metal ions through anion-exchange by functional groups in porous open frameworks.

One Cu(I)-based MOF reported by Bai et al. was designed to possess weak electrostatic interactions between cationic frameworks and encapsulated nitrate anions and thus displaying versatile colorimetric sieving and selective separation capacity towards a variety of inorganic anionic species [60]. Due to the versatile metal cluster and organic ligand, the flexibility derived from tunable ligand instead of the monotonous structural rigidity, could properly position the frameworks with functional ionic sieving capacity. This will satisfy the multi-purpose demand for an ion sieve, allowing for greater tunable ionic sieving capability.



Fig. 1.18. The anion sensing MOF with visual colorimetric responses to a series of anions [60].

#### 1.6.4 The MOF based separator for lithium-sulfur batteries

The MOF based separator is expected to expand its capability from molecular to ionic sieve. Due to the high-ordered porous frameworks, its larger surface area and ionic selectivity based on size and shape is the most appropriate building blocks for separators in lithium-sulfur batteries. Owing to the open metal sites with ligand's functional groups, the infiltrating metal-organic compounds can act as a high-efficient selective carrier, displaying outstanding molecular/ionic transferring capability.

However, the crystalline morphological drawbacks have hampered its success in potentially separating polysulfide. The introduced graphene oxide (GO) laminate have also been treated as improper separators, because of its evanescent robustness in solutions over time and relatively larger distances between GO layers than the diameters of polysulfide. Thereby, our design cooperatively takes advantages of the porous crystalline coordination as the building blocks, and the flexible GO laminates as the structural spokes. Make sure the self-assembled separator is dense and well-grown along the grain boundary at room temperature. The synergetic strategy has sufficiently regulated the cooperative nature of the stable porous structures and the flexible fabrications. This will satisfy the multi-purpose demand for a functional polysulfide separator, allowing for greater interconnections of enhanced fabrications and polysulfide resistance.

The MOF based separator functions as an ionic sieve to block the shuttling dissolved polysulfide and result in less shuttle effect and better capacity retention, leading to superior long-life performance in lithium-sulfur batteries. In the future, it can further improve the practical potential of metal-organic materials in lithium-sulfur batteries.

## 1.7 Reference

- [1] V. Zimmer et.al., *Nucl Instrum Meth A*, 2014, **764**, 330-339.
- [2] M. Armand and J. M. Tarascon, *Nature*, 2008, **451**, 652-657.
- [3] P. G. Bruce, S. A. Freunberger, L. J. Hardwick and J. M. Tarascon, *Nat Mater*, 2012, **11**, 19-29.
- [4] B. Dunn, H. Kamath and J. M. Tarascon, *Science*, 2011, **334**, 928-935.
- [5] J. M. Tarascon and M. Armand, *Nature*, 2001, **414**, 359-367.
- [6] Y. X. Yin, S. Xin, Y. G. Guo and L. J. Wan, *Angew Chem Int Edit*, 2013, **52**, 13186-13200.
- [7] A. Manthiram, Y. Z. Fu, S. H. Chung, C. X. Zu and Y. S. Su, *Chem Rev*, 2014, **114**, 11751-11787.
- [8] A. Manthiram, Y. Z. Fu and Y. S. Su, *Accounts Chem Res*, 2013, **46**, 1125-1134.
- [9] S. S. Zhang, *J Power Sources*, 2013, **231**, 153-162.
- [10] S. S. Zhang and J. A. Read, *J Power Sources*, 2012, **200**, 77-82.
- [11] S. Walus, C. Barchasz, J. F. Colin, J. F. Martin, E. Elkaim, J. C. Lepretre and F. Alloin, *Chem Commun*, 2013, **49**, 7899-7901.
- [12] M. Cuisinier, P. E. Cabelguen, S. Evers, G. He, M. Kolbeck, A. Garsuch, T. Bolin, M. Balasubramanian and L. F. Nazar, *J Phys Chem Lett*, 2013, **4**, 3227-3232.
- [13] S. Y. Lang, Y. Shi, Y. G. Guo, D. Wang, R. Wen and L. J. Wan, *Angewandte Chemie*, 2016, DOI: 10.1002/anie.201608730.
- [14] L. M. Suo, Y. S. Hu, H. Li, M. Armand and L. Q. Chen, *Nat Commun*, 2013,

4,1481

- [15] S. S. Zhang, *J Electrochem Soc*, 2012, **159**, 920-923.
- [16] S. S. Zhang, *Electrochim Acta*, 2012, **70**, 344-348.
- [17] H. S. Ryu, H. J. Ahn, K. W. Kim, J. H. Ahn, K. K. Cho, T. H. Nam, J. U. Kim and G. B. Cho, *J Power Sources*, 2006, **163**, 201-206.
- [18] L. X. Yuan, J. K. Feng, X. P. Ai, Y. L. Cao, S. L. Chen and H. X. Yang, *Electrochem Commun*, 2006, **8**, 610-614.
- [19] X. L. Ji, K. T. Lee and L. F. Nazar, *Nat Mater*, 2009, **8**, 500-506.
- [20] S. R. Chen, Y. P. Zhai, G. L. Xu, Y. X. Jiang, D. Y. Zhao, J. T. Li, L. Huang and S. G. Sun, *Electrochim Acta*, 2011, **56**, 9549-9555.
- [21] C. F. Zhang, H. B. Wu, C. Z. Yuan, Z. P. Guo and X. W. Lou, *Angew Chem Int Edit*, 2012, **51**, 9592-9595.
- [22] N. Jayaprakash, J. Shen, S. S. Moganty, A. Corona and L. A. Archer, *Angew Chem Int Edit*, 2011, **50**, 5904-5908.
- [23] R. Elazari, G. Salitra, A. Garsuch, A. Panchenko and D. Aurbach, *Adv Mater*, 2011, **23**, 5641-5644.
- [24] C. J. Hart, M. Cuisinier, X. Liang, D. Kundu, A. Garsuch and L. F. Nazar, *Chem Commun*, 2015, **51**, 2308-2311.
- [25] J. Rouquerol, D. Avnir, C. W. Fairbridge, D. H. Everett, J. H. Haynes, N. Pernicone, J. D. F. Ramsay, K. S. W. Sing and K. K. Unger, *Pure Appl Chem*, 1994, **66**, 1739-1758.
- [26] R. Ryoo, S. H. Joo, M. Kruk and M. Jaroniec, *Adv Mater*, 2001, **13**, 677-681.

- [27] R. Ryoo, S. H. Joo and S. Jun, *J Phys Chem B*, 1999, **103**, 7743-7746.
- [28] K. S. Xia, Q. M. Gao, C. D. Wu, S. Q. Song and M. L. Ruan, *Carbon*, 2007, **45**, 1989-1996.
- [29] Y. H. Zhang, A. Q. Wang and T. Zhang, *Chem Commun*, 2010, **46**, 862-864.
- [30] H. S. Zhou, S. M. Zhu, M. Hibino, I. Honma and M. Ichihara, *Adv Mater*, 2003, **15**, 2107-2111.
- [31] K. S. Xia, Q. M. Gao, J. H. Jiang and J. Hu, *Carbon*, 2008, **46**, 1718-1726.
- [32] S. Xin, L. Gu, N. H. Zhao, Y. X. Yin, L. J. Zhou, Y. G. Guo and L. J. Wan, *J Am Chem Soc*, 2012, **134**, 18510-18513.
- [33] H. L. Wang, Y. Yang, Y. Y. Liang, J. T. Robinson, Y. G. Li, A. Jackson, Y. Cui and H. J. Dai, *Nano Lett*, 2011, **11**, 2644-2647.
- [34] G. J. Hu, C. Xu, Z. H. Sun, S. G. Wang, H. M. Cheng, F. Li and W. C. Ren, *Adv Mater*, 2016, **28**, 1603-1609.
- [35] F. Wu, S. X. Wu, R. J. Chen, S. Chen and G. Q. Wang, *Chinese Chem Lett*, 2009, **20**, 1255-1258.
- [36] M. M. Sun, S. C. Zhang, T. Jiang, L. Zhang and J. H. Yu, *Electrochem Commun*, 2008, **10**, 1819-1822.
- [37] J. L. Wang, J. Yang, C. R. Wan, K. Du, J. Y. Xie and N. X. Xu, *Adv Funct Mater*, 2003, **13**, 487-492.
- [38] J. L. Wang, J. Yang, J. Y. Xie and N. X. Xu, *Adv Mater*, 2002, **14**, 963-965.
- [39] X. U. Yu, J. Y. Xie, Y. Li, H. J. Huang, C. Y. Lai and K. Wang, *J Power*

*Sources*, 2005, **146**, 335-339.

[40] Z. W. Seh, W. Y. Li, J. J. Cha, G. Y. Zheng, Y. Yang, M. T. McDowell, P. C.

Hsu and Y. Cui, *Nat Commun*, 2013, **4**, 1331.

[41] X. Liang, A. Garsuch and L. F. Nazar, *Angew Chem Int Edit*, 2015,

**54**,3907-3911.

[42] Y. S. Su and A. Manthiram, *Nat Commun*, 2012, **3**, 1166.

[43] J. Q. Huang, T. Z. Zhuang, Q. Zhang, H. J. Peng, C. M. Chen and F. Wei,

*Acs Nano*, 2015, **9**, 3002-3011.

[44] R. K. Joshi, P. Carbone, F. C. Wang, V. G. Kravets, Y. Su, I. V. Grigorieva,

H. A. Wu, A. K. Geim and R. R. Nair, *Science*, 2014, **343**, 752-754.

[45] K. Raidongia and J. X. Huang, *J Am Chem Soc*, 2012, **134**, 16528-16531.

[46] A. Lerf, A. Buchsteiner, J. Pieper, S. Schottl, I. Dekany, T. Szabo and H. P.

Boehm, *J Phys Chem Solids*, 2006, **67**, 1106-1110.

[47] M. Vijayakumar, N. Govind, E. Walter, S. D. Burton, A. Shukla, A. Devaraj,

J. Xiao, J. Liu, C. M. Wang, A. Karim and S. Thevuthasan, *Phys Chem Chem Phys*,

2014, **16**, 10923-10932.

[48] H. B. Yao, K. Yan, W. Y. Li, G. Y. Zheng, D. S. Kong, Z. W. Seh, V. K.

Narasimhan, Z. Liang and Y. Cui, *Energ Environ Sci*, 2014, **7**, 3381-3390.

[49] H.-J. Peng, D.-W. Wang, J.-Q. Huang, X.-B. Cheng, Z. Yuan, F. Wei and Q.

Zhang, *Advanced Science*, 2015,1, 1500268.

[50] B. J. Holliday and C. A. Mirkin, *Angew Chem Int Edit*, 2001, **40**, 2022-2043.

- [51] G. F. Swiegers and T. J. Malefetse, *Chem Rev*, 2000, **100**, 3483-3537.
- [52] H. Li, M. Eddaoudi, M. O'Keeffe and O. M. Yaghi, *Nature*, 1999, **402**, 276-279.
- [53] D. N. Dybtsev, H. Chun and K. Kim, *Angew Chem Int Edit*, 2004, **43**, 5033-5036.
- [54] B. L. Chen, M. Eddaoudi, S. T. Hyde, M. O'Keeffe and O. M. Yaghi, *Science*, 2001, **291**, 1021-1023.
- [55] M. Eddaoudi, D. B. Moler, H. L. Li, B. L. Chen, T. M. Reineke, M. O'Keeffe and O. M. Yaghi, *Accounts Chem Res*, 2001, **34**, 319-330.
- [56] D. Zhao, D. J. Timmons, D. Q. Yuan and H. C. Zhou, *Accounts Chem Res*, 2011, **44**, 123-133.
- [57] B. L. Chen, S. C. Xiang and G. D. Qian, *Accounts Chem Res*, 2010, **43**, 1115-1124.
- [58] B. L. Chen, X. Zhao, A. Putkham, K. Hong, E. B. Lobkovsky, E. J. Hurtado, A. J. Fletcher and K. M. Thomas, *J Am Chem Soc*, 2008, **130**, 6411-6423.
- [59] C. Fang, Q. K. Liu, J. P. Ma and Y. B. Dong, *Inorg Chem*, 2012, **51**, 3923-3925.
- [60] S. Y. Bai, T. L. Sheng, C. H. Tan, Q. L. Zhu, Y. H. Huang, H. Jiang, S. M. Hu, R. B. Fu and X. T. Wu, *J Mater Chem A*, 2013, **1**, 2970-2973.

# Chapter 2. A zinc(II)-metal-organic framework based separator

## 2.1 Introduction

The emerging energy demand has attracted increasing interest in rechargeable batteries. <sup>[1,2]</sup> Lithium–sulfur batteries have been regarded as one of the most promising energy-storage candidates, for their vitally advantageous economy, environmental friendliness and high-energy density. <sup>[3]</sup> The high theoretical specific capacity (1673 mA h g<sup>-1</sup>) of lithium–sulfur batteries have far exceeded that of the current lithium-ion batteries, which has already approached to their theoretical limits. However, the electrochemical intermediates, involved in lithium sulfur batteries, (a series of soluble long-chain lithium polysulfides and insoluble short-chain lithium polysulfides), have resulted in unfavourable “shuttle” effects, low coulombic efficiency, low sulfur utilization, and poor cycling performance, all of which have hindered its potential development in practical applications. <sup>[3–5]</sup>

Aiming to overcome this challenge, a wide range of typical researches have been concentrated on developing sulfur carriers, such as porous carbon, <sup>[6–8]</sup> graphene-derived materials, <sup>[9–12]</sup> conductive polymers <sup>[13–15]</sup> and transition metal oxides. <sup>[16–18]</sup> Conventional emphasis on cathodes, to some extent, has been unable to effectively retain polysulfide in lithium–sulfur batteries. Inevitably, it has been confronted with continuous sulfur dissolution into the electrolyte over time, coupled with critical capacity decay, particularly in long-term cycles. <sup>[1,3]</sup>

Conceptually, development of a new functional separator for the lithium–sulfur battery is regarded as an alternative approach in contrast to the complicated synthesis or surface modification of cathode materials. <sup>[19–21]</sup> As a part of our longstanding interest in separator technology, we have continuously concentrated on designing and synthesizing functional separators for soluble polysulfide in lithium–sulfur batteries. <sup>[22]</sup> Recently, we have firstly reported the metal–organic framework based separator in lithium–sulfur batteries. <sup>[23]</sup> The hybrid nature of MOF results in a series of porous materials with high surface area and tunable porosity, constructed by metal ions and

organic ligands. <sup>[24–26]</sup> Due to its highly-ordered porosity, large surface area and ionic selectivity based on size and shape, MOF is one of the most appropriate building blocks for separators in lithium–sulfur batteries. On the basis of open metal sites and the ligands' functional groups, the infiltrating metal–organic compounds can act as a highly-efficient selective carrier, displaying outstanding molecular/ionic transferring capability. <sup>[26,27]</sup>

What remained to be demonstrated is whether this MOF candidate might provide an attractive performance, stability and robustness to influence its capability in electrochemistry. Hence, an isostructural Zn(II)-based framework was preferred and further generated for its microporous structures. <sup>[28,29]</sup> The divalent zinc ion was regarded as a promising metal center due to its approximate coordination and geometry capabilities. Accordingly, the structural skeleton of a Zn(II)-based MOF was constructed with the same organic ligand (benzene-1,3,5-tricarboxylic acid, BTC). Its prototypical 3-dimensional structure was constructed by analogous binuclear Zn(II) paddlewheel subunits with interconnected carboxylate groups. The amount of water molecules existing in the framework was also equal. More importantly, the advantageous characteristics of perfectly high-ordered micropores ( $\sim 9 \text{ \AA}$ ) were certainly conserved; these pores are rationally smaller than the diameters of soluble lithium polysulfides ( $\text{Li}_2\text{S}_n$ ,  $4 < n \leq 8$ ). Due to the reliable interaction between carboxylic groups and the zinc centers in skeletons, the balanced electrical neutrality also introduced an equal stability and robustness under electrochemical conditions.

In this study, we synthesized one novel and highly-efficient ionic sieving separator for lithium–sulfur batteries. The self-assembled Zn(II)-based MOF@GO separator is designed and introduced to sufficiently minimize the soluble polysulfide migrating to the anode. It further demonstrates prolonged cycling performance and enhanced high-rate capability at a current of 1C over 1000 cycles in a lithium–sulfur battery, resulting in lower capacity fading rates and longer cycling life for traditional cathode composites containing up to 70 wt% sulfur, without elaborate synthesis or surface modification of composites. In addition, we have also investigated the infrared spectra (IR) of the Zn(II)-based MOF@GO separator. After charging over 100 cycles, Zn–S

bonds were formed that have been found to effectively stabilize the MOF structures under electrochemical conditions.

## 2.2 Experiment and Characterization

### 2.2.1 Chemicals

All chemicals, including 1,3,5-benzenetricarboxylic acid (BTC) (99.5%),  $\text{Cu}(\text{NO}_3)_2 \cdot 3\text{H}_2\text{O}$  (99.5%), N,N-dimethylformamide (DMF) (99.8%), ethanol (99.8%), 1,3-dioxacyclopentane (DOL 99.8%), 1,2-dimethoxyethane (DME 99.8%), and LiTFSI (lithium bis(trifluoromethanesulfonyl)imide 99.9%) were commercially purchased from TCI Chemicals without further purification. Graphene oxide (GO) was prepared from natural graphite powder (> 99.8%, Alfa Aesar) via a modified version of Hummers' method. The filter membrane (47 mm, 0.2  $\mu\text{m}$ ) and Millipore filter systems were obtained from Millipore Co. Ltd.

### 2.2.2 Preparation of Sulfur cathode (CMK-3@S)

Ordered mesoporous carbon (CMK-3) was firstly reported by Ryoo et al. in 1999, produced by SBA-15 silica as the template and sucrose as the carbon source under hydrothermal conditions. Since the *L. F. Nazar* et al. first reported with CMK-3 as cathode sulfur host in 2009, the development of the novel cathode structural design has attracted a huge number of attentions. The host of highly ordered CMK-3 illustrates uniform pore sizes, high pore volume, and high conductivity. The synthesizing methods for sulfur-containing CMK-3@S composites can be classified as sulfur/carbon mixture, sulfur-melting route, and sulfur immersion.

The CMK-3/S composite was prepared as previously reported, following a melt-diffusion strategy. CMK-3 (1.0 g) and sulfur (2.33 g) were mixed and ground

together, and heated to 155 °C. The weight ratio of sulfur/carbon was adjusted to be approximately 7:3, to allow for 70 wt% sulfur content. Because of the density of  $\text{Li}_2\text{S}$  ( $1.66 \text{ g cm}^{-3}$ ), 1.0 g of CMK-3 ( $2.1 \text{ cm}^3 \text{ g}^{-1}$ , the pore volume of the CMK-3) can accommodate 3.486 g of  $\text{Li}_2\text{S}$ , which corresponds to a maximum of 2.425 g of sulfur.

The process was illustrated as follows:

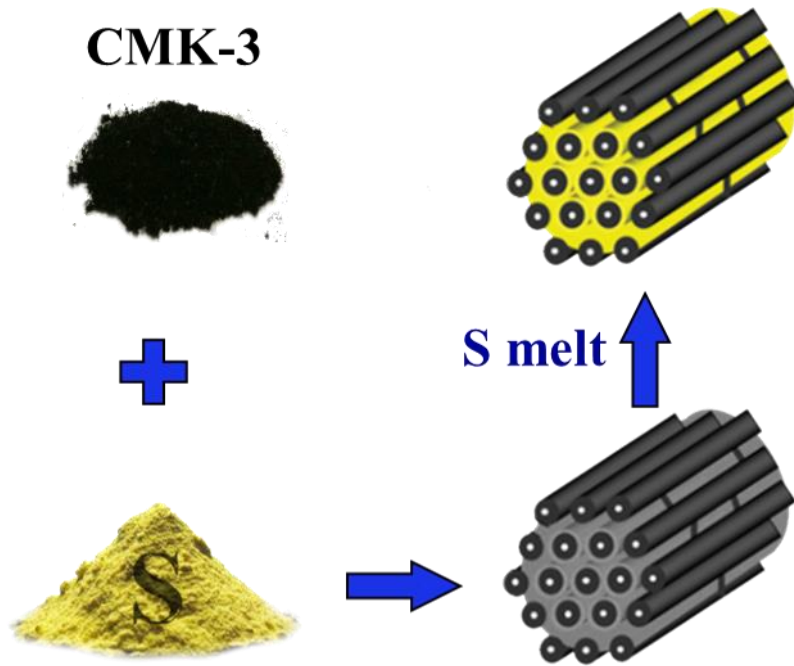


Fig. 2.1. Synthesizing process of sulfur cathode materials (CMK-3@S sulfur cathode materials)

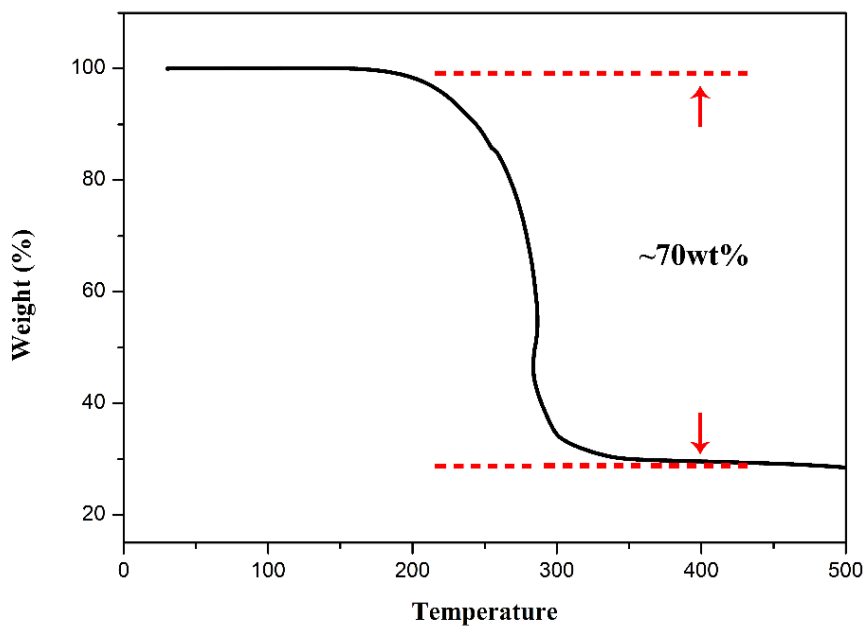


Fig. 2.2. Thermogravimetric analysis. The wt% of sulfur in the CMK-3/S composite was determined to ~70%, respectively.

The sulfur content was measured by the thermogravimetric analysis (TGA) from room temperature to 800 °C with a heating rate of 2 °C/min<sup>-1</sup> under nitrogen flow.

### 2.2.3 The fabrication of coin cell and CV measurement of lithium-sulfur batteries

Common 2032-type coin cells were assembled in an argon-filled glove box and lithium metal foil was used as the counter electrode. In comparison, mesoporous carbon was chosen as the sulphur carrier. Working electrode materials were mixed as follows: the sulphur-containing cathode materials (CMK-3/S composite), carbon black (Super P), and poly(vinylidene fluoride) (PVDF) binder into N-methyl-2-pyrrolidone (NMP) with a mass ratio of 8:1:1. The sulphur/CMK-3 (70 wt%) was prepared according to a typical melt-diffusion strategy.<sup>2</sup> In our experiments, the electrolyte was prepared with 1 M LiTFSI and 0.1 M LiNO<sub>3</sub> in 1:1(v/v) 1,2-dimethoxyethane (DME) and 1,3-dioxacyclopentane (DOL).<sup>4,31</sup> The pristine separator was Celgard 2400.

Cyclic voltammetry (CV) is one kind of electrochemical measurement by potentiodynamic scan. The potential of sulfur cathode (Lithium-sulfur batteries) is scanned linearly versus time. In the CVs, the extended cutoff voltage has been measured between 1.5 and 3.0 V. The set potential will return to the initially potential after CV scanning in lithium-sulfur batteries. In experimental, CV measurements have been conducted by Solatron electrical station. The CV curve in lithium sulfur battery with a MOF@GO separator is at a scan rate of 0.1 mV s<sup>-1</sup>. The lithium-ion diffusion rate has also been measured by different scanning rates, ranging from 0.1 mV s<sup>-1</sup> to 0.2 mV s<sup>-1</sup>.

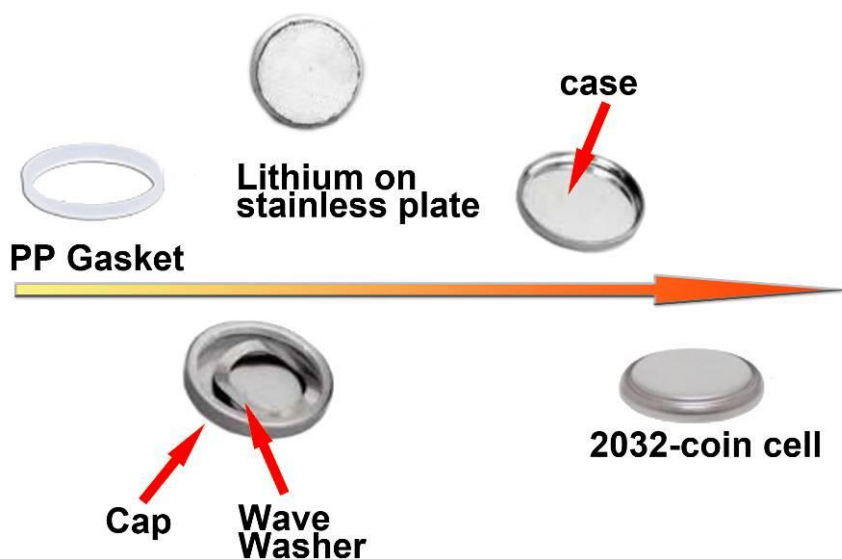


Fig. 2.3. The fabrication of 2032-coin cell in lithium-sulfur batteries.

#### 2.2.4 Characterization

The PXRD data was collected at ambient temperature on a Bruker D8 Advanced diffractometer (40 kV, 40 mA) for Cu  $K\alpha$  ( $\lambda = 1.5418 \text{ \AA}$ ), with a scan speed of 1 sec/step, a step size of  $0.05^\circ$  in  $2\theta$  ( $5\text{-}60^\circ$ ). Elemental analyses (sulfur) were performed with a Vario MICRO CHNOS Elemental Analyzer. Thermal analysis was performed on a NETZSCH STA 449C instrument from room temperature to  $800^\circ\text{C}$  with a heating rate of  $2^\circ\text{C}/\text{min}^{-1}$  under nitrogen flow. SEM studies analyses were conducted on a Scanning Electron Microscope of JSM6700-F, Field Emission Scanning Electron Microscope. The infrared spectra (KBr pellets) was conducted on a Bruker VERTEX70 FT-IR spectrometer in the range of  $4000\text{-}400 \text{ cm}^{-1}$ .

#### 2.2.5 Fabrication process of Zn(II)-MOF@GO separator

The Zn-MOF@GO separator was synthesized according to the method given in a previous report. Synthesis of Zn-HKUST-1 nanoparticles was prepared similarly: Zinc(II) nitrate hexahydrate ( $\text{Zn}(\text{NO}_3)_2 \cdot 6\text{H}_2\text{O}$ ) (1.190 g, 4 mmol) and 1,3,5-benzenetricarboxylic acid (0.42 g, 2 mmol) were mixed. These Zn-MOF crystalline particles were self-assembled on the surface by vacuum filtration

(Millipore, 47mm, 0.2 $\mu$ m). The MOF thin film was formed on the filter membrane. In contrast, the reaction time for the Zn-MOF is further prolonged due to the relatively lower coordination ability.

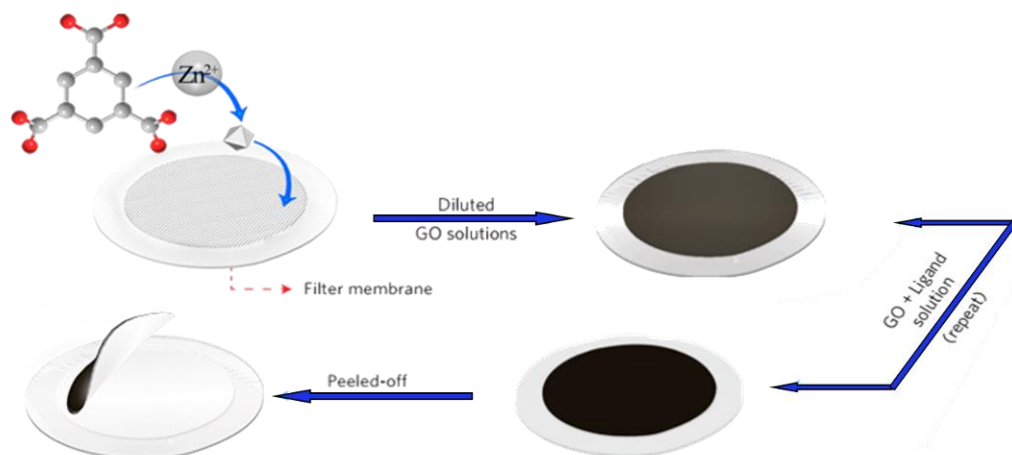


Fig. 2.4. Fabrication process of Zn(II)-MOF@GO separators.

In contrast, the reaction time for the Zn ions is further prolonged due to the relatively lower coordination ability. The GO layer was manufactured by vacuum filtration of a certain amount of GO suspension (0.1mg mL<sup>-1</sup>). The GO laminates retained on top of the MOF membrane could not only strengthen the permeation barrier, but also provide a strong support for improving the stability as a separator. After filtration, the in-situ fabricated separator was washed thrice by anhydrous ethanol solutions and then peered off from the filter.

The novel separator comprising Zn<sub>3</sub>(BTC)<sub>2</sub> integrated with graphene oxide (abbreviated as MOF@GO) was synthesized [23,28]. The Zn(II)-based (Zn-HKUST-1) MOF@GO separator has been synthesized similarly as the step-by-step fabricating process. After filtering a certain number of diluted GO solution, GO layers was formed on top of the MOFs layer. The GO layer was manufactured by vacuum filtration of a certain amount of GO suspension (0.1mg mL<sup>-1</sup>).

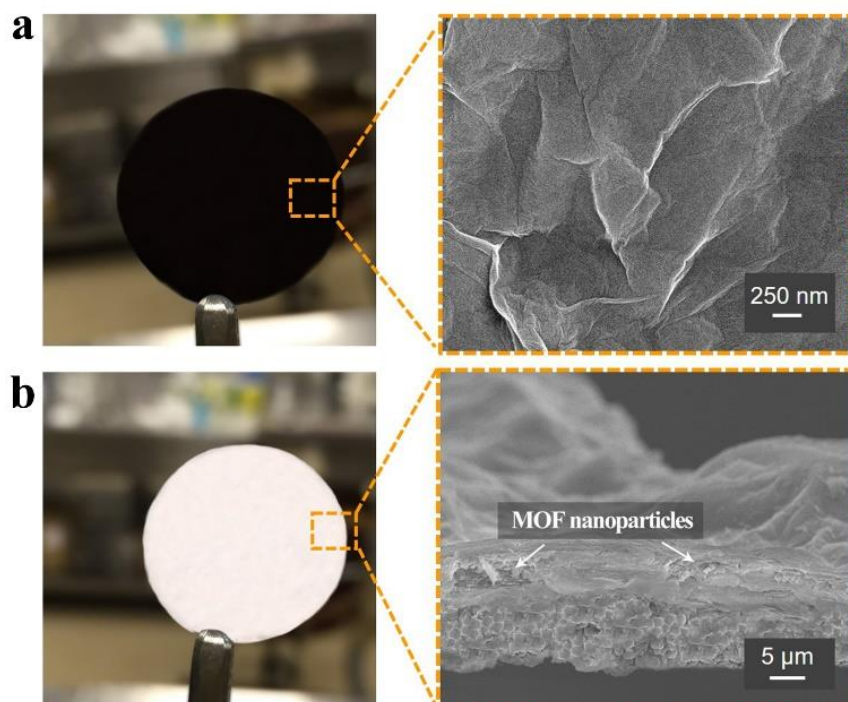


Fig. 2.5. (a) Digital photo of upper GO laminates. The inset shows a SEM image along the GO side. (Scale bar, 250 nm). (b) Digital photo of cross-section Zn-based MOF@GO separator. The inset shows a SEM image along the MOF side. (Scale bar, 5 μm)

A series of homogeneous MOF crystalline nanoparticles were regularly self-assembled and retained under the layered GO laminates. The GO laminates retained on top of the MOF membrane could not only strengthen the permeation barrier, but also provide a strong support for improving the stability as a separator. The nano-sized crystals continued growing under the paralleled GO layers, resulting in a well-prepared MOF@GO separator. After filtration, the in-situ fabricated separator was washed thrice by anhydrous ethanol solutions and then peeled off from the filter membrane.

### 2.2.6 Permeation experiments of Zn(II)-MOF@GO separator

In the permeation experiment, the home-made V-tube device with Celgard 2400 separator and Zn(II)-MOF@GO separator was prepared. A polysulfide solution (0.1

M,  $\text{Li}_2\text{S}_6$ ) and blank electrolyte were injected into the units. Permeation with Celgard 2400 separator tended to malfunction within 2 hours. In contrast, permeation with MOF@GO separator still retained its resistance and the scarlet polysulfide solution stayed at the same level over 48 hours. The Zn(II)-based MOF@GO separator was likely to effectively limit polysulfide ions within the left tube, and no evident colour change in the right side was observed, indicating efficient suppression of polysulfide permeation by the Zn(II)-based MOF@GO separator.

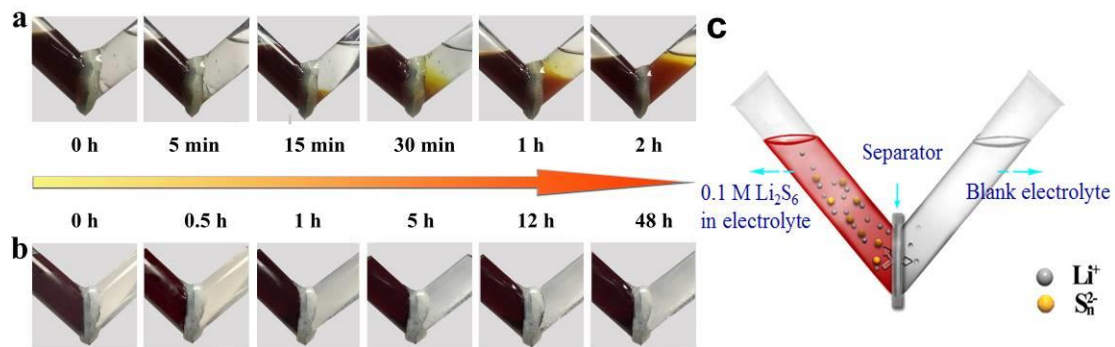


Fig. 2.6 (a) The permeation with the pristine separators (Celgard 2400 separator); (b) The permeation with the MOF@GO separators; (c) The permeation mode with the separators.

And we have made one more permeation experiments with original separator (Celgard 2400 separator). As depicted in Fig. 2.5, it is significantly obvious that the first group with pristine Celgard separator was measured under room temperature. It is obvious that polysulfide ions were continuously diffused through the interlayer, then the vivid scarlet solutions gradually occupied the whole blank counterparts step by step in the next 2 h. In comparison, the first group with Zn-MOF@GO separators, no obvious polysulfide permeation can be detected under the similar conditions. The polysulfide ions were found to be impossible to pass through such MOF@GO separators even within 48 hours. The blank electrolyte in the right side keeps clear all the time.

## 2.3 Results and Discussion

### 2.3.1 Confirmation of MOF particles

According to its PXRD spectra (Fig. 2.6), it also remains consistent with the Zn(II)-based MOF structures. These Zn(II) based particles were also self-assembled along the preferred crystalline (200) direction, in agreement with its crystal growth mechanism [23,24]. Owing to the great hindrance along vertical and horizontal directions, the cuboctahedron should illustrate the superior domination along the crystal facts of {001} and {111}. As depicted, the potential channels can provide the larger window size of  $\sim 9 \text{ \AA}$ . These highly ordered pores have been well regulated along the (001) direction, which is rationally smaller than the diameters of lithium polysulfide ( $\text{Li}_2\text{S}_n$ ,  $4 < n \leq 8$ ).

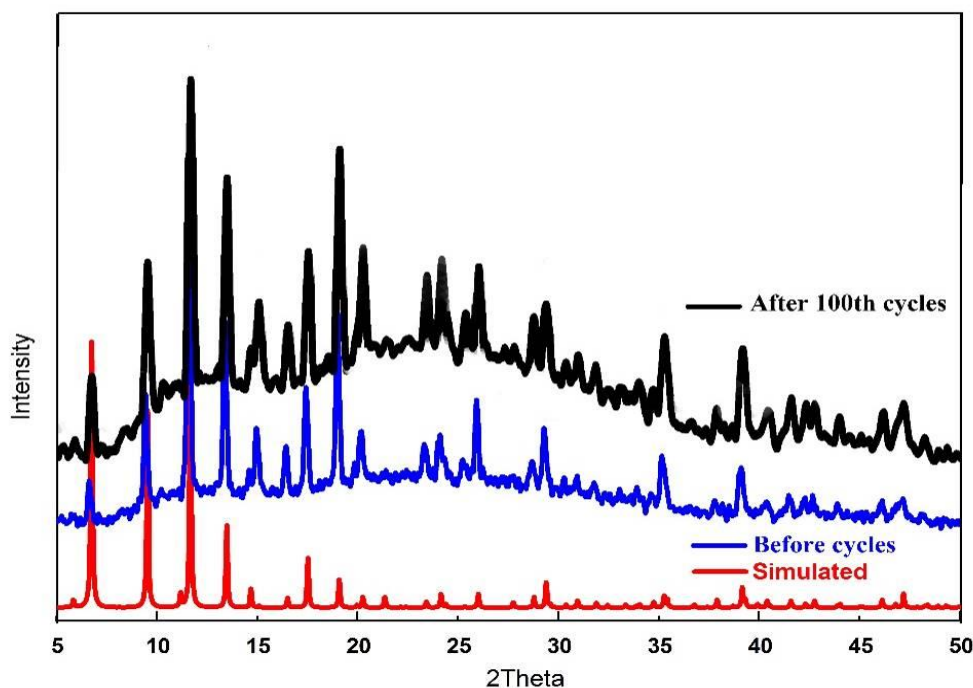


Fig. 2.7. The PXRD patterns of MOF@GO separators. The MOF structural skeleton remains intact during the discharge/charge process over 100 cycles

### 2.3.2 Electrochemical stability of Zn-MOF@GO separator

Cyclic voltammetry (CV) experiments were performed with a Solartron station. The extended cut-off voltage was measured between 1.5 and 3.0 V in the

lithium–sulfur batteries. As depicted in Fig. 2.7., the CV plots of the lithium–sulfur battery with Zn(II)-based MOF@GO separators were measured at the scan rate of  $0.1 \text{ mV s}^{-1}$ . The two anodic peaks at  $\sim 2.3 \text{ V}$  and  $1.9 \text{ V}$  corresponded to the reduction of elemental sulfur to soluble lithium polysulfide ( $\text{Li}_2\text{S}_n$ ,  $4 < n \leq 8$ ) and the eventual formation of insoluble  $\text{Li}_2\text{S}_2$  and  $\text{Li}_2\text{S}$ .

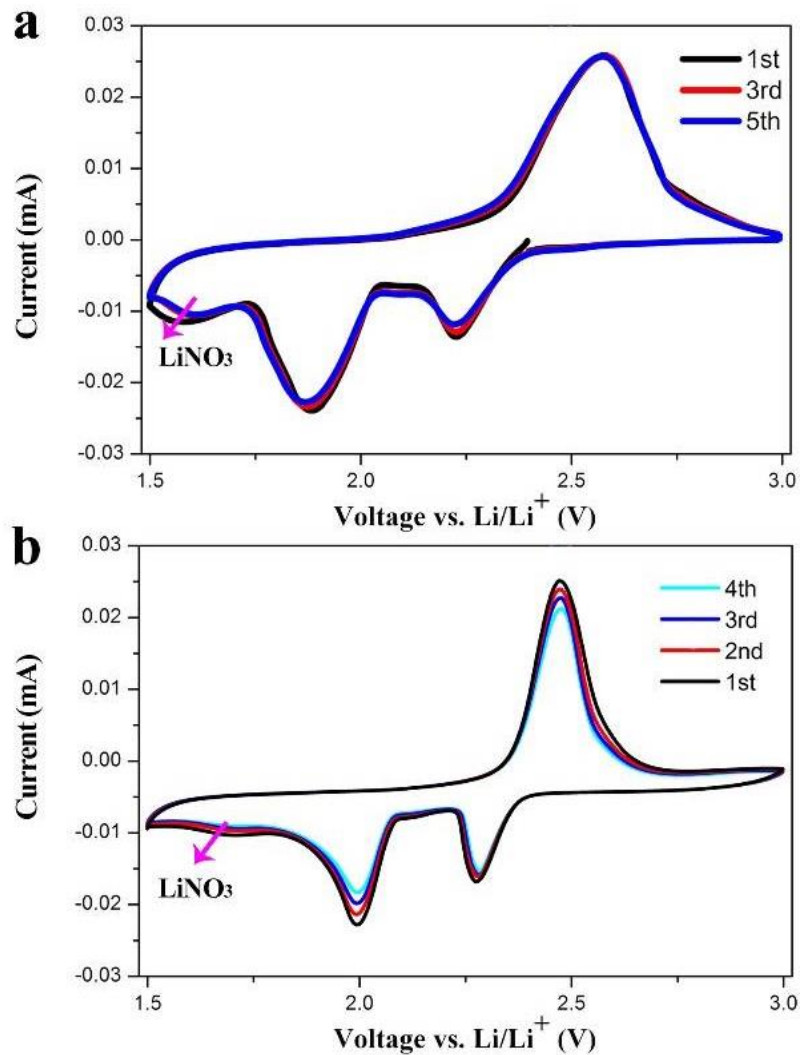


Fig. 2.8. The CVs in lithium sulfur batteries with (a) a MOF@GO separator at a scan rate of  $0.1 \text{ mV s}^{-1}$  and (b) a pristine separator (Celgard 2400) at a scan rate of  $0.1 \text{ mV s}^{-1}$ .

Due to the presence of  $\text{LiNO}_3$ , an irreversible reduction at  $\sim 1.6 \text{ V}$  was observed in the initial cycles, and disappeared in the subsequent cycles. <sup>[31,32]</sup> The subsequent cathodic peak, depicted as one strong and broad peak, underwent a slight shift to  $\sim 2.6$

V. These overlapped CV peaks illustrated the excellent electrochemical performance of the cells, revealing high stability and efficiency of the separators without parasitic reactions.

In our experiments, the electrolyte was prepared with 1 M LiTFSI and 0.1 M LiNO<sub>3</sub> in 1:1 (v/v) 1,2-dimethoxyethane (DME) and 1,3-dioxacyclopentane (DOL). In the CVs, the extended cutoff voltage has been measured between 1.5 and 3.0 V in the lithium-sulfur batteries. The CV curve in lithium sulfur battery with a MOF@GO separator is at a scan rate of 0.1 mV s<sup>-1</sup>.

Experimentally, there observed no evident changes in peak intensities or locations in the CVs over 5 cycles (with Zn-MOF@GO separator). It is seemed to illustrate excellent cycle stability and preferable consistency, indicative of high sulfur utilization in lithium sulfur batteries with the MOF-based separators. In contrast, the peak intensity with pristine separator (Celgard 2400 separator) obviously decreased over 4 cycles.

Towards the peak shift, it can be regarded that the MOF modified separators illustrate excellent capability to block these dissolved polysulfide, coupling with the high polarization simultaneously. It is noteworthy that the introduced polarization in lithium-sulfur battery has resulted from the main difference among the charge curves at different rates, similar to a series of reports.

### 2.3.3 Molecular properties of Zn-MOF@GO separator

In fact, insight into the inherent difference in structural analysis is provided because of the similar paddlewheel-like skeletons. To further investigate the roles that these MOF particles have played in the electrochemical process, the IR spectra have been studied. All of these MOF samples were collected from the self-assembled MOF@GO separators in the glove box, individually.

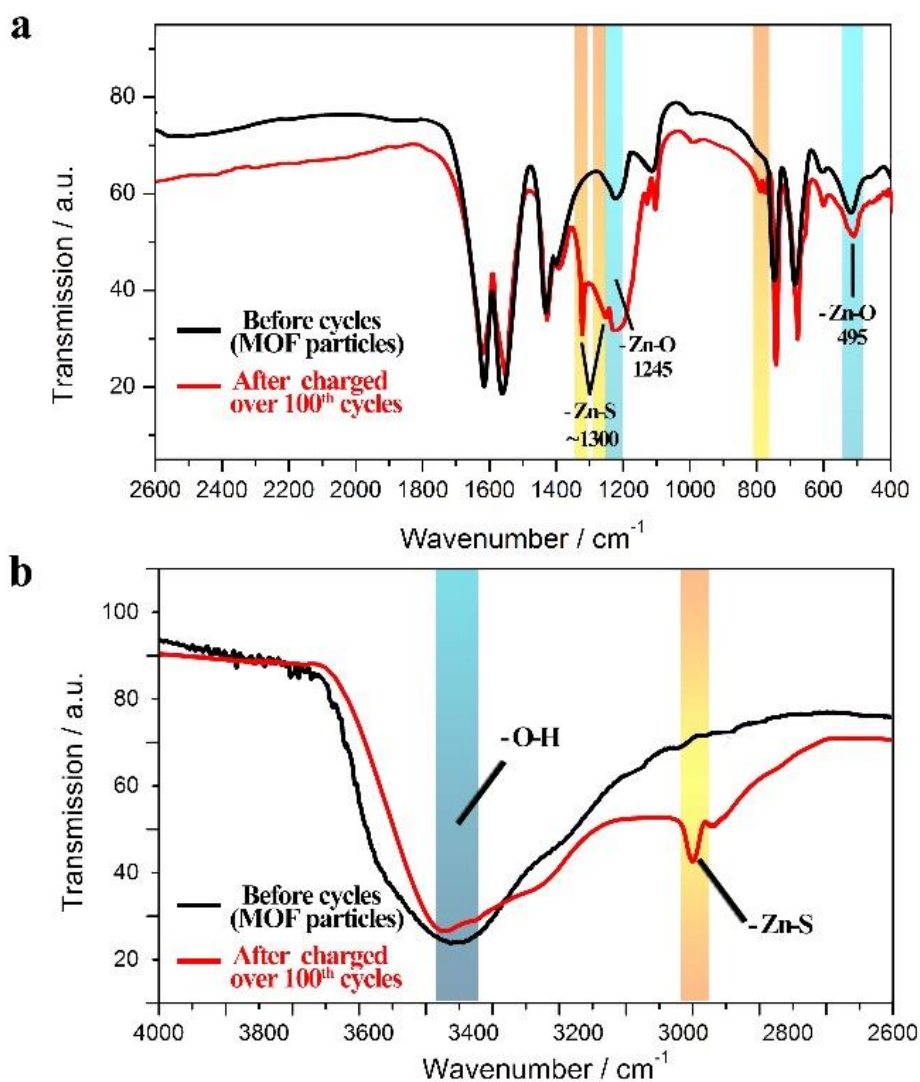


Fig. 2.9. The analyses based on the IR spectra. (a) Before/after the electrochemical process, the IR spectra of the dehydrated MOF particles. (b) The IR spectra have been measured in the higher wavenumbers.

As illustrated in Fig. 2.8, their main adsorptions remain consistent with the initial values. Simultaneously, it is worth mentioning that some bands were attributed to Zn–S and Zn–O interference in our observed spectra. Because of the strong hydroxyl band in the carboxylic groups, the strong peak of –OH bond in the higher wavenumbers was highlighted. The weak peak of the Zn–S bond at  $3000\text{ cm}^{-1}$  was also observed. The adsorptions in the next region at  $1323\text{ cm}^{-1}$  and  $1275\text{ cm}^{-1}$  also corresponded to Zn–S bonds. <sup>[33,34]</sup> Moreover, the two weaker characteristic peaks at  $798\text{ cm}^{-1}$  and  $781\text{ cm}^{-1}$  reflected the stretching vibrations of Zn–S groups.

In comparing the electrochemical performance and IR spectra, the important role that the MOF species might have played in lithium–sulfur batteries is further documented. Due to steric hindrance, the overwhelming majority of coordination sites of the Zn(II) dimers were occupied by oxygen groups from carboxylic acid; therefore, vacancies available for the formation of Zn–S bonds were significantly limited, and were mainly provided by the removal of water molecules from the porous cavities. According to the reported calculation, the Zn(II)-based MOF species also appeared to be properly stable structures. [28,29]

The formed Zn–S bond further addressed the primary result, which seemingly decreased the energy barrier of the structural skeletons. Moreover, the electrochemical performance varied with the energy status of the MOF structures and, undoubtedly, the Zn(II)–MOF based separator may owe its high performance to its stability. In structures, the dehydrated Zn(II)-based framework undergoes a change from square pyramidal geometry to a square planar coordination as compared to the stable structures of our previously reported Cu(II)-based MOF@GO separators, which may explain the preferable performance of the Cu(II)-based separators. [23]

In our experiment, the two samples of MOF particles are collected from the MOF@GO separators. The red curve is the IR spectra of the precursor MOF particles before the cycles. In comparison, the black curve is the IR spectra of the MOF particles after 100 discharge/charge cycles. Meanwhile, the peak of Zn-S bond appears in  $1323\text{cm}^{-1}$  and  $781\text{ cm}^{-1}$  after 100 cycles instead of that in the precursor MOF particles (The forming Zn-S bonds were highlighted with light yellow bar chart). In the revision, we have added one illustration about it.

In addition, the desulphurization role that ZnO has played also contributed to its structural instability and relatively imperfect electrochemical performance. [35,36] Despite this inadequate structural distortion or weak interconnection around divalent zinc geometric spheres, the Zn(II)-based MOF@GO separators in lithium–sulfur batteries can still act as highly-efficient ionic sieves and provide attractive performance in electrochemistry.

In our opinion, it is ineffective to have a redox reaction between the GO and

polysulfide ions ( $\text{Li}_2\text{S}_6$ ) at room temperature. We have searched a wide series of reports about the GO separator. In those cases, the GO separator is unable to remain resistance, to some extent, towards dissolved anions, because of its evanescent robustness in solutions over time rather than the redox reactions. It also has been certified by the SEM images.

### 2.3.4 Electrochemical performance

What remained to be demonstrated is whether the Zn(II)–MOF based separators might provide an attractive performance in electrochemistry. It will be a key factor in further understanding how the MOF-based separator functions. The dehydrated MOF@GO separator was used as a functional separator in lithium–sulfur batteries. Briefly, its performance mainly depended on its ionic sieving capability under electrochemical conditions.

As illustrated in Fig. 2.9, the long-term cycling stability of the cell was evaluated at a lower rate of 0.5C for 350 cycles. Galvanostatic charge/discharge cycling was conducted on a Hokuto measurement from 1.5–3.0V (versus  $\text{Li}^+/\text{Li}$ ). The sulfur mass loading was 0.6–0.8  $\text{mg cm}^{-2}$ .

In the initial activation process over 100 cycles, the discharge capacity witnessed a moderate drop. After that, it further provided a stable status in electrochemistry. Similarly, the capacity fading rate represented efficient restriction and excellent long-life cycling stabilities, which appears to be significantly slowed down in this stage. The cell delivered a high capacity of 1005  $\text{mA h g}^{-1}$  in the initial discharge. After cycling over 100, 200 and 350 cycles, the discharge capacity remained at  $\sim 818$   $\text{mA h g}^{-1}$ , 745  $\text{mA h g}^{-1}$  and 685  $\text{mA h g}^{-1}$ , respectively.

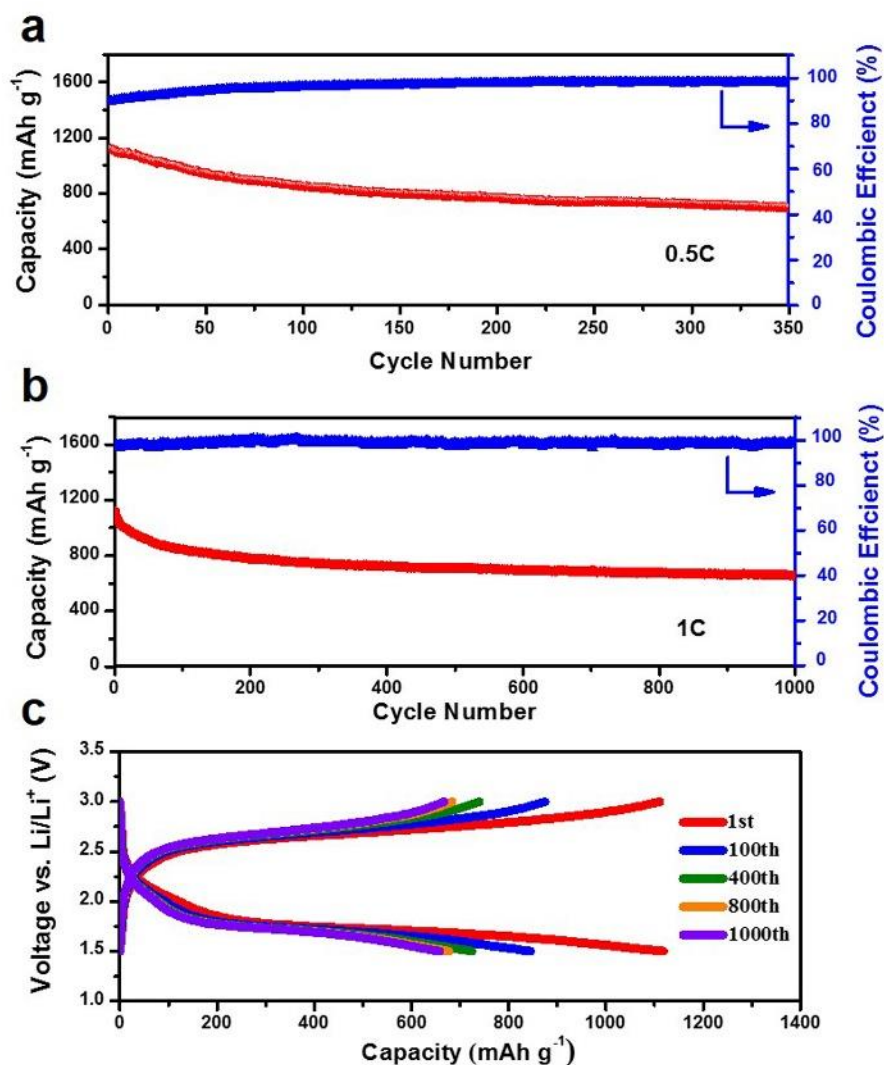


Fig. 2.10. Electrochemical performance of the lithium–sulfur cells. (a) Discharge capacity and Coulombic efficiency at the current rate of 0.5C over 350 cycles. (b) Discharge capacity and Coulombic efficiency at the current rate of 1 C over 1,000 cycles. (c) The voltage profiles at the rate of 1 C at the 1st, 100th, 400th, 800th and 1000th cycle, respectively.

To further demonstrate the advantages of the Zn(II)-based MOF@GO separator, the long-term electrochemical performance was measured at 1C over 1000 cycles (1C = 1673 mA g<sup>-1</sup>). After an initial discharge capacity of 1118 mA h g<sup>-1</sup>, its achieved capacity was 782 mA h g<sup>-1</sup>, 724 mA h g<sup>-1</sup>, 676 mA h g<sup>-1</sup> and 657 mA h g<sup>-1</sup> at the end of the 200<sup>th</sup>, 400<sup>th</sup>, 800<sup>th</sup> and 1000<sup>th</sup> cycle, respectively. The decrease in capacity during the first 100 cycles can be attributed to the gradual contact between the

mesoporous carbon and sulfur, and thus, an increase in sulfur utilization. More notably, the restricted fading capacity was  $125 \text{ mA h g}^{-1}$  in the range of the 200<sup>th</sup> to the 1000<sup>th</sup> cycle, representing a much lower capacity decay of 0.041% per cycle during the whole process, in agreement with the fading rate with our Cu(II)-based MOF@GO separator. [23]

The evident two-plateau behaviour in the discharge plots is still observed. According to the corresponding CV curves, the voltage profiles kept well-matched shapes with the increased charge potentials and decreased discharge potentials. The second discharge plateau still remained at  $\sim 1.75 \text{ V}$ .

We have added the potential of the two charge plateaus. And it is obvious that at lower rate of C/10, there still illustrates the obvious two-plateau behavior in the charging plots. With C-rates increased from C/10 C to 1C, both their voltage profiles keep well-matched shapes with the increased charge potentials and decreased discharge potentials.

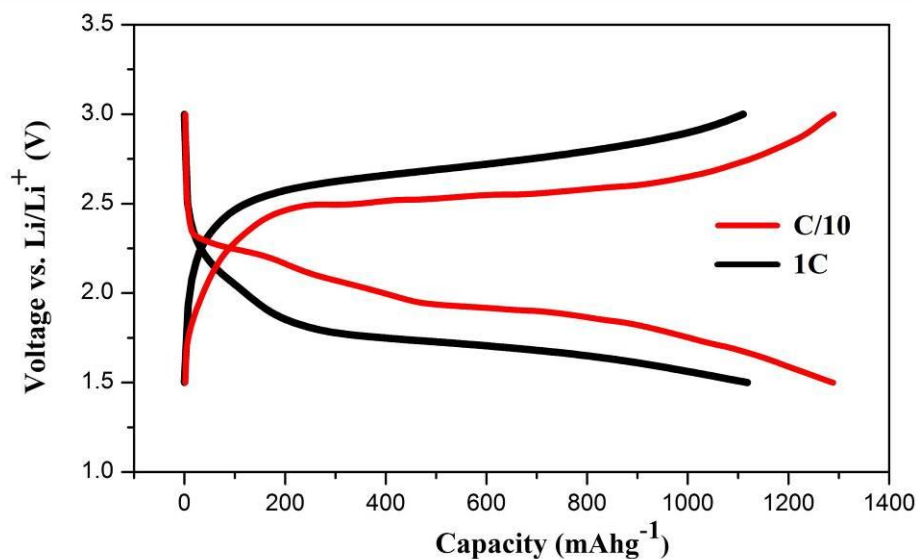


Fig. 2.11. The discharge/charge curves at C/10 and 1C with Zn-MOF@GO separators.

### 2.3.5 Further characterization of the MOF@GO separators

As depicted in Fig. 2.11, the surface morphology of the lithium metallic anodes before and after 1000 cycles was observed by SEM. The metallic lithium surface was still greatly flat, indicating that the MOF@GO separator could efficiently suppress the

formation of dissolved lithium polysulfide anions during long-life cycling process. The related permeation measurements and SEM images both displayed efficient resistance and notable rejection towards the dissolved polysulfide anions, which further greatly highlights the advantage of the Zn–MOF@GO separator.

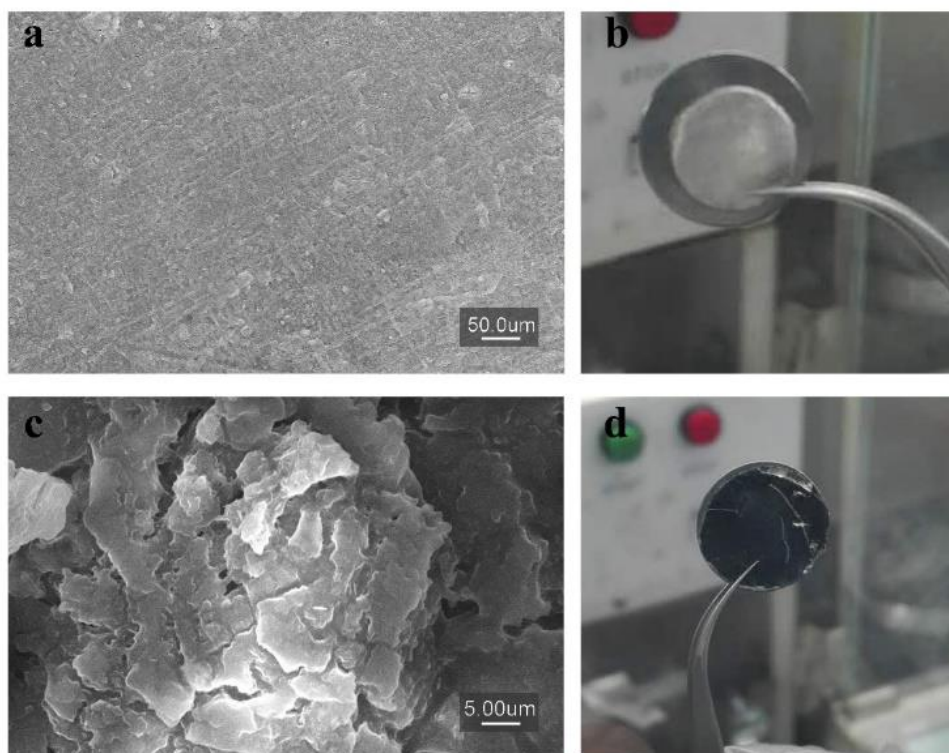


Fig. 2.12. SEM images of the lithium–metal surface before cycling (a) and after 1000 cycles (c). Photographs of lithium anode before cycling (b) and after 1000 cycles (d).

The charge plots illustrate non-typical two-plateau curves. Due to increased polarization and a relatively high energy barrier, it may mesh with the solution-to-solid phase transition from dissolved lithium polysulfide to elemental sulfur in lithium–sulfur batteries. Furthermore, it is worth mentioning that the MOF@GO separator appeared to continuously hold significant implications for suppressing the shuttle effects of soluble polysulfide in lithium–sulfur batteries. Simultaneously, the cell with MOF@GO separator still retained its relatively high  $\text{Li}^+$  diffusion kinetics and greatly enhanced sulfur utilization in electrochemistry.

In our opinion, the introduced MOF@GO separators is capable of restricting the polysulfide ions, which would tend to introduce great polarization in lithium-sulfur

batteries. It is also observed in our CVs and related charge plots with typical two-plateaus curves at lower C-rates (1/10C) and untypical curves at higher rates (1C).

However, in our opinion, the cells with our MOF-based separators would not cause the strong increase of lithium-ion transfer resistance, because the lithium–sulfur batteries with a MOF@GO separator can effectively offer excellent cycling performance at 1C over 1,000 cycles and provide well-matched discharge/charge curves in our manuscripts. In fact, considering its enhanced stability and long-term performance in lithium-sulfur batteries, it needs to remain its relatively high Li<sup>+</sup> diffusion kinetics.

Meanwhile, the shuttle effects of dissolved polysulfide ions would cause a poor rate performance and low cycle stability in conventional lithium-sulfur batteries. In fact, our MOF@GO separator is able to efficiently function towards the severe polysulfide dissolution. The excellent high-rate performance with the MOF@GO separator can be further understood through its nature of our MOF@GO separators.

These perfectly high-ordered micropores ( $\sim 9 \text{ \AA}$ ) are rationally smaller than the diameters of lithium polysulfide ( $\text{Li}_2\text{S}_n$ ,  $4 < n \leq 8$ ). This will satisfy the multi-purpose demand for effectively separating polysulfide ions, as its ionic radius is significantly larger, allowing for its enhanced long-life performance in lithium-sulfur batteries. Furthermore, it also corresponds to the permeation experiments. The MOF@GO separator can remain its resistance over 48 hours and the Celgard separator can only function less than 2 hours.

As depicted in Fig. 2.11, it is noteworthy that the surface morphology of the lithium metallic anodes before/after 1,000 cycles were observed by SEM. And the corresponding metallic lithium surface is still greatly flat, indicating that the MOF@GO separator could efficiently suppress dissolved lithium polysulfide anions during long-life cycling.

In fact, the related permeation measurements and SEM images both displayed efficient resistance and notable rejection towards the dissolved polysulfide anions, which further greatly highlights advantage about the Zn-MOF@GO separator.

In addition, the average coulombic efficiency still remains 98.8% over 1000 cycles, indicating that the separator can undoubtedly play an effective role as an ionic sieve toward polysulfide shuttle to the anode side. According to PXRD spectra, the structure of the MOF based separator remains intact. The MOF modified separators simultaneously exhibited excellent capability to block the soluble polysulfides and high polarization in lithium–sulfur battery. To better understand the redox behaviours during the discharge/charge process, when the current density remained as high as 1C, the voltage profiles of the 1<sup>st</sup>, 100<sup>th</sup>, 400<sup>th</sup>, 800<sup>th</sup> and 1000<sup>th</sup> cycle are illustrated in Fig. 2.10.

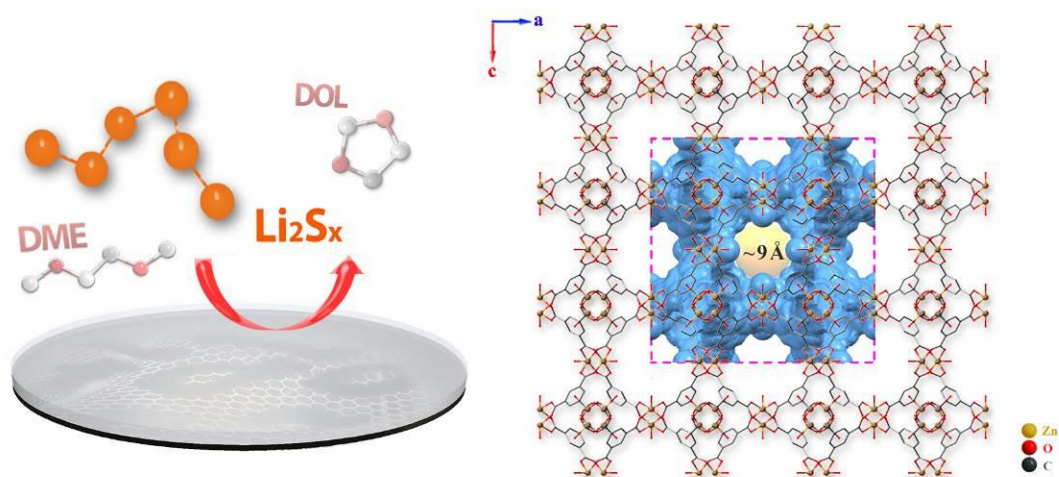


Fig. 2.13. Schematic of the Zn-based MOF@GO separator. The atomic stack (Right) illustrates the micropores.

To further investigate the stability of Zn(II)-MOF particles, the corresponding powder X-Ray Diffraction (PXRD) have been introduced before/after the electrochemical cycles. After immersing the MOF-based separator into the lithium-sulfur batteries over 100 cycles at the rate of 1C, the structural skeleton of MOF remains intact throughout the electrochemical process, as typical of pristine Zn-HKUST-1. Moreover, there still remains the forms of cuboctahedron as dominant crystalline configuration, in agreement with the pristine MOF based precursor. It further confirms the structural stability and reliability of MOF-based separators under

rigid conditions.

Owing to the great hindrance along vertical and horizontal directions, the cuboctahedron should illustrate the superior domination along the horizontal direction of {001} in our MOF@GO separator. Therein, its exposed crystalline facet of {001} was directed straightly to the vertical orientation. Following this self-assembly strategy, the MOF particles have witnessed the highly regular arrangements inside the separator. The potential channels can provide the larger window size of  $\sim 9 \text{ \AA}$ . These highly ordered pores have been well regulated along the (001) direction, which is rationally smaller than the diameters of lithium polysulfide ( $\text{Li}_2\text{S}_n$ ,  $4 < n \leq 8$ ).

In contrast, due to the intrinsic mechanical brittleness of the MOF, these particulate morphological crystals make it difficult to be peeled off from the substrate materials and further play the role as an ionic sieve. Hence, GO laminates are introduced to overcome this limitation, as they are easy to fabricate and are mechanically robust. The synergetic strategy has sufficiently regulated the cooperative nature of the stable porous structures and the flexible fabrications.

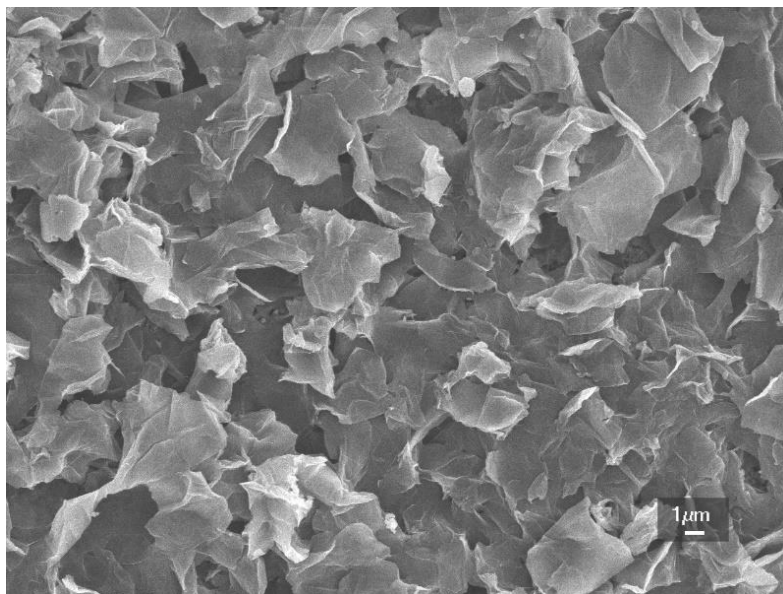


Fig. 2.14. SEM images of the GO laminates in MOF@GO separator. (After 100<sup>th</sup> charge/discharge cycles with GO separator) (Scale bar, 1 μm)

There are no obvious peak changes before/after the cycle in the PXRD spectra. On the basis of the steric hindrance, the overwhelming vacancy of the zinc sites were

occupied by oxygen groups from carboxylic acid. In comparison, the only affordable vacancy for the formation of Zn-S bond is significantly limited, mainly provided by the removing water molecules existed in the porous cavity. It seems to be comparable in terms of its lower energy with the more stable structures.

In fact, the polysulfide anions ( $\text{Li}_2\text{S}_x$ ) would be dissolved into lithium ions and polysulfide anions. Our MOF@GO separator could efficiently suppress dissolved lithium polysulfide anions in lithium-sulfur batteries. However, it has introduced subtle influence on the migration of lithium ions. And the MOF based separator may also embrace its stability in long-term cycles.

The desulfurization function of ZnO is an intriguing explanation. The capacity decaying of our Zn-MOF@GO separator is rather serious than that of Cu-MOF@GO separator in our previous work. In fact, the possible desulfurization of ZnO is also corresponding to our previous analyses that the weaker chemical bonding of Zn-S further results in the imperfect electrochemical cycling performance in lithium-sulfur batteries. And we have also added one explanation sentence in our manuscripts.

## 2.4 Conclusions

We synthesized a novel Zn(II)-based MOF@GO separator for lithium-sulphur batteries. It was able to function as a high-efficient ionic sieve toward polysulfide migrating across the separator and shuttling to the anode. Its electrochemical stability and lower capacity-fading rate is strikingly excellent, particularly in the long-term cycling process.

More importantly, it is found that the formed Zn-S bond would decrease the energy barrier and further stabilize the entire skeletons, in agreement with the observations of our previous Cu-based MOF@GO separator. The electrochemical performance of the separators in lithium-sulphur batteries reflects the subtle differences in their structures. Many more in-depth benefits may be realized in the design and development of functional MOF-based separators for energy-storage devices.

## 2.5 References

- [1]. P. G. Bruce, S. A. Freunberger, L. J. Hardwick and J. M. Tarascon, *Nat Mater*, 2012, **11**.
- [2]. X. L. Ji, K. T. Lee and L. F. Nazar, *Nat Mater*, 2009, **8**, 500-506.
- [3]. Y. X. Yin, S. Xin, Y. G. Guo and L. J. Wan, *Angew Chem Int Edit*, 2013, **52**, 13186-13200.
- [4]. S. S. Zhang, *J Power Sources*, 2013, **231**, 153-162.
- [5]. V. Etacheri, R. Marom, R. Elazari, G. Salitra and D. Aurbach, *Energ Environ Sci*, 2011, **4**, 3243-3262.
- [6]. S. R. Chen, Y. P. Zhai, G. L. Xu, Y. X. Jiang, D. Y. Zhao, J. T. Li, L. Huang and S. G. Sun, *Electrochim Acta*, 2011, **56**, 9549-9555.
- [7]. S. Xin, L. Gu, N. H. Zhao, Y. X. Yin, L. J. Zhou, Y. G. Guo and L. J. Wan, *J Am Chem Soc*, 2012, **134**, 18510-18513.
- [8]. C. F. Zhang, H. B. Wu, C. Z. Yuan, Z. P. Guo and X. W. Lou, *Angew Chem Int Edit*, 2012, **51**, 9592-9595.
- [9]. G. M. Zhou, L. Li, D. W. Wang, X. Y. Shan, S. F. Pei, F. Li and H. M. Cheng, *Adv Mater*, 2015, **27**, 641-647.
- [10]. H. L. Wang, Y. Yang, Y. Y. Liang, J. T. Robinson, Y. G. Li, A. Jackson, Y. Cui and H. J. Dai, *Nano Lett*, 2011, **11**, 2644-2647.
- [11]. L. W. Ji, M. M. Rao, H. M. Zheng, L. Zhang, Y. C. Li, W. H. Duan, J. H. Guo, E. J. Cairns and Y. G. Zhang, *J Am Chem Soc*, 2011, **133**, 18522-18525.
- [12]. Z. Y. Wang, Y. F. Dong, H. J. Li, Z. B. Zhao, H. B. Wu, C. Hao, S. H. Liu, J. S. Qiu and X. W. Lou, *Nat Commun*, 2014, .
- [13]. H. Li, M. Q. Sun, T. Zhang, Y. Q. Fang and G. C. Wang, *J Mater Chem A*, 2014, **2**, 18345-18352.
- [14]. K. Park, J. H. Cho, J. H. Jang, B. C. Yu, A. T. De la Hoz, K. M. Miller, C. J. Ellison and J. B. Goodenough, *Energ Environ Sci*, 2015, **8**, 2389-2395.
- [15]. X. W. Yu, J. Joseph and A. Manthiram, *J Mater Chem A*, 2015, **3**, 15683-15691.

- [16]. Z. W. Seh, W. Y. Li, J. J. Cha, G. Y. Zheng, Y. Yang, M. T. McDowell, P. C. Hsu and Y. Cui, *Nat Commun*, 2013, **4**.
- [17]. S. Meini, R. Elazari, A. Rosenman, A. Garsuch and D. Aurbach, *J Phys Chem Lett*, 2014, **5**, 915-918.
- [18]. Q. Pang, D. Kundu, M. Cuisinier and L. F. Nazar, *Nat Commun*, 2014, **5**.
- [19]. J. Balach, T. Jaumann, M. Klose, S. Oswald, J. Eckert and L. Giebeler, *Adv Funct Mater*, 2015, **25**, 5285-5291.
- [20]. J. Q. Huang, T. Z. Zhuang, Q. Zhang, H. J. Peng, C. M. Chen and F. Wei, *Acs Nano*, 2015, **9**, 3002-3011.
- [21]. Y. R. Li, L. X. Yuan, Z. Li, Y. Z. Qi, C. Wu, J. Liu and Y. H. Huang, *Rsc Adv*, 2015, **5**, 44160-44164.
- [22]. N. Li, Z. Weng, Y. R. Wang, F. Li, H. M. Cheng and H. S. Zhou, *Energ Environ Sci*, 2014, **7**, 3307-3312.
- [23]. S. Bai, X. Liu, K. Zhu, S. Wu and H. Zhou, *Nature Energy*, 2016, **1**, 16094.
- [24]. S. S. Y. Chui, S. M. F. Lo, J. P. H. Charmant, A. G. Orpen and I. D. Williams, *Science*, 1999, **283**, 1148-1150.
- [25]. L. Li, X. L. Liu, H. Y. Geng, B. Hu, G. W. Song and Z. S. Xu, *J Mater Chem A*, 2013, **1**, 10292-10299.
- [26]. S. Y. Bai, T. L. Sheng, C. H. Tan, Q. L. Zhu, Y. H. Huang, H. Jiang, S. M. Hu, R. B. Fu and X. T. Wu, *J Mater Chem A*, 2013, **1**, 2970-2973.
- [27]. V. Stavila, A. A. Talin and M. D. Allendorf, *Chem Soc Rev*, 2014, **43**, 5994-6010.
- [28]. M. K. Bhunia, J. T. Hughes, J. C. Fettinger and A. Navrotsky, *Langmuir*, 2013, **29**, 8140-8145.
- [29]. J. I. Feldblyum, M. Liu, D. W. Gidley and A. J. Matzger, *J Am Chem Soc*, 2011, **133**, 18257-18263.
- [30]. J. Yoo, S. J. Cho, G. Y. Jung, S. H. Kim, K. H. Choi, J. H. Kim, C. K. Lee, S. K. Kwak and S. Y. Lee, *Nano Lett*, 2016, **16**, 3292-3300.
- [31]. S. S. Zhang, *J Power Sources*, 2016, **322**, 99-105.
- [32]. S. S. Zhang, *Electrochim Acta*, 2012, **70**, 344-348.

- [33]. N. Ueyama, T. Sugawara, K. Sasaki, A. Nakamura, S. Yamashita, Y. Wakatsuki, H. Yamazaki and N. Yasuoka, *Inorg Chem*, 1988, **27**, 741-747.
- [34]. A. K. Verma, T. B. Rauchfuss and S. R. Wilson, *Inorg Chem*, 1995, **34**, 3072-3078.
- [35]. R. Ullah, P. Bai, P. P. Wu, Z. Q. Zhang, Z. Y. Zhong, U. J. Etim, F. Subhan and Z. F. Yan, *Energ Fuel*, 2016, **30**, 2874-2881.
- [36]. L. C. Huang, G. F. Wang, Z. F. Qin, M. X. Du, M. Dong, H. Ge, Z. W. Wu, Y. D. Zhao, C. Y. Ma, T. D. Hu and J. Wang, *Catal Commun*, 2010, **11**, 592-596.

# Chapter 3. A Cu(II)-Metal-Organic Framework-Based Separator

## 3.1 Introduction

The ever-growing demand for energy has pushed the development of energy storage technologies to go beyond lithium-ion batteries for higher energy density and a lower cost <sup>[1]</sup>. Because of the high theoretical specific capacity (1,673 mAh g<sup>-1</sup>) and natural abundance of sulfur, the lithium sulfur battery has recently been regarded as one of the most promising candidates for next-generation energy storage <sup>[2]</sup>. The major issue that hampers the lithium-sulfur battery from practical applications is the “shuttle effect” caused by the dissolution of the discharge/charge intermediates (i.e., various polysulfides) in organic electrolytes, consequently resulting in capacity loss of the sulfur cathode and poor cycle life of the battery. Aiming to address this issue, many efforts have been devoted to the development of porous composite cathode materials that are capable of immobilising polysulfides by encapsulating sulfur in porous carriers <sup>[3, 4]</sup>, such as carbon-based materials <sup>[5-7]</sup>, conductive polymers <sup>[8, 9]</sup>, transition metal oxides <sup>[10-12]</sup>, and metal-organic framework based materials <sup>[13-15]</sup>. These conventional sulfur carriers could, to some extent, prevent the escape of soluble polysulfides from the cathode. However, the cycle stability obtained to date has still been far from satisfactory because the volume change of the active mass of the cathode during discharge/charge cycling also causes problems. <sup>[16, 17]</sup>

The MOF represents a class of recently developed porous materials, composed of subunits of metal ions and organic ligands <sup>[22 - 27]</sup>. MOF-based materials are a type of well-known molecular sieve and have long been used for selective gas separation on a molecular scale. However, the use of MOF-based materials for a cathode as a porous host to contain sulfur may be an improper choice. The framework suffers from gradual malfunction and is unable to retard soluble polysulfides in batteries over time, especially after long-term cycling. The MOF containing sulfur endures great pressure from both the redox reactions and polysulfide dissolution when used as the cathode, possibly leading to further dramatic capacity decay and lower coulombic efficiency in

electrochemistry. In addition, the insulating nature of MOF-based materials and sulfur also hampers its success. A substantially higher conductivity additive should be added to improve the cathode conductivity, resulting in lower sulfur content and energy density in batteries.

While the dissolution of polysulfides in organic electrolytes appears to be inevitable, a useful approach to address this issue is to determine a method to block the shuttle pathway of polysulfides [17-21]. If a porous material with properly tuned pore sizes can act as a sieve to separate targeted ions on the basis of their sizes and shapes from an ionic solution, it may well be considered as an ionic sieve. MOF-based materials that have a large surface area and highly ordered pores with tuneable porosity would be appropriate candidates as ionic sieves to mitigate these shuttling polysulfide ions. In addition, MOF-based materials may also satisfy the electrical requirement in terms of its naturally insulating property, when used as separators in batteries.

However, due to the intrinsic mechanical brittleness of the MOF, these particulate morphological crystals make it difficult to fabricate an ideal ionic sieve membrane. Graphene oxide (GO) laminates are expected to overcome this limitation, as they are easy to fabricate and are mechanically robust [28, 29]. Our idea is to design a functional membrane as an ionic sieve with MOF and GO materials (abbreviated as MOF@GO). Their cooperative combination, where porous crystalline nanoparticles of MOF form building blocks while the mechanically flexible and robust GO laminates compose the structural spokes, may provide a promising construction strategy for the ionic sieve membranes.

Here, we report a MOF-based ionic sieve designed specifically for the lithium-sulfur battery, functioning as a battery separator to selectively sieve  $\text{Li}^+$  ions while blocking polysulfides [21, 30, 31]. We chose  $\text{Cu}_3(\text{BTC})_2$  (HKUST-1) as the MOF to construct the MOF@GO separator because its 3-D channel structure contains highly ordered micropores with a size window of approximately 9 Å [25, 32], which is reasonably smaller than the diameters of lithium polysulfide ( $\text{Li}_2\text{S}_n$ ,  $4 < n \leq 8$ ) [33, 34]; thus, it is well suited for blocking polysulfides. The MOF@GO separator

demonstrated high efficiency in blocking polysulfides and remarkable stability over long-term cycling in a lithium-sulfur battery without complicated synthesis or chemical surface modification of cathode materials. The battery possesses low capacity fading rates of approximately 0.019% per cycle over 1,500 cycles.

## 3.2 Experiment and Characterization

### 3.2.1 Chemicals

All chemicals, including 1,3,5-benzenetricarboxylic acid (BTC) (99.5%),  $\text{Cu}(\text{NO}_3)_2 \cdot 3\text{H}_2\text{O}$  (99.5%), N,N-dimethylformamide (DMF) (99.8%), ethanol (99.8%), 1,3-dioxacyclopentane (DOL 99.8%), 1,2-dimethoxyethane (DME 99.8%), and LiTFSI (lithium bis(trifluoromethanesulfonyl)imide 99.9%) were commercially purchased from TCI Chemicals without further purification. Graphene oxide (GO) was prepared from natural graphite powder (> 99.8%, Alfa Aesar) *via* a modified version of Hummers' method. The filter membrane (47 mm, 0.2  $\mu\text{m}$ ) and Millipore filter systems were obtained from Millipore Co. Ltd.

### 3.2.2 The Fabrication of coin cells and CV measurement in lithium-sulfur batteries

The CMK-3/S composite was prepared as previously reported <sup>[6]</sup>. To prepare the cathode materials, the various CMK-3/S composites were mixed with carbon black (Super P) and poly(vinylidene fluoride) binder (80:10:10 by weight) in N-methyl-2-pyrrolidinone. The slurry was coated on the current collector and dried under vacuum to form the working cathode. Lithium metal foil was used as the counter electrode. Common 2032-type coin batteries were assembled in an argon-filled glove box. The electrolyte contained 1 M LiTFSI and 0.1 M  $\text{LiNO}_3$  in 1:1 (v/v) 1,2-dimethoxyethane (DME) and 1,3-dioxacyclopentane (DOL). Before use, the MOF@GO and GO separators were cut into 16 mm pieces and then washed with blank electrolytes in the glove box. According to thermogravimetric analysis (TGA)

measurements, the sulfur content of the CMK-3/S composite was approximately 70 wt%, accounting for approximately 56 wt% of the electrode mixture, with a typical sulfur mass loading of 0.6-0.8 mg cm<sup>-2</sup>. Galvanostatic cycling was conducted on a Hokuto charging/discharging machine, and the cutoff potential was in the range of 1.5-3.0 V (versus Li<sup>+</sup>/Li).

Cyclic voltammetry (CV) is one kind of electrochemical measurement by potentiodynamic scan. The potential of sulfur cathode (Lithium-sulfur batteries) is scanned linearly versus time. In the CVs, the extended cutoff voltage has been measured between 1.5 and 3.4 V. The set potential will return to the initially potential after CV scanning in lithium-sulfur batteries. In experimental, CV measurements have been conducted by Solatron electrical station. The CV curve in lithium sulfur battery with a MOF@GO separator is at a scan rate of 0.1 mV s<sup>-1</sup>. The lithium-ion diffusion rate has also been measured by different scanning rates, ranging from 0.1 mV s<sup>-1</sup> to 0.2 mV s<sup>-1</sup>.

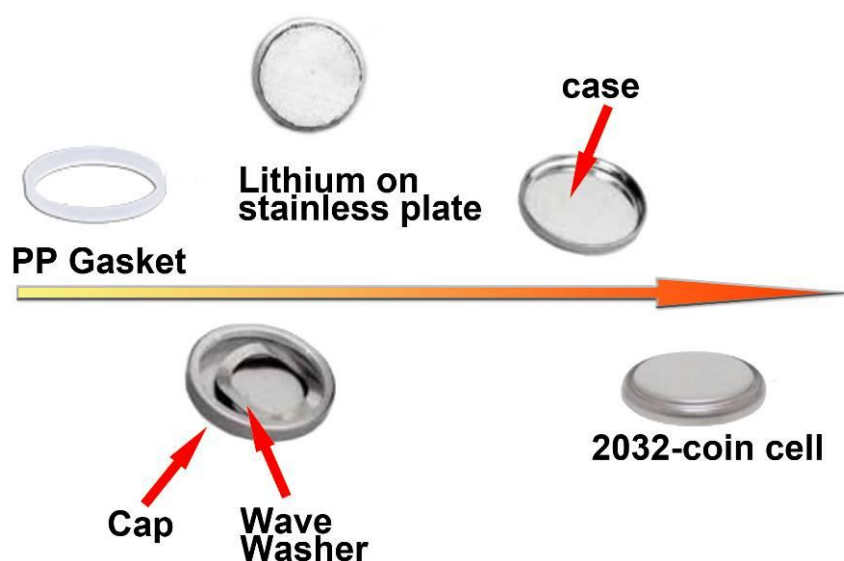


Fig. 3.1. The fabrication of 2032-coin cell in lithium-sulfur batteries.

### 3.2.3 Characterization of the MOF@GO separator

PXRD data were collected at ambient temperature on a Bruker D8 Advanced

diffractometer at 40 kV, 40 mA for Cu-K $\alpha$  ( $\lambda=1.5418 \text{ \AA}$ ). AFM measurements were obtained on a Nano-WizardII Bio AFM under the tapping mode. Samples were prepared by dripping an aqueous suspension on the silicon chip. The scanning rate and the resonance vibration frequency were 1 Hz and 310-330 kHz, respectively. SEM studies were conducted on a JSM6700-F field emission scanning electron microscope. Thermal analysis was performed on a NETZSCH STA 449C instrument from room temperature to 800 °C with a heating rate of 2 °C/min under nitrogen flow. The nitrogen adsorption was measured with a Hiden IGA100B analyser at 77 K and 1 atm. The infrared spectra with KBr pellets were recorded in the range of 4000-400  $\text{cm}^{-1}$  on a Bruker VERTEX70 FT-IR spectrometer. Solid UV/Vis spectra were obtained using a PE Lambda 900 UV/Vis/NIR spectroscope equipped with an integrating sphere and using the BaSO<sub>4</sub> plate as the reference.

### 3.2.4 Fabrication of Cu(II)-MOF@GO separator

The MOF nanoparticles were synthesised according to the process in a previous report [28, 31]. The mixed solution containing copper(II) nitrate trihydrate (Cu(NO<sub>3</sub>)<sub>2</sub>·3H<sub>2</sub>O) (0.966 g, 4 mmol) and 1,3,5-benzenetricarboxylic acid (0.42 g, 2 mmol) was introduced to prepare the crystalline particles by the vacuum filtration. The fabrication process of the MOF@GO separator was shown (Fig. 3.1). A certain amount of precursor solution containing copper nitrate and 1,3,5-benzenetricarboxylic acid was prepared for the fabrication. Crystalline nanoparticles were synthesised and self-assembled on the filter membrane. The GO solution was diluted by sonication to 0.1 mg/ml. GO laminates in SEM images and atomic force microscope (AFM) images were confirmed. GO separators were manufactured by filtration in the absence of MOF nanoparticles. After filtration, these peeled-off separators were kept under adequate dehydration before use.

The 3-D structure of HKUST-1 is constructed by the binuclear Cu(II) paddlewheel subunits and carboxylate linkers. Such a structure can retain high stability and robustness under extreme conditions. These highly ordered micropores

(approximately 9 Å) are reasonably smaller than the diameters of lithium polysulfide ( $\text{Li}_2\text{S}_n$ ,  $4 < n \leq 8$ ) [32-34].

The fabrication procedure is shown. The initial MOF layer is grown *in situ* as reported [28, 31]. After filtering a certain amount of diluted GO solution, the parallel GO layer is regularly formed on top of the uniform crystalline MOF nanoparticles. The adjacent MOF and GO layers are tightly adhered on the filter membrane. Next, this process is repeated twice or thrice for a better fabrication. These continuously growing MOF nanoparticles fill the previous void space without an obvious gap along the grain boundary. After peeling off from the filter, a free-standing separator was obtained.

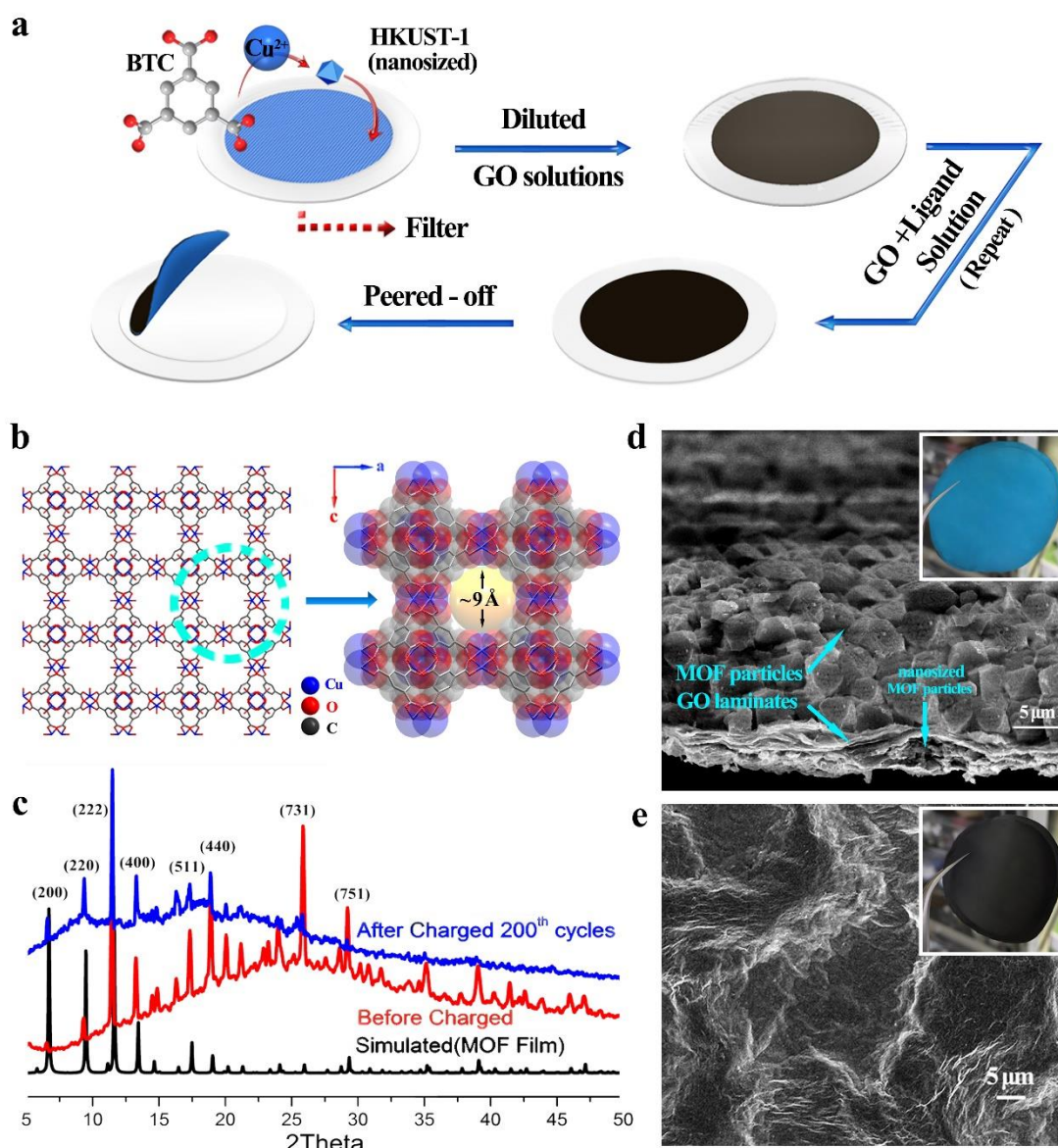


Fig. 3.2. Fabrication and Structural characteristics of MOF@GO separators. (a) Schematic of the fabrication process of MOF@GO separators. The MOF nanoparticles and introduced GO laminates synergistically consist of a MOF@GO separator. (b) An illustration of the microporous crystalline structures (HKUST-1). The homogeneous coordinated structures are depicted by sticks, whereas the pores are highlighted in space-filling representation. (c) The PXRD patterns of MOF@GO separators. The MOF structural skeleton remains intact during the discharge/charge process over 200 cycles. (d) The SEM image of the multilayered MOF@GO separator. The inset shows a digital photo along the MOF side. (e) The SEM image of the GO layer. The inset shows a digital photo along the GO side. Scale bar: 5  $\mu\text{m}$ .

Powder X-ray diffraction (PXRD) patterns indicate that these MOF particles in the separator are in agreement with that of HKUST-1 along the oriented (001) directions. On the basis of the crystalline growth mechanism, the cuboctahedron was found to occupy the dominant morphology. The structural skeleton of MOF remained intact throughout the discharge/charge process over 200 cycles. The multilayered structure of the MOF@GO separator is shown in the corresponding scanning electron microscopy (SEM) image. The nitrogen adsorption isotherm was measured at 77 K and 1 atm. The pore size distribution of our MOF@GO separator (approximately 9  $\text{\AA}$ ) is calculated according to the non-local density functional theory (NLDFT) model, indicating its microporous nature. The synergistic effects of the MOF particles and GO laminates further help reinforce the stability of the separator.

### 3.2.5 Permeation experiments

Permeation experiments were performed using a homemade V-shaped device, as shown in Fig. 3.2. The device consists of two glass tubes and MOF@GO separators or GO separators. The separator was implemented by a transparent instant adhesive with a 20-mm aperture. An additional coat of instant adhesive was required before connecting the two glass tubes. In a typical experiment, small amounts of

polysulphide solutions (0.1 M  $\text{Li}_2\text{S}_6$  in a blank electrolyte) were injected on the left side. The blank electrolyte was kept at the same level as on the right side. Before the experimental measurements, the MOF@GO or GO separators were carefully and thoroughly checked and for possible cracks or holes.

As a separator in a lithium-sulfur battery, the permeation resistance of the MOF@GO separator towards soluble polysulfides is an important factor. The permeation experiments were conducted in homemade V-shaped devices. The polysulfide solution (0.1 M  $\text{Li}_2\text{S}_6$ ) was slowly added into the left tube. Next, the blank electrolyte was slightly injected into the right counterpart. The permeation device with the GO separator was measured under similar conditions.

In the permeation experiment with a MOF@GO separator, polysulfides were unable to pass through the separator within 48 hours. As an ionic sieve, the MOF@GO separator demonstrates obvious blocking effects towards polysulfides. In comparison, the permeation experiment revealed that the GO separator was unable to sufficiently block the soluble polysulfides over time. Initially, a slight amount of polysulfide was found to permeate through the separator within 1 hour. However, the GO separator malfunctioned in the next stage. Almost 1/8 of the right counterpart was occupied by a vivid scarlet polysulfide solution within 3 hours. Polysulfides underwent accelerated permeation through the separator and entered into the right-hand tubes. Finally, vivid scarlet polysulfides continued diffusing through the separator and fulfilled the blank electrolytes within 12 hours.

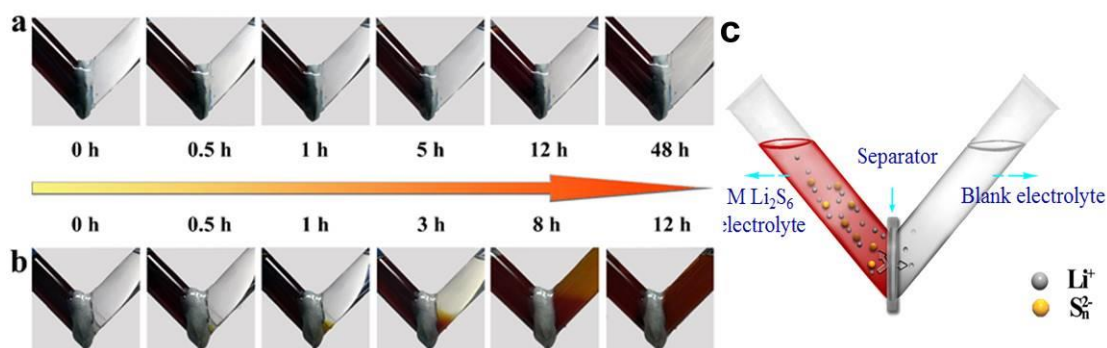


Fig. 3.3. Polysulfide permeation measurements. (a) V-type permeation device with a MOF@GO separator. The MOF@GO separator retained its resistance towards

polysulfides over 48 hours. No obvious polysulfide permeation through the MOF@GO separator was observed. (b) The V-type permeation device with a GO separator. The polysulfides gradually permeate through the GO separator over time and fulfil the blank electrolyte over 12 hours; (c) The permeation mode with the separators.

### 3.3 Results and Discussion

#### 3.3.1 Porosity of MOF@GO separator

The permanent porosity of our self-assembled MOF@GO separators was studied using gas permeation experiments. On the basis of its microporous properties, it is supposed to function as the effective ionic sieve with its highly narrowed pore sizes. In our case, the pore diameter is around 9 Å, which is estimated through the separation capability of its structures.

For the sake of the gas adsorption, the nitrogen adsorption isotherm has been measured at 77 K and 1 atm. It is noteworthy that the pore size distributions of our MOF based separator can be precisely measured and calculated due to its adsorption behaviour (Fig. 3.3). Nitrogen adsorption with a typical reversible type I isotherm was performed 514.7 m<sup>2</sup> g<sup>-1</sup> (Langmuir surface area) and analyzed the pore size distribution. The Brunauer–Emmett–Teller (BET surface area) with a saturated adsorption amount of 368.2 m<sup>2</sup> g<sup>-1</sup> is consistent with theoretical calculation.

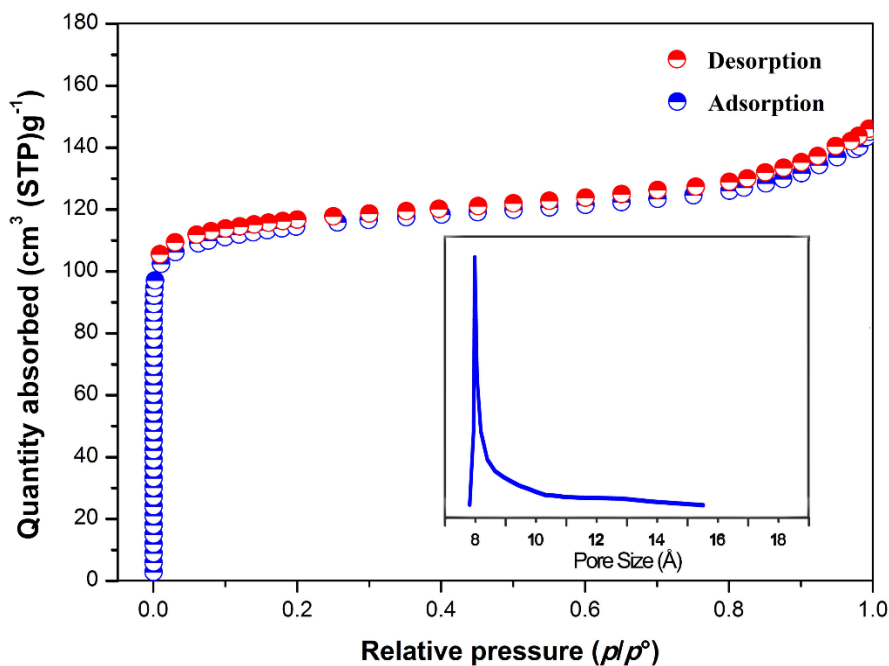


Fig. 3.4. Nitrogen sorption data for MOF@GO separators. N<sub>2</sub> sorption isotherm at 77 K and its analytical pore size distribution.

Accordingly, it can be regarded that by the non-local density functional theory (NLDFT) model, pore size distribution in our separators can be confirmed as a narrow arrangement below 9 Å. In addition, compared with the adsorption, the nitrogen desorption amount has illustrated no obvious loss in the adsorption-desorption test, suggestive of the stable and reliable MOF skeleton in our separator.

Therefore, the BET analysis has indicated its restricted pore sizes in our separators as expected, and indicates the microporous nature of our self-assembled MOF@GO separators. Following our experimental design, its excellent restriction may introduce positive contribution to the electrochemical performance in lithium-sulfur batteries. One advantageous factor is these perfectly high-ordered micropores that can function as an efficient ion sieve with polysulfide resistance and minimize the shuttle effects of polysulfide dissolution. We have made one more analyses on the microporous and mesoporous distribution between 0 and 300 Å. As depicted, there is no more pore size distribution in the whole range.

In general, on the basis of the nitrogen adsorption, the Brunauer–Emmett–Teller

(BET theory) is widely applied to calculate the specific surface area. Meanwhile, the non-local density functional theory (NLDFT) is chosen to estimate the permanent porosity. In our case, the saturated adsorption amount of our self-assembled MOF@GO separators arrived at  $368.2 \text{ m}^2 \text{ g}^{-1}$ . The narrow pore size distribution is below  $9 \text{ \AA}$ . In fact, both of the two values is perfectly consistent with theoretical calculation. As mentioned above, it is unnecessary to concern the porosity in the MOF@GO separator.

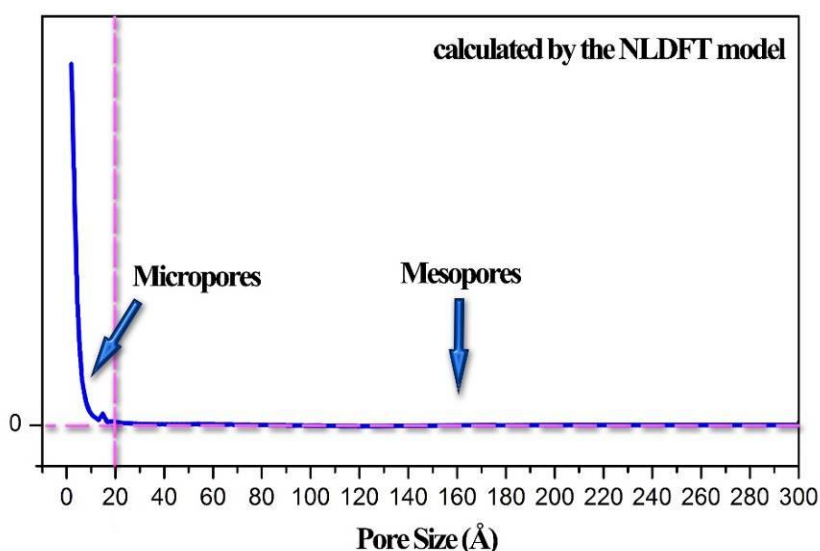


Fig. 3.5. Nitrogen sorption data for MOF@GO separators. N<sub>2</sub> sorption isotherm at 77 K and its analytical pore size distribution. Follow the calculation of the non-local density functional theory (NLDFT) model.

### 3.3.2 Electrochemical stability with/without MOF@GO separator

Experimentally, the extended cutoff voltage has been measured between 1.5 and 3.4 V in the lithium sulfur batteries (Fig. 3.5). The Cyclic voltammetry (CV) was measured over 5 cycles at different rates and the initial 5 cycles therein were measured at the scan rate of  $0.1 \text{ mVs}^{-1}$ . The cells with/without the MOF based separators have been introduced, individually. As depicted, the pair of sharp redox peaks indicates that during the electrochemical process, the sulfur witnessed the electrochemical reactions in cells.

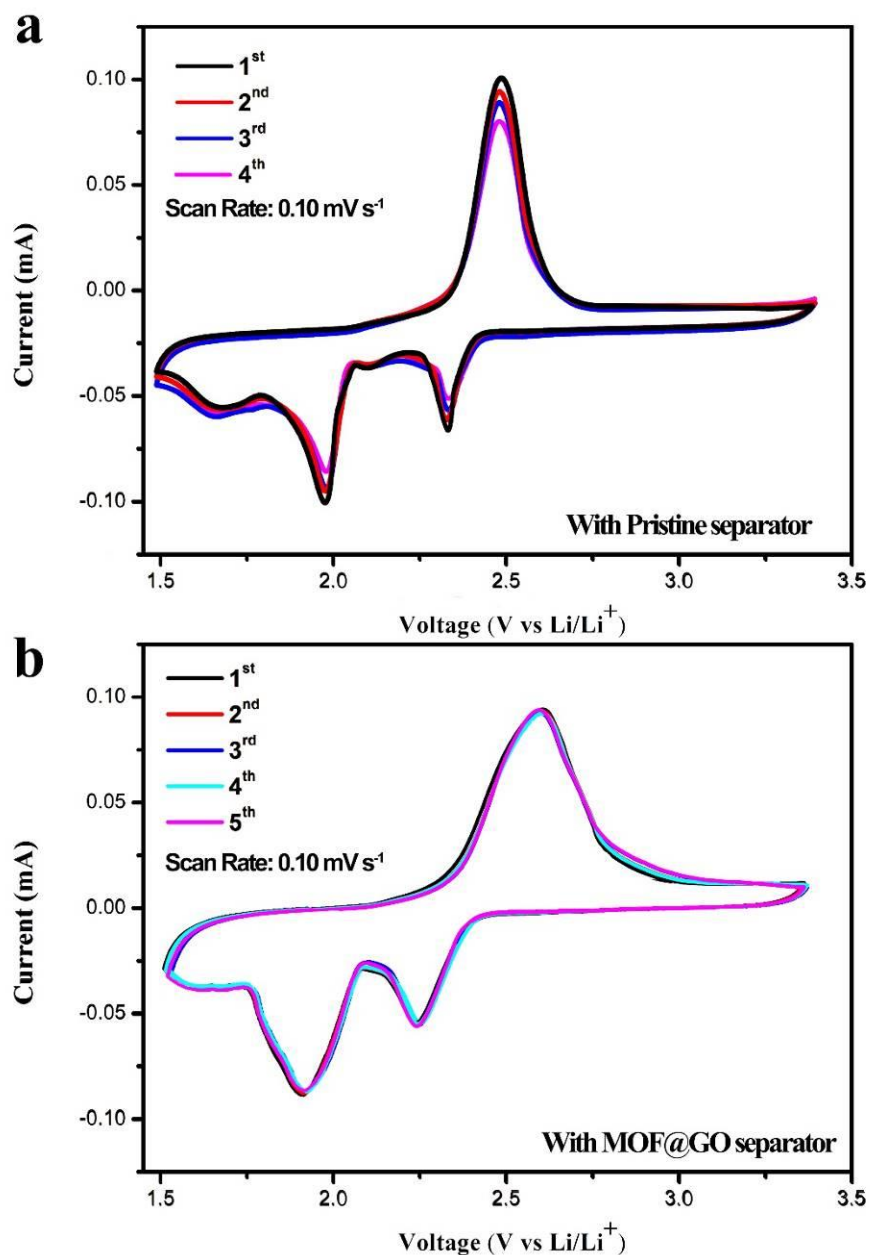


Fig. 3.6. (a) CV profiles with a pristine separator at a scan rate of  $0.1 \text{ mV s}^{-1}$ , (b) CV profiles with a MOF@GO separator at a scan rate of  $0.1 \text{ mV s}^{-1}$

Typically, the CVs of the lithium-sulfur battery at the scan rate of  $0.1 \text{ mV s}^{-1}$  without MOF@GO separators is introduced. The first cathodic peak at 2.4 V is attributed to the conversion of elemental sulfur ( $\text{S}_8$ ) to soluble lithium polysulfide ( $\text{Li}_2\text{S}_n$ ,  $4 < n \leq 8$ ). The second peak at 2.0 V is regarded to correspond to the formation of insoluble  $\text{Li}_2\text{S}_2$  and eventually  $\text{Li}_2\text{S}$ . A lower cathodic peak may be found at the end of the discharge

process, which can be regarded to the irreversible decomposed  $\text{LiNO}_3$  in the electrolyte. Conversely, there is only one strong anodic peak at  $\sim 2.5$  V, illustrating the backward reaction from  $\text{Li}_2\text{S}$  and  $\text{Li}_2\text{S}_2$  to  $\text{Li}_2\text{S}_4$  and continuous conversion of  $\text{Li}_2\text{S}_4$  to  $\text{Li}_2\text{S}_8/\text{Sulfur}$ .

In comparison, the other group of the lithium-sulfur battery with MOF@GO separator is also measured. The first cathodic peak at  $\sim 2.3$  V is ascribed as the reduction of elemental sulfur to lithium polysulfide ( $\text{Li}_2\text{S}_n$ ,  $4 < n \leq 8$ ). The second peak at 1.9 V is treated as the further reduction to  $\text{Li}_2\text{S}_2$  and eventually to  $\text{Li}_2\text{S}$ . Similarly, the corresponding anodic peak is illustrated as one strong and broad peaks as well. The peak illustrates a slight shift to  $\sim 2.6$  V, indicative of the sequential redox reactions from lithium polysulfide to elemental sulfur during the CV scans.

In our experiments, the electrolyte was prepared with 1 M LiTFSI and 0.1 M  $\text{LiNO}_3$  in 1:1 (v/v) 1,2-dimethoxyethane (DME) and 1,3-dioxacyclopentane (DOL). In the CVs, the extended cutoff voltage has been measured between 1.5 and 3.0 V in the lithium-sulfur batteries. The CV curve in lithium sulfur battery with a MOF@GO separator is at a scan rate of  $0.1 \text{ mV s}^{-1}$ .

As illustrated, in the extended voltage ranges, there observed no evident changes in peak intensities or locations in the CVs. It is seemed to illustrate excellent cycle stability and preferable consistency, indicative of high sulfur utilization in lithium sulfur batteries with the MOF-based separators. Hence, there is no doubt that never the possible parasitic reaction nor the partial decomposition of MOF compounds in electrochemical reactions would happen.

More notably, it is worth noting that there is only one strong oxidation peak existing in the CVs as mentioned. Due to the effects of polarization, this potential hysteresis is commonly observed in micropores-rich systems.

### 3.3.3 Electrochemical stability at different scanning rates

Generally, the MOF@GO separator can introduce no notable influence on the transfer of lithium ions across the separator, and play an important role in blocking the

dissolved polysulfide ions simultaneously. Therefore, to confirm that the MOF@GO separator afford highly selective capability to lithium ions against polysulfide anions, CVs with different scan rates are used to investigate  $\text{Li}^+$  diffusion coefficients according to the equation:

$$I_p = 2.69 \times 10^5 n^{3/2} S D^{1/2} \nu^{1/2} C$$

where  $n$  is the number of electrons per specific reaction, for  $\text{Li}^+$  it is 1;  $S$  is the surface area of the electrode which is  $1.53 \text{ cm}^2$  in this work;  $C$  is the concentration of  $\text{Li}^+$  ions in the material,  $I_p$  is the current intensity and  $\nu$  is the scan rate. And the diffusion coefficients could be calculated using the slop of fitting line  $I_p$  and  $\nu^{1/2}$ . Under the conditions with pristine separators (Celgard 2400 separators), the anodic peak was assigned at around 2.5 V and the cathodic peaks at around 2.0 and 2.3 V as peak  $\alpha_1$ ,  $\beta_1$ ,  $\gamma_1$ , respectively (Fig. 3.6). The values are evaluated to be  $D(\alpha_1)=1.45 \times 10^{-9} \text{ cm}^2/\text{s}$ ;  $D(\beta_1)=2.0 \times 10^{-9} \text{ cm}^2/\text{s}$ ;  $D(\gamma_1)=2.68 \times 10^{-9} \text{ cm}^2/\text{s}$ . In contrast, for the MOF-based separators, the corresponding redox peak was assigned as peak  $\alpha_2$ ,  $\beta_2$ ,  $\gamma_2$ , respectively. The diffusion coefficients were calculated to be  $D(\alpha_2)= 1.5 \times 10^{-9} \text{ cm}^2/\text{s}$ ,  $D(\beta_2)=1.9 \times 10^{-9} \text{ cm}^2/\text{s}$ ;  $D(\gamma_2)=2.1 \times 10^{-9} \text{ cm}^2/\text{s}$ . These similar values of  $D_{\text{Li}^+}$  indicated that the introduced MOF@GO separator would not significantly influence the diffusion of the lithium ion.

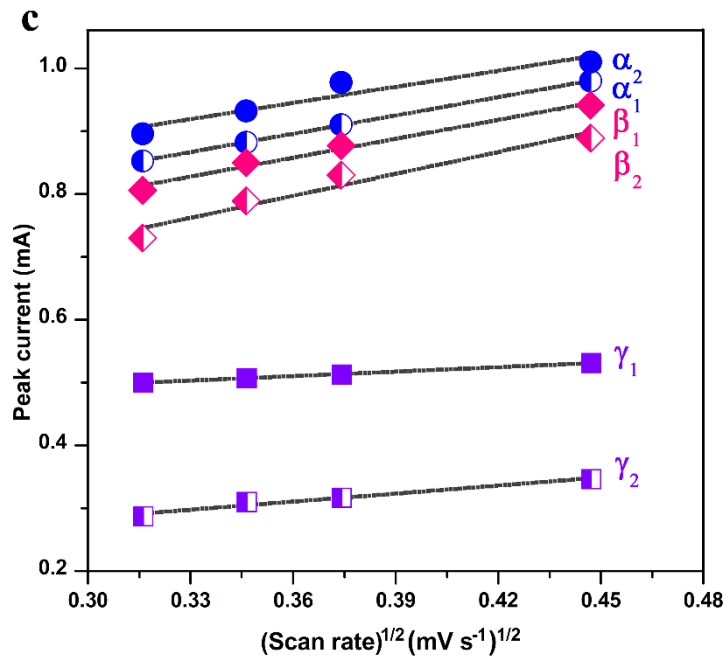
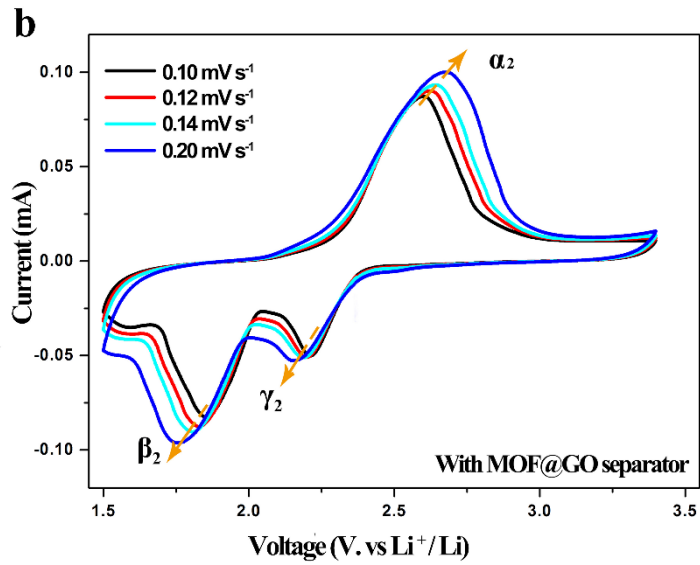
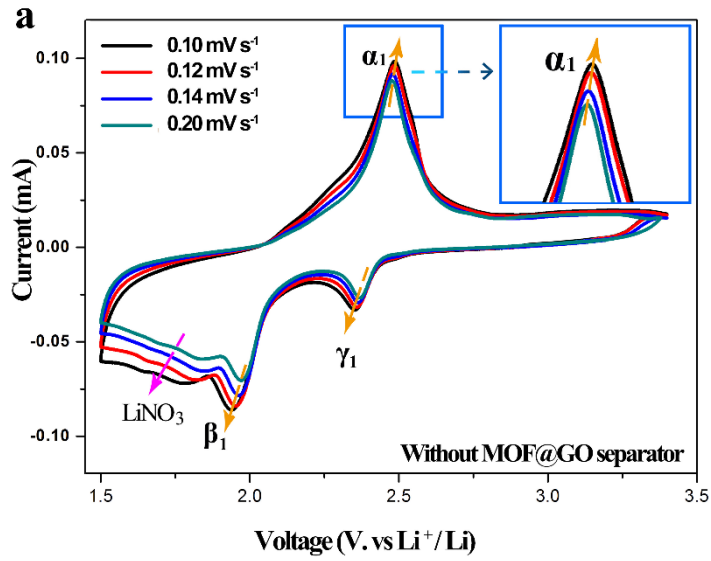


Fig. 3.7. CVs at different scan rates of lithium sulfur batteries. (a) With the pristine separators (Celgard) in lithium sulfur batteries. (b) With Cu(II)-based MOF@GO separators in lithium sulfur batteries. (c) The linear fits of the peak currents for the lithium sulfur batteries with/without MOF@GO separators.

As calculated, the cells with as-prepared MOF-based separators have illustrated equal levels of the ion conductivity, suggestive of its subtle influence on the lithium ion transition during the electrochemical process. The evaluated lithium-ion diffusion coefficient and ion conductivity still indicated a highly efficient lithium-ion transport with the MOF-based separator. In traditional, the shuttle effects of dissolved polysulfide ions would cause a poor rate performance and low cycle stability in conventional lithium-sulfur batteries. What remained to be illustrated is whether the severe polysulfide dissolution has been efficiently generated and controlled.

Therefore, despite the introduced MOF@GO separator may cause the slight increase of lithium-ion transfer resistance, it can still indicate the comparable capability of lithium-ion transport, highly efficient lithium-ion diffusion coefficient and ion conductivity, and the excellent rate performance with a MOF@GO separator in lithium sulfur batteries. As mentioned in the manuscript, we have further suggested that neither the conventional separator (Celgard) nor pure graphene oxide separator can effectively block the polysulfide diffusion. Their poor rate performance and low cycle stability can be ascribed as the shuttling effects of dissolved polysulfide ions in lithium sulfur batteries. Meanwhile, a series of researches have been carried out, as polymer coating, coupling with reversible polysulfide dissolution into the electrolyte over time, especially at high rates and long-term cycling.

In our experiments, the cells with excellent high-rate performance can be further understood through the nature of our MOF@GO separators. These perfectly high-ordered micropores ( $\sim 9 \text{ \AA}$ ) are rationally smaller than the diameters of lithium polysulfide ( $\text{Li}_2\text{S}_n$ ,  $4 < n \leq 8$ ), which would approximately bring in little negative effects on the transportation of lithium ion. Consequently, the MOF-based separator is able to serve as a preferable ionic sieving towards dissolved polysulfide, coupling with

comparable capability of lithium-ion transport and ion conductivity simultaneously. More notably, considering the analogous lithium ion conductivity of the MOF@GO separator, this will satisfy the multi-purpose demand for effectively separating polysulfide ions, as the ionic radiuses are significantly larger, allowing for its enhanced rate capability and long life performance in lithium-sulfur batteries.

The impressive rate performance is attributed to the effectively prevention its severely continuous diffusion of polysulfide dissolution, further favorably restrict its active mass shuttling loss on anodic metallic lithium and provide much higher sulfur utilization in lithium-sulfur batteries. Undoubtedly, it perfectly illustrated its great potential as an ionic sieve with excellent rate performance in electrochemistry. More importantly, our novel design approach to MOF-based separator technology targeting not only enhanced capacity but also rate performance and long-term cycle life is an entertaining attempt toward its potentially practical application in lithium-sulfur batteries. Its greatly enhanced electrochemical performance is achieved, even without complicated synthesis or surface modification of cathode materials, which is especially important in industrial production.

### 3.3.4 Ion conductivity of MOF@GO separator

To better understand the ion transition in the membranes, the ion conductivity is also calculated. Actually, the permeating capability of MOF@GO separators for lithium ions is also beneficial to know its performance of enhanced rate capability. As usual, the introduced MOF@GO separators would cause the slight increase of lithium-ion transfer resistance. In our experiments, cells were prepared by inserting pristine Celgard 2400 separators or the MOF@GO separators (Fig. 3.7) between two blocking stainless steel electrodes with the electrolyte. The working temperature was raised from ambient temperature (30 °C) to 65 °C and all cells were recorded at constant temperatures. Ionic conductivity measurements were performed by electrical impedance spectroscopy (EIS).

According the equation:

$$\sigma = L \times S^{-1} \times R^{-1}$$

where  $\sigma$  is the ion conductivity,  $L$  is the distance between the two stainless steel electrode, the  $S$  is the geometric area of electrode/electrolyte interface and the  $R$  is the intercept at the real axis in the impedance Nyquist plot.

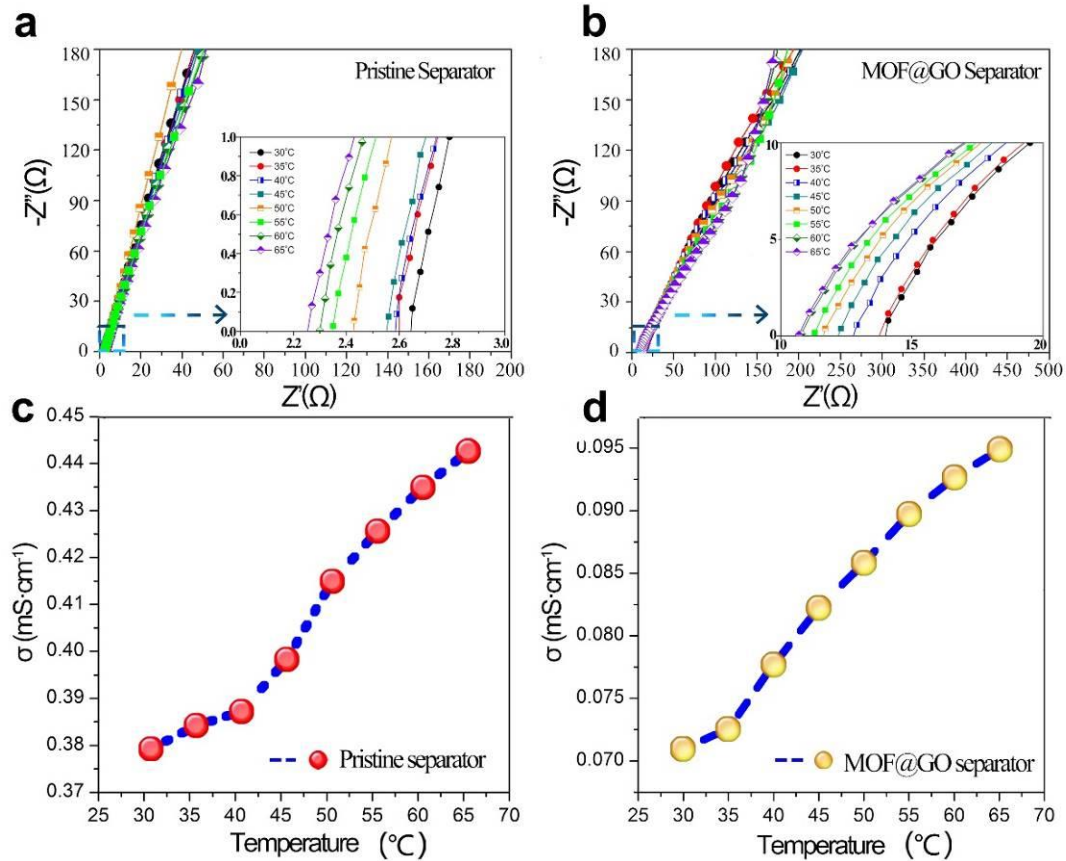


Fig. 3.8. Electrical impedance spectra of (a) Celgard (b) MOF@GO separator. Ion conductivity of (c) Celgard (d) MOF@GO separator.

The chosen ether-based electrolyte in battery is 1 M lithium bis(trifluoromethanesulfonyl)imide (LiTFSI) dissolved in a mixture of 1,3-dioxolane (DOL) and dimethoxyethane (DME). Following the previous experiments, the lithium-ion ionic conductivity of the electrolyte alone was also calculated to be 7.8 mS cm<sup>-1</sup> at ambient temperature (30 °C), which was similar to a series of researches reported.

Actually, due to the separator between two stainless steel electrodes with the electrolyte, it would greatly raise the interfacial resistance and further decrease the

lithium-ion conductivity of electrolyte. In our case, the calculated conductivity with MOF@GO separator is similar to that of Celgard in cells. The lithium-ion conductivity of electrolyte falls to 0.38 mS cm<sup>-1</sup> (Celgard) and 0.07 mS cm<sup>-1</sup> (MOF@GO), individually.

In comparison, the MOF@GO separator may cause the slight increase of lithium-ion transfer resistance than that of the Celgard separator. However, the lithium-ion conductivity with the MOF@GO separator still falls in a rational range. The introduced influence on the transfer of lithium ions can be ascribed to be negligible, especially considering its excellent performance in suppressing the dissolved polysulfide ions through the separator.

### 3.3.5 Stability of MOF@GO separator

To further investigate the roles that these MOF (HKUST-1) particles have played in the electrochemical process, the Infrared spectra (IR) and solid Ultraviolet–Visible spectra (UV-Vis) have been introduced. All of these MOF samples were collected from the self-assembled MOF@GO separators in the glove box, individually.

According to these well matched peaks, the IR spectra are supposed to integrally preserve the molecular potential energy surfaces, in the presence with the associated vibrant coupling<sup>5,6</sup>. The first to be introduced is the dehydrated MOF precursor. Its IR spectrum was plotted in the range of 400-3500 wavenumber region, which was found to agree with the previous values reported (Fig. 3.8). There exists a strong and broad peak at around 3400 cm<sup>-1</sup>, corresponding to the O-H groups with associated hydrogen bonds. The characteristic band, a strong C=O band at 1645 cm<sup>-1</sup>, witnessed a red shift towards short wavenumbers, indicative of carboxylate groups acting as bidentate linkages with hydrogen bonds.

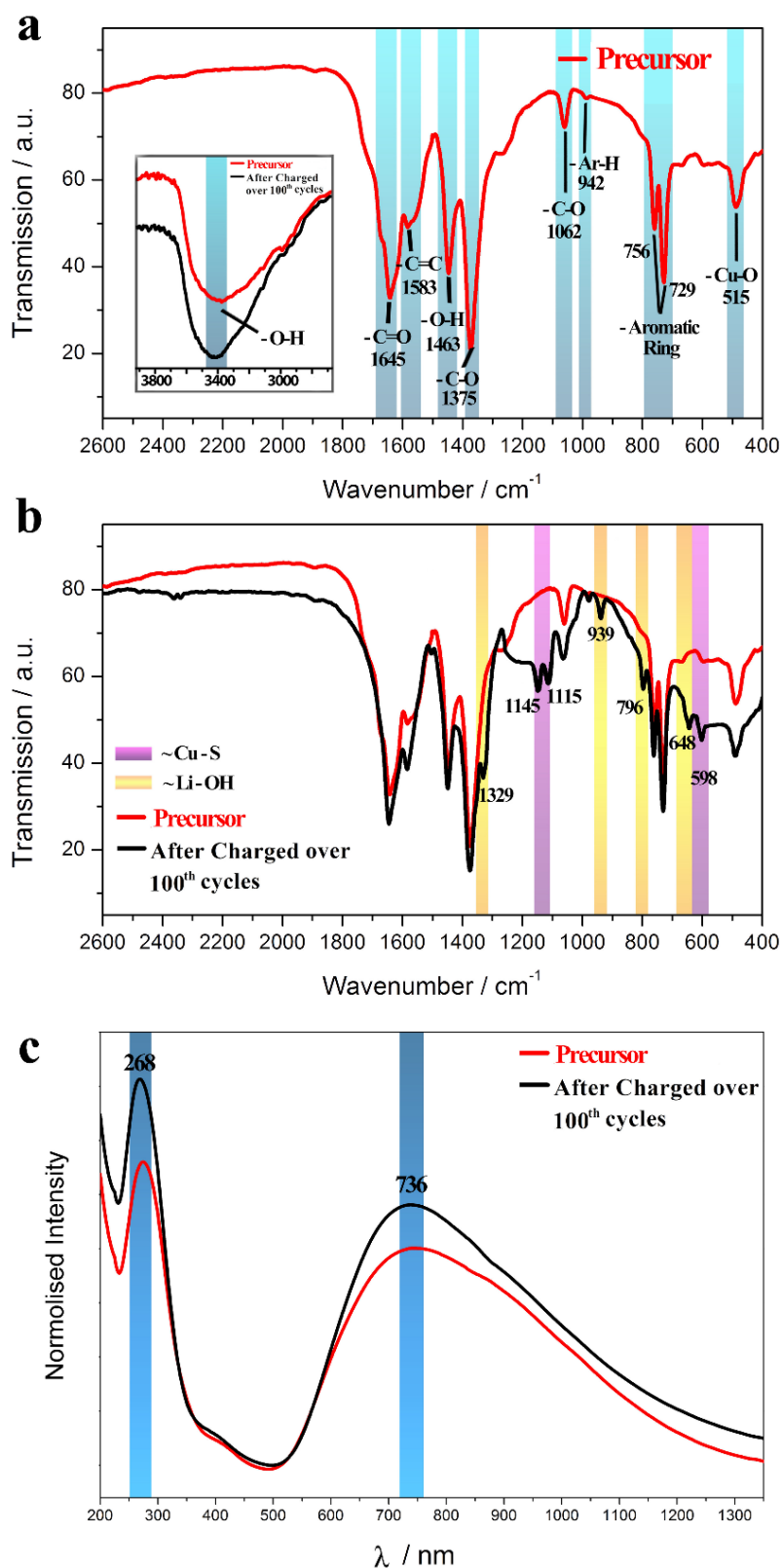


Fig. 3.9. The analyses based on the IR and solid UV-Vis spectra. (a) Before the electrochemical process, the IR spectra of the dehydrated MOF particles. (b) After the process over 100 charge/ discharge cycles, the IR spectra of the MOF particles have been measured. (c) The UV-Vis spectra of the MOF particles have illustrated no

obvious changes before/after the charge/discharge process over 100 cycles.

Moreover, the adsorptions at  $1463\text{ cm}^{-1}$  and  $942\text{ cm}^{-1}$  can be assigned to the O-H and C-H deformation vibrations respectively, while the peaks at  $1375\text{ cm}^{-1}$  and  $1062\text{ cm}^{-1}$  are also assigned to the C–O stretching vibration. It can be further illustrated that the bands at  $1645$  and  $1463\text{ cm}^{-1}$  correspond to the symmetric and asymmetric stretching vibrations of the carboxylate groups of 1,3,5-benzenetricarboxylic acid (abbreviated as BTC), respectively. In contrast, the weaker bands at  $1583$  and  $942\text{ cm}^{-1}$  are associated with C=C stretching modes of the aromatic ring. The moderate peaks between  $756$  and  $729\text{ cm}^{-1}$  have been detected and well recognized as out-of-plane bending of aromatic skeleton. In addition, a distinct peak at  $515\text{ cm}^{-1}$  emerging in the lower wavenumber range considerably corresponds to the Cu-O vibration as reported before.

In comparison, the IR spectra of these exhausted MOF particles that witnessed over 100 charge/discharge cycles have also been measured. As illustrated, their main adsorptions remain consistent with the well-associated values as before. Simultaneously, it is worth mentioning that we have found some extraneous bands that could be attributed to Li-OH and Cu-S interference in our observed spectra, respectively. Despite the peak in the higher wavenumbers for -OH is not highlighted for the strong hydroxyl band in carboxylic groups, the adsorptions in the next stretching region at  $1329\text{ cm}^{-1}$  and  $939\text{ cm}^{-1}$  have indicated obviously for the bending vibration of -OH. Moreover, the weaker characteristic spectra at  $796\text{ cm}^{-1}$  and  $648\text{ cm}^{-1}$  has reflected the stretching vibrations of low-lying -OH group. All of the results serve to substantiate the slight presence of Li-OH band that may derive from the trace amount of residuals in MOF@GO separators after dehydration or tiny water existing in electrolytes (~50 p.p.m. water in the electrolyte).

Additionally, the weaker and distinct bands emerging at  $1145\text{ cm}^{-1}$ ,  $1115\text{ cm}^{-1}$  and  $598\text{ cm}^{-1}$  is found to be perfectly in agreement with standard spectra of the Cu-S band. However, these exceptional bands are further reasonably close to the values with much lower transmittance intensity. Due to the specific metal-organic coupling

mode, the formation of Cu-S bond is restricted within the subtly available open metal sites that derived from the absent water molecules. That has been explained its formation thoroughly in the analyses of the Lewis acid-base interaction.

The following solid Ultraviolet-visible (UV-Vis) spectra are also collected. According to the Bragg equation, any great change of the lattice parameters and/or the effective refractive index is able to induce a shift in the reflectance peak ( $\lambda$ ) of these MOF crystals. It was expected that the capture of guest molecules/ions and their interaction with the microporous framework of the MOF skeleton would probably cause a shift in their spectra. Compared with the MOF precursor and exhausted MOF particles over 100 cycles in cells, their UV-Vis absorption spectra exhibited the MOF peaks centered at  $\sim 268$  nm and  $\sim 736$  nm without obvious changes as expected.

Due to the structural stability and robustness, we found that these MOF particles under the electrochemical conditions generated no apparent red/blue shift or new absorption bands in their reflectance peaks. Moreover, it indicated that the interaction between the guest and MOF host, as Cu-S band, or the possible decomposition of the rigid MOF skeleton was too subtle to bring in evident responses.

In general, the hybrid nature of MOF represents a series of porous materials with high surface area and tunable porosity, consisting of metal ions and organic linkers. In the as-synthesized forms, these potential open metal sites around the divalent copper centers are occupied by excess coordinated oxygen groups from carboxylic acid and one dissociative water molecule. Experimentally, these existing water molecules occupying the cavities are easily removed at approximate temperature in vacuum, which is widely applied in the adsorption measurements. Moreover, the dehydration, likewise, appears to meet electrochemical requirements in lithium-sulfur batteries. In addition, according to the PXRD measurements, the structural skeleton in the self-assembly MOF@GO separators remains intact throughout the electrochemical process, as typical of pristine HKUST-1. The IR and UV-Vis measurements have also illustrated no obvious changes except for the observed weak Cu-S bond in the electrochemical process.

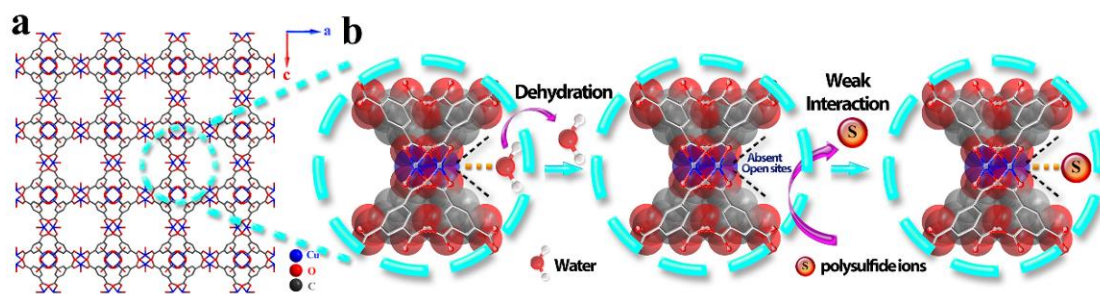


Fig.3.10. (a) The structural properties of binuclear Cu(II) paddlewheel subunits. (b) The presentation of the dehydration process (removing the water in cavities) and the weak interaction between the restricted open metal sites and polysulfide ions.

Based on the crystalline structure, it is favorably reasonable to understand the difference. The metal-organic skeleton was integrally constructed by the rigid Cu-O covalent bond. Because of stereochemical hindrance, the overwhelming portion of open metal sites on the surface have been generated and coordinated by the rich oxygen groups from carboxylic acid. Moreover, the removing water molecules have left the affordable but subtly limited vacancy for the formation of Cu-S bond in the porous frameworks (Fig. 3.9). Hence, the lack of available open metal sites has favorably hampered its success in generating the Cu-S bond.

As a matter of Lewis acid-base interaction, these well-defined copper centers are likely to partially release available open metal sites as Lewis acid characteristics. The interaction between the Cu(II) ions (Lewis acid) and the oxygen atom (Lewis base) of carboxylic groups, have played an important role in systematically generating and customizing the entire skeletons. The related calculation has also certificated that its bonding energy between metal dimers and water molecules is profoundly weaker. On the basis of the donor ability, polysulfide ions can be generally ascribed as soft Lewis base for the lone electron pairs. In comparison with the sulfur atoms, the oxygen atoms might be regarded as better electron donors, coupling with stronger Lewis basicity. Due to these excess rigid and strong covalent Cu-O bonds, it has been anticipated that the formation of Cu-S bond is likely to result in the disadvantageous energy barrier, which was found to agree with the experimental values as PXRD, IR

and UV spectra. Thereby, there merely exists in the form of ambiguous Cu-S bond bonds. The expected combining capacity of the polysulfide ions is significantly weakened and illustrates no severe influence in the available open sites or structural skeletons.

Therefore, based on the Lewis acid-base interaction and structural analyses, the formation of Cu-S bond has been generated within the restricted open metal sites and polysulfide ions, representing its negligible effects to the entire systems, rather than the strong trap or stabilization as the conventional MOF-based sulfur carriers.

Undoubtedly, the electrochemical performance could provide one insight into the inherent difference of these two microporous analogues. It may address whether the existing difference is the primary result. According to the calculation reported, the stability of the Cu(II)-based MOF appears to be a bit stronger than that of its Zn(II)-based analogues. More subtly, the concept of difference mainly depends on the changes in the geometric spheres of the coordinated metal atoms, which can introduce profound effects on the entire structural skeleton in coordination chemistry. In general, the calculation has illustrated that the interruption between the metal centers and water would increase the energy barrier after dehydration, rendering it instability in the inherent surface.

Simultaneously, the comparison in structural stability and energy barriers document the important role that the Lewis acid-base interaction might have played in. These Zn(II)/Cu(II) dimers are able to partially release available open metal sites as Lewis acid characteristics. In contrast, due to the donor ability of polysulfide ions, it can function as soft Lewis base for the lone electron pairs. It seems analytical and reasonable in contrast to the combination of energetic decrease and structural stabilization. What counts is the difference of Lewis acid-base interaction on the surface of transition metal oxide centers has influence the energy status of entire frameworks, in the presence of their electrochemical performance in lithium-sulfur batteries. For the dehydrated Zn(II)-based framework, it underwent a square planar coordination to a square pyramidal geometry change in structures with higher energy barrier.

Hence, despite their electrochemical performance is strikingly close, the inherent difference suggests that the lithium-sulfur batteries with Cu(II)-based MOF@GO separators can provide preferable performance in electrochemistry rather than that with Zn(II)-based separators.

### 3.3.6 Electrochemical performance

Initial activation cycles are necessary in lithium-sulfur batteries due to the large interfacial contact area between carbon carriers and sulfur. Because of the higher sulfur content and lower electron conductivity, the intimate interconnections among sulfur particles play a significant role in improving the ionic transportation ability inside the mesoporous carbon particles [35, 36]. In our case, the initial process of approximately 100 cycles can be ascribed to the activation cycles for a highly reversible and stable electrochemical status.

The battery with a MOF@GO separator was measured at  $C/2$  ( $1\text{ C} = 1,673\text{ mA g}^{-1}$ ) over 500 cycles (Fig. 3.10). The initial discharge capacity was measured to be  $1,126\text{ mAh g}^{-1}$ , followed by a moderate drop up to 100 cycles. Nevertheless, the capacity still approached  $813\text{ mAh g}^{-1}$ ,  $807\text{ mAh g}^{-1}$  and  $799\text{ mAh g}^{-1}$  at the end of the 100<sup>th</sup>, 300<sup>th</sup> and 500<sup>th</sup> cycles, respectively, exhibiting high capacity retention. The fading capacity was thoroughly restricted within  $14\text{ mAh g}^{-1}$  in the range of the 100<sup>th</sup> - 500<sup>th</sup> battery cycle. In addition, the galvanostatic charge/discharge voltage plateaus at  $C/2$  are consistent with the typical profiles of lithium-sulfur batteries, corresponding to the conversion between the soluble lithium polysulfide ( $\text{Li}_2\text{S}_n$ ,  $4 < n \leq 8$ ) at approximately 2.1 V and insoluble lithium polysulfide ( $\text{Li}_2\text{S}_2$  and  $\text{Li}_2\text{S}$ ) at approximately 1.8 V. The results are consistent with the cyclic voltammetry (CV) measurements.

The enhanced electrochemical performance of lithium-sulfur batteries was evaluated at 1 C with MOF@GO and GO separators. Although the battery with the GO separator could deliver a relatively large initial capacity of  $1,000\text{ mAh g}^{-1}$ , it

exhibited a rather dramatic capacity decay. The capacity had already decreased to 611 mAh g<sup>-1</sup>, 363 mAh g<sup>-1</sup>, 258 mAh g<sup>-1</sup> and 234 mAh g<sup>-1</sup> at the end of 100<sup>th</sup>, 400<sup>th</sup>, 800<sup>th</sup> and 1000<sup>th</sup> cycles, respectively. The capacity retention rate was only approximately 23%. This result can be explained by the short-term stability of the blocking effects of the GO separator, which can be ascribed to the evanescence of the structural robustness of GO. Such a result is also in accordance with that of the permeation experiments.

Alternatively, the battery with the MOF@GO separator displayed a relatively moderate decrease in capacity up to 100 cycles, namely from the initial 1,207 mAh g<sup>-1</sup> to 870 mAh g<sup>-1</sup> at the 100<sup>th</sup> cycle. The capacity drop at this stage is regarded as to the activation process of the battery. The cycling performance was rather stable from 100<sup>th</sup> cycle up to 1,500<sup>th</sup> cycles, and retained a capacity of 855 mAh g<sup>-1</sup>. The capacity retention rate approached approximately 71% with a fading rate as low as 0.019% per cycle over 1,500 cycles, suggesting higher efficiency and kinetics of the battery.

To better understand the redox behaviours during discharge/charge process, the lithium-sulfur batteries with GO and MOF@GO separators were measured at different C-rates. The battery with the GO separator suffered from dramatic capacity decay. At C/5, the initial capacity can reach up to 885 mAh g<sup>-1</sup>, decreasing to 718 mAh g<sup>-1</sup> at the end. By cycling at a wide range of C-rates, as C/2, 1 C, 2 C and 3 C, the capacities remained at 452 mAh g<sup>-1</sup>, 296 mAh g<sup>-1</sup>, 141 mAh g<sup>-1</sup> and 84 mAh g<sup>-1</sup>, respectively. When switching back to C/5, the capacity reversed to 580 mAh g<sup>-1</sup> in the end. In contrast, the battery with MOF@GO separators demonstrated much better performance. After the initial capacity of approximately 1,072 mAh g<sup>-1</sup> at C/5, the retention capacity arrived at 969 mAh g<sup>-1</sup>. When cycling at 0.5 C, 1 C, 2 C and 3 C, the capacities remained at 801 mAh g<sup>-1</sup>, 612 mAh g<sup>-1</sup>, 537 mAh g<sup>-1</sup> and 488 mAh g<sup>-1</sup>, respectively. Last, the capacity returned to 876 mAh g<sup>-1</sup> at C/5.

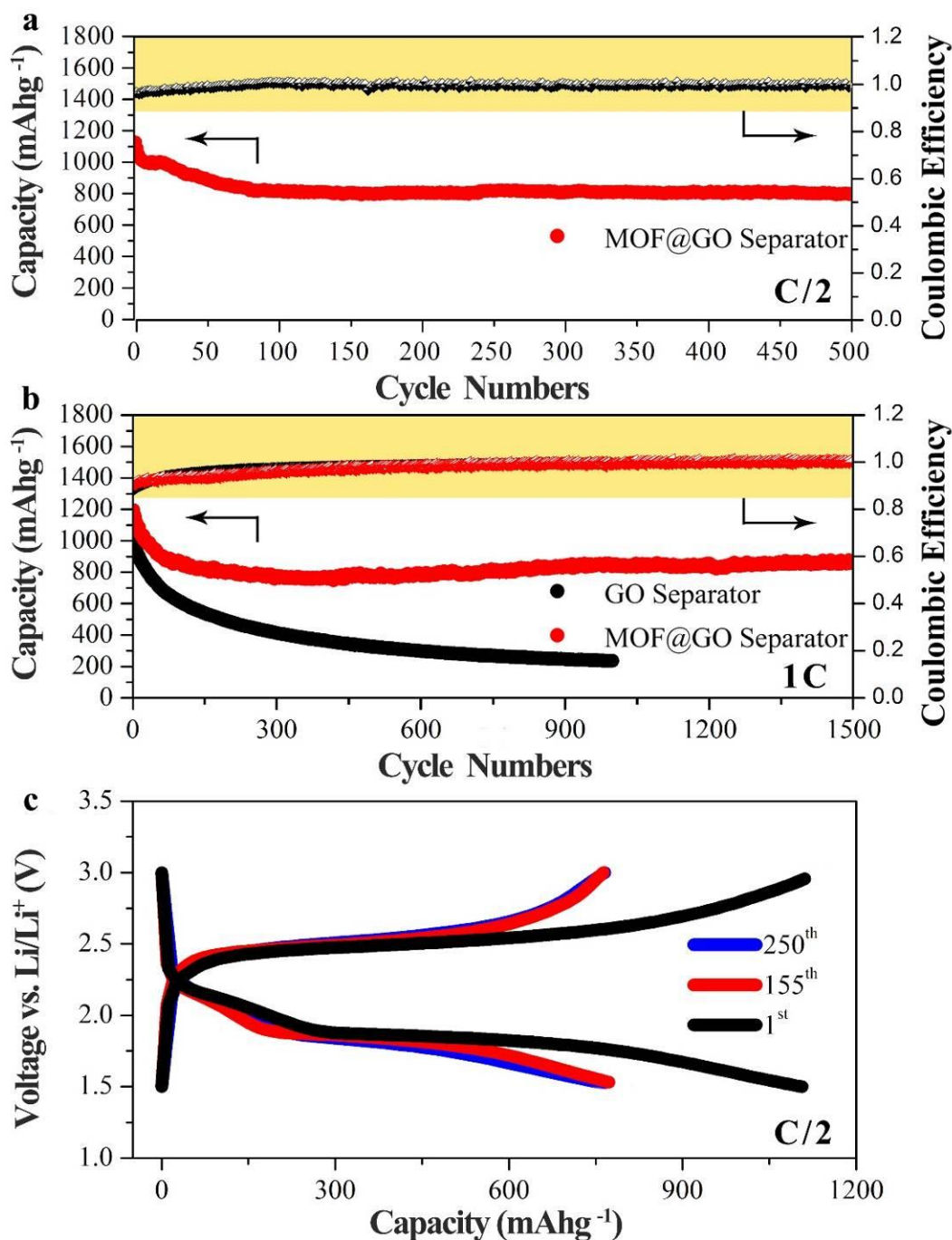


Fig. 3.11. Electrochemical performance of lithium-sulfur batteries. (a) Discharge capacity and coulombic efficiency at the rate of  $C/2$  over 500 cycles with MOF@GO separators. (b) Cycling performance at the rate of 1 C over 1,500 cycles with MOF@GO separators and over 1,000 cycles with GO separators. (c) Discharge/charge voltage profiles at the rate of  $C/2$  with MOF@GO separators. The specific capacities of the cathode are calculated based on the mass of sulfur.

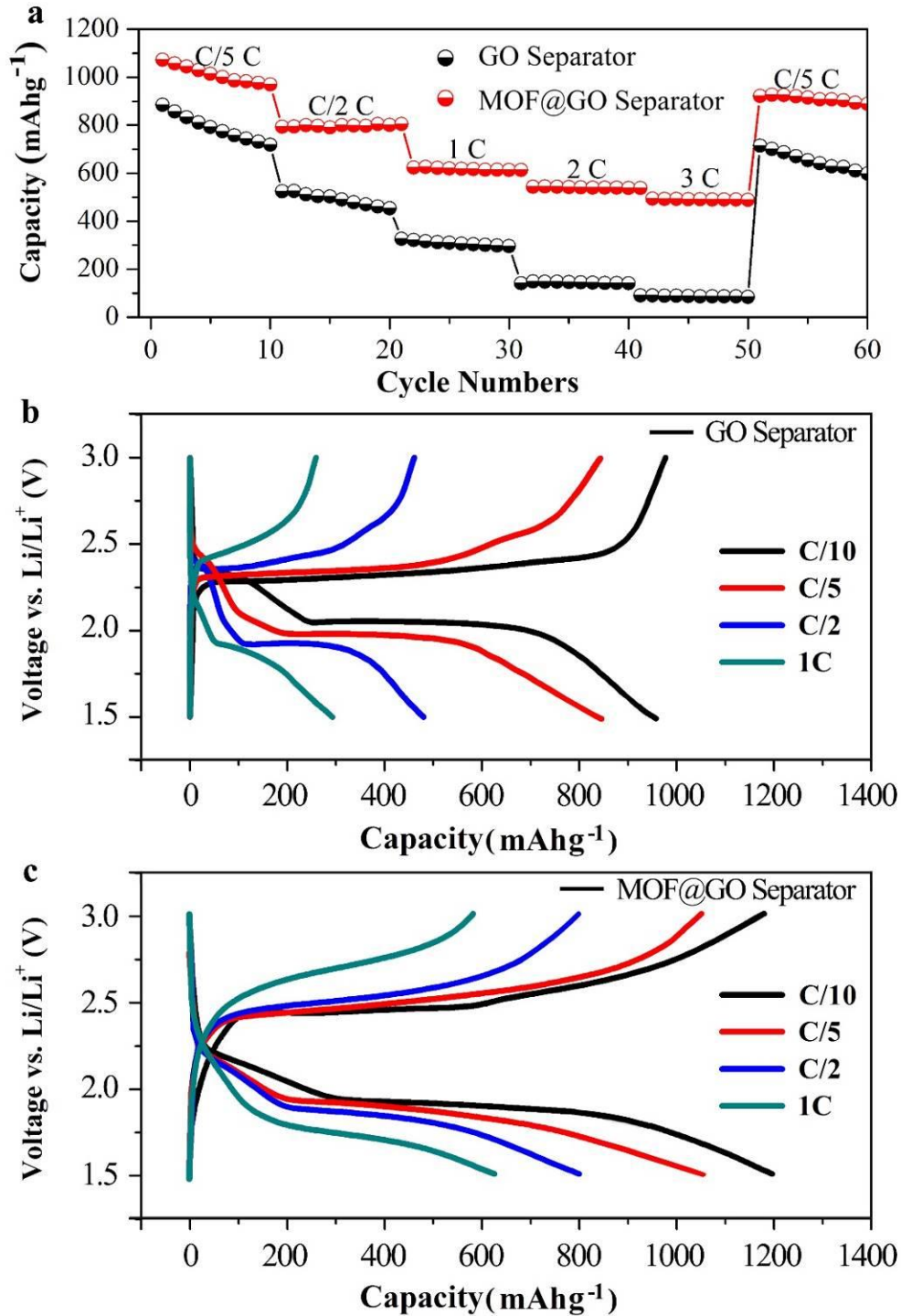


Fig. 3.12. Rate performance and voltage profiles of lithium-sulfur batteries. (a) Rate performance with MOF@GO and GO separators at various C-rates from C/5 to 3 C. The discharge/charge voltage profiles for batteries with (b) the MOF@GO separator and (c) the GO separator at different current densities.

Simultaneously, the discharge/charge voltage profiles at different C-rates for some selected cycles are shown (Fig. 3.11). All discharge curves of the batteries with GO and MOF@GO separators demonstrate two plateaus, which are typically observed in lithium-sulfur batteries with carbon/sulfur cathodes. In contrast, although the battery with the MOF@GO separator still illustrates the obvious two-plateau charging behaviour at lower rates of C/10 and C/5, the irregular charge profiles at higher C-rates are observed. To better understand the redox behaviors during discharge/charge process, the voltage profiles at different C-rates are illustrated in Fig. 3.11. The first cycle at a current rate of C/10 ( $1C = 1673 \text{ mA/g}$ ) was the initial activation cycle. The following cycles reached at C/5, C/2 and 1C, respectively.

Therein, at lower rates of C/10 and C/5, there still illustrates the obvious two-plateau behavior in the charging plots, though its charge plateau is not as flat as that with GO separator. With C-rates increased from C/10 C to 1C, both their voltage profiles keep well-matched shapes with the increased charge potentials and decreased discharge potentials. The sluggish  $\text{Li}^+$  diffusion kinetics with MOF@GO result in the gradually increased charge potentials and gradually decreased discharge potentials even at very low C-rates.

In addition, the charge plateau with the MOF@GO separator is not as obvious as that with the GO separator. The MOF modified separators illustrate excellent capability to block these dissolved polysulfide, coupling with the high polarization simultaneously. It is noteworthy that the introduced polarization in lithium-sulfur battery has resulted from the main difference among the charge curves at different rates, similar to a series of reports.

Note that the MOF-based separators illustrate high efficiency to block these soluble polysulfides while coupling with the high polarisation in batteries. Moreover, the main difference among the charge curves at different rates remains consistent with the previous CVs. With C-rates increased from C/10 C to 1 C, both their voltage profiles retain well-matched shapes with the increased charge potentials and decreased discharge potentials. A series of CVs with different scan rates are used to investigate  $\text{Li}^+$  diffusion coefficients, suggesting diffusion from the sulfur cathode side to the

anode side without obvious impediment [34, 37, 38].

The sluggish  $\text{Li}^+$  diffusion kinetics with MOF@GO result in the gradually increased charge potentials and gradually decreased discharge potentials, even at very low C-rates. In addition, according to the electrical impedance spectroscopy (EIS), the measured ionic conductivity has also illustrated that the MOF@GO separator introduces a negligible influence on the lithium ion transition across the separator, while preventing soluble polysulfides from migrating to the anode side. Hence, MOF-based separators have illustrated equal levels of the diffusion coefficient and ion conductivity under the electrochemical conditions.

### 3.3.7 Further characterization of the MOF@GO separators

According to the SEM measurements, the GO laminates were found to be detached from the GO separator after over 200 cycles. This observation is also in agreement with the permeation result with the GO separator. The diffusion of soluble polysulfides worsens the function of the GO separator because of widely existing void cracks among GO layers. According to previous calculations, every single S-S chain length estimated among the species of lithium polysulfide ( $\text{Li}_2\text{S}_n$ ,  $4 < n \leq 8$ ) ranged from 2.09 Å to 2.39 Å, and the lithium-sulfur bond length tended to be slightly less than 2.6 Å [33]. Moreover, these GO interlayers are unable to function as polysulfide molecules because the polysulfide diameters are less than their spacing distances ( $d \leq 13 \pm 1$  Å) [29, 39, 40]. The polysulfides can reasonably permeate through GO layers along these voids.

According to the PXRD patterns and SEM images, the GO laminates have negligible influence on the crystalline growth of MOF. Regarding the MOF@GO separator, its synergetic effects may primarily originate from the robust and highly ordered micropores, which have been identified by nitrogen adsorption. The MOF@GO separator primarily utilises the size effects as an ionic sieve in lithium-sulfur batteries to block these bigger polysulfides ( $\text{Li}_2\text{S}_n$ ,  $4 < n \leq 8$ ) from shuttling to the anode side [12, 19, 34] because the pore size is reasonably smaller than the diameters of polysulfides ( $\text{Li}_2\text{S}_n$ ,  $4 < n \leq 8$ ).

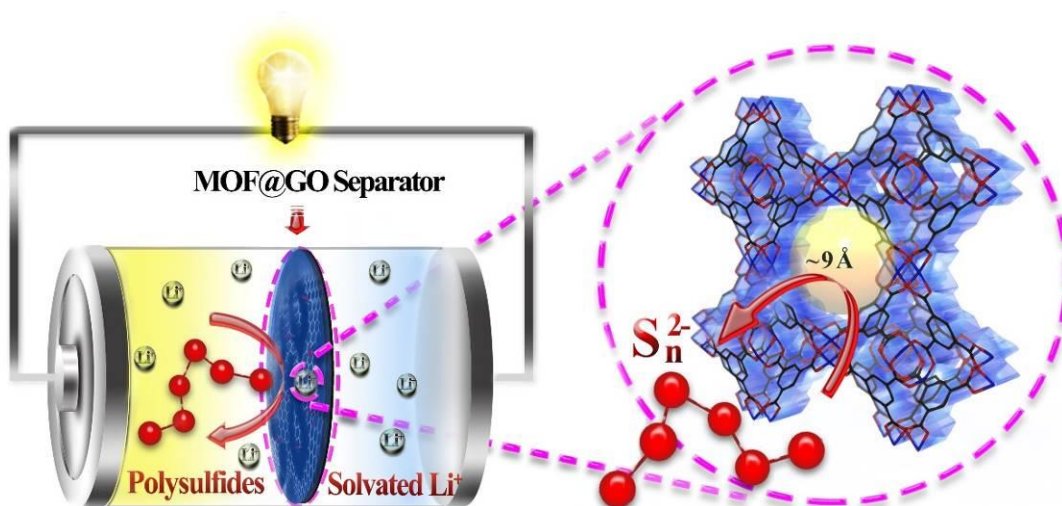


Fig. 3.13. Schematic of MOF@GO separators in lithium-sulfur batteries. The MOF@GO separator acts as an ionic sieve towards the soluble polysulfides. The enlarged image illustrates the MOF pore size (approximately 9 Å), which is reasonably smaller than that of polysulfides ( $\text{Li}_2\text{S}_n$ ,  $4 < n \leq 8$ ).

According to the mechanism of crystalline growth, these MOF particles are regularly grown *in situ* along the (001) direction in the fabrication process. The structural skeleton of self-assembled MOF@GO separators remains intact after up to 200 discharge/charge cycles. This further confirms the structural stability and reliability of MOF-based separators under rigid conditions.

In light of the aforementioned experiments, the roles the MOF has played in can be ascribed as the size effects, instead of the sulfur trap. The MOF@GO separator could perfectly act as one ionic sieve for its high-ordered porous frameworks and ionic selectivity toward the dissolved polysulfide ions in lithium-sulfur batteries.

Owing to the great hindrance along vertical and horizontal directions, the cuboctahedron should illustrate the superior domination along the crystal facets of {001} and {111}. Therein, in our MOF@GO separator, the crystalline growth is pointed toward the adjacent MOF particles along the horizontal direction of {111}. In contrast, its exposed crystalline facet of {001} was directed straightly to the vertical orientation. Following this self-assembly strategy, the MOF particles have witnessed

the highly regular arrangements inside the separator. As depicted, the potential channels can provide the larger window size of  $\sim 9$  Å. These highly ordered pores have been well regulated along the (001) direction, which is rationally smaller than the diameters of lithium polysulfide ( $\text{Li}_2\text{S}_n$ ,  $4 < n \leq 8$ ).

It would help understand the formation of Cu-S bond in stereochemistry. On the basis of the steric hindrance, the overwhelming vacancy of the Cu(II) sites were occupied by oxygen groups from carboxylic acid. In comparison, the only affordable vacancy for the formation of Cu-S bond is significantly limited, mainly provided by the removing water molecules existed in the porous cavity. It seems to be comparable in terms of its lower energy with the more stable structures <sup>[11, 12]</sup>. Simultaneously, in the light of weight ratio, its amount of sulfur trap is so subtle that the MOF based separator may embrace its stability in long-term cycles, instead of introducing any significantly disadvantage in lithium-sulfur battery.

In accordance with our initial targets, the MOF-based separator may embrace its stability in electrochemistry, instead of any of the significant disadvantages introduced in a lithium-sulfur battery. Their CVs, the infrared spectra and solid ultraviolet-visible (UV-Vis) light, are consistent with the well-associated values without side reactions <sup>[37, 41, 42]</sup>. After the 50 discharge/charge cycles, the detection of Cu-S bonds suggests that the formation of Cu-S bonds is irreversible. It is not surprising that the formed Cu-S bonds introduced negligible influence on the MOF structures and stability under electrochemical conditions. In light of steric hindrance, as the overwhelming vacancy of the Cu(II) sites are occupied by oxygen groups from carboxylic acid, the only affordable vacancy for the formation of Cu-S bond is significantly limited, which is mainly provided by the removal of water molecules existing in the porous cavities.

### 3.4 Conclusions

In summary, we designed and prepared a microporous MOF@GO separator for lithium-sulfur batteries. During the electrochemical process, the MOF@GO separator

plays the role of an efficient ionic sieve towards polysulfides migrating to the anode while introducing negligible influence on the transfer of  $\text{Li}^+$  ions across the separator. Moreover, the proposed separator may retain its structural stability and reliability under electrochemical conditions. The battery with the MOF-based separator exhibited sustainably enhanced cycling stability and a lower capacity-fading rate. The stable performance is mainly attributed to the size effects derived from the homogeneous porous frameworks of the separator. The strategy demonstrated here may guide us to develop functional separators with MOF-based materials for energy-storage devices.

### 3.5 References

1. Tarascon JM, Armand M. Issues and challenges facing rechargeable lithium batteries. *Nature* 414, 359-367 (2001).
2. Bruce PG, Freunberger SA, Hardwick LJ, Tarascon JM. Li-O<sub>2</sub> and Li-S batteries with high energy storage (vol 11, pg 19, 2012). *Nat Mater* 11,19-29 (2012).
3. Pang Q, Kundu D, Cuisinier M, Nazar LF. Surface-enhanced redox chemistry of polysulphides on a metallic and polar host for lithium-sulphur batteries. *Nat Commun* 5, 4759 (2014).
4. Yao HB, et al. Improving lithium-sulphur batteries through spatial control of sulphur species deposition on a hybrid electrode surface. *Nat Commun* 5, 3943 (2014).
5. Zhou GM, et al. A Graphene-Pure-Sulfur Sandwich Structure for Ultrafast, Long-Life Lithium-Sulfur Batteries. *Adv Mater* 26, 625-631 (2014).
6. Ji XL, Lee KT, Nazar LF. A highly ordered nanostructured carbon-sulphur cathode for lithium-sulphur batteries. *Nat Mater* 8, 500-506 (2009).
7. Zhou GM, Paek E, Hwang GS, Manthiram A. Long-life Li/polysulphide batteries with high sulphur loading enabled by lightweight three-dimensional nitrogen/sulphur-codoped graphene sponge. *Nat Commun* 6, 7760 (2015).
8. Yin LC, Wang JL, Lin FJ, Yang J, Nuli Y. Polyacrylonitrile/graphene composite as a precursor to a sulfur-based cathode material for high-rate rechargeable Li-S batteries. *Energ Environ Sci* 5, 6966-6972 (2012).
9. Chen SG, et al. Nanostructured Polyaniline-Decorated Pt/C@PANI Core-Shell Catalyst with Enhanced Durability and Activity. *J Am Chem Soc* 134, 13252-13255 (2012).
10. Seh ZW, et al. Two-dimensional layered transition metal disulphides for effective encapsulation of high-capacity lithium sulphide cathodes. *Nat Commun* 5, 5017 (2014).
11. Seh ZW, et al. Sulphur-TiO<sub>2</sub> yolk-shell nanoarchitecture with internal void space for long-cycle lithium-sulphur batteries. *Nat Commun* 4, 1331 (2013).

12. Liang X, Garsuch A, Nazar LF. Sulfur Cathodes Based on Conductive MXene Nanosheets for High-Performance Lithium-Sulfur Batteries. *Angew Chem Int Edit* 54, 3907-3911 (2015).
13. Demir-Cakan R, et al. Cathode Composites for Li-S Batteries via the Use of Oxygenated Porous Architectures. *J Am Chem Soc* 133, 16154-16160 (2011).
14. Zhou JW, et al. Rational design of a metal-organic framework host for sulfur storage in fast, long-cycle Li-S batteries. *Energ Environ Sci* 7, 2715-2724 (2014).
15. Zheng JM, et al. Lewis Acid-Base Interactions between Polysulfides and Metal Organic Framework in Lithium Sulfur Batteries. *Nano Lett* 14, 2345-2352 (2014).
16. Yin YX, Xin S, Guo YG, Wan LJ. Lithium-Sulfur Batteries: Electrochemistry, Materials, and Prospects. *Angew Chem Int Edit* 52, 13186-13200 (2013).
17. Park K, et al. Trapping lithium polysulfides of a Li-S battery by forming lithium bonds in a polymer matrix. *Energ Environ Sci* 8, 2389-2395 (2015).
18. Yao HB, et al. Improved lithium-sulfur batteries with a conductive coating on the separator to prevent the accumulation of inactive S-related species at the cathode-separator interface. *Energ Environ Sci* 7, 3381-3390 (2014).
19. Liang X, Hart C, Pang Q, Garsuch A, Weiss T, Nazar LF. A highly efficient polysulfide mediator for lithium-sulfur batteries. *Nat Commun* 6, 5682 (2015).
20. Peng HJ, et al. Janus Separator of Polypropylene-Supported Batteryular Graphene Framework for Sulfur Cathodes with High Utilization in Lithium-Sulfur Batteries. *Adv Sci* 3, 1500268 (2016).
21. Chung SH, Manthiram A. Bifunctional Separator with a Light-Weight Carbon-Coating for Dynamically and Statically Stable Lithium-Sulfur Batteries. *Adv Funct Mater* 24, 5299-5306 (2014).
22. Peng Y, et al. Metal-organic framework nanosheets as building blocks for molecular sieving membranes. *Science* 346, 1356-1359 (2014).
23. Wang B, Cote AP, Furukawa H, O'Keeffe M, Yaghi OM. Colossal cages in zeolitic imidazolate frameworks as selective carbon dioxide reservoirs. *Nature* 453, 207-211 (2008).
24. Bai SY, et al. Distinct anion sensing by a 2D self-assembled Cu(I)-based

metal-organic polymer with versatile visual colorimetric responses and efficient selective separations via anion exchange (vol 1, pg 2970, 2013). *J Mater Chem A* 1, 2970-2973 (2013).

25. Talin AA, et al. Tunable Electrical Conductivity in Metal-Organic Framework Thin-Film Devices. *Science* 343, 66-69 (2014).

26. Mao YY, et al. General incorporation of diverse components inside metal-organic framework thin films at room temperature. *Nat Commun* 5, 5532 (2014).

27. Huang JQ, Zhang Q, Peng HJ, Liu XY, Qian WZ, Wei F. Ionic shield for polysulfides towards highly-stable lithium-sulfur batteries. *Energ Environ Sci* 7, 347-353 (2014).

28. Dikin DA, et al. Preparation and characterization of graphene oxide paper. *Nature* 448, 457-460 (2007).

29. Joshi RK, et al. Precise and Ultrafast Molecular Sieving Through Graphene Oxide Membranes. *Science* 343, 752-754 (2014).

30. Su YS, Manthiram A. Lithium-sulphur batteries with a microporous carbon paper as a bifunctional interlayer. *Nat Commun* 3, 1166 (2012).

31. Huang JQ, Zhuang TZ, Zhang Q, Peng HJ, Chen CM, Wei F. Permselective Graphene Oxide Membrane for Highly Stable and Anti-Self-Discharge Lithium-Sulfur Batteries. *Acs Nano* 9, 3002-3011 (2015).

32. Chui SSY, Lo SMF, Charmant JPH, Orpen AG, Williams ID. A chemically functionalizable nanoporous material [Cu-3(TMA)(2)(H2O)(3)](n). *Science* 283, 1148-1150 (1999).

33. Vijayakumar M, et al. Molecular structure and stability of dissolved lithium polysulfide species. *Phys Chem Chem Phys* 16, 10923-10932 (2014).

34. Cuisinier M, et al. Sulfur Speciation in Li-S Batteries Determined by Operando X-ray Absorption Spectroscopy. *J Phys Chem Lett* 4, 3227-3232 (2013).

35. Chen SR, et al. Ordered mesoporous carbon/sulfur nanocomposite of high performances as cathode for lithium-sulfur battery. *Electrochim Acta* 56, 9549-9555 (2011).

36. Meini S, Elazari R, Rosenman A, Garsuch A, Aurbach D. The Use of Redox

Mediators for Enhancing Utilization of  $\text{Li}_2\text{S}$  Cathodes for Advanced Li-S Battery Systems. *J Phys Chem Lett* 5, 915-918 (2014).

37. Bouchet R, et al. Single-ion BAB triblock copolymers as highly efficient electrolytes for lithium-metal batteries. *Nat Mater* 12, 452-457 (2013).

38. Christie AM, Lilley SJ, Staunton E, Andreev YG, Bruce PG. Increasing the conductivity of crystalline polymer electrolytes. *Nature* 433, 50-53 (2005).

39. Lerf A, et al. Hydration behavior and dynamics of water molecules in graphite oxide. *J Phys Chem Solids* 67, 1106-1110 (2006).

40. Raidongia K, Huang J.X. Nanofluidic Ion Transport through Reconstructed Layered Materials. *J Am Chem Soc* 134, 16528-16531 (2012).

41. Scrosati B. Conducting polymers: Advanced materials for new design, rechargeable lithium batteries. *Polym Int* 47, 50-55 (1998).

42. Barpanda P, et al.  $\text{LiZnSO}_4\text{F}$  Made in an Ionic Liquid: A Ceramic Electrolyte Composite for Solid-State Lithium Batteries. *Angew Chem Int Edit* 50, 2526-2531 (2011).

43. Zhu K, Qiu HL, Zhang YQ, Zhang D, Chen G, Wei YJ. Synergetic Effects of  $\text{Al}^{3+}$  Doping and Graphene Modification on the Electrochemical Performance of  $\text{V}_2\text{O}_5$  Cathode Materials. *Chemsuschem* 8, 1017-1025 (2015).

## Chapter 4 Conclusions

In my PhD research, on the basis of synthesizing and characterizing the Cu(II)/Zn(II)-based MOF@GO separators, its favorable role the separator has played in has been thoroughly conducted.

The novel rechargeable lithium-sulfur batteries with lower cost and higher energy density become of current interest. Its higher theoretical specific capacity of 1,673 mAh g<sup>-1</sup>, has far exceeded that of current lithium-ion batteries. The natural abundance and lower competitive cost suggest that tremendous values in commercialization. However, the shuttle effects of polysulfide have resulted in rapid capacity fading and hindered its commercialization. We prepared a self-assembled Metal-Organic Frameworks based separator to solve this problem.

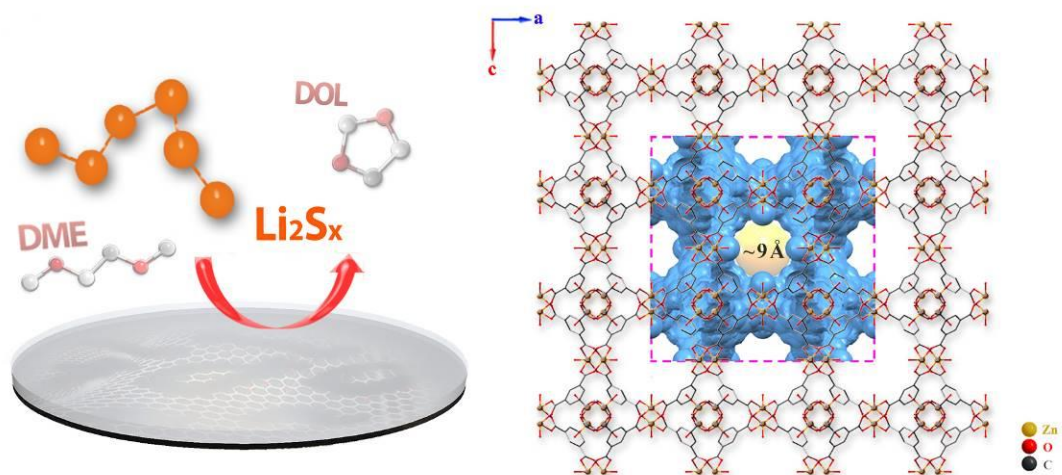
- (1) Due to metal-organic Frameworks (MOF) properties, we have attempted to utilize its high-ordered micropores for size effects. The chosen MOF illustrates the 3-dimensional open channels, with its intersecting pore diameter viewed along the (100) direction ranging around 9 Å, respectively. Because the length of every S-S chain of lithium polysulfide (Li<sub>2</sub>S<sub>n</sub>, 4 < n ≤ 8) ranged between 2.09 Å and 2.39 Å. The MOF-based separator, The MOF-based separator can act as a high-effective ionic sieve to block and separate these relatively larger polysulfide ions.
- (2) More importantly, to the best of our knowledge, this is the first report about a MOF-based separator in a lithium-sulfur battery. It can further open a door to a large family of MOF-based materials as separators for energy-storage applications.
- (3) Moreover, there is approximately no capacity fading after about 100 cycle. Its fading capacity was totally restricted within 15 mAh g<sup>-1</sup> in the range of 100th ~ 1,500th cycles, suggestive of negligible shuttle effects in this stage. Never has it been reported before with such record-high electrochemical performance in Lithium-Sulfur batteries.

In general, we present a metal-organic framework (MOF) based battery separator to mitigate the shuttling problem. We show that the MOF-based separator acts as an

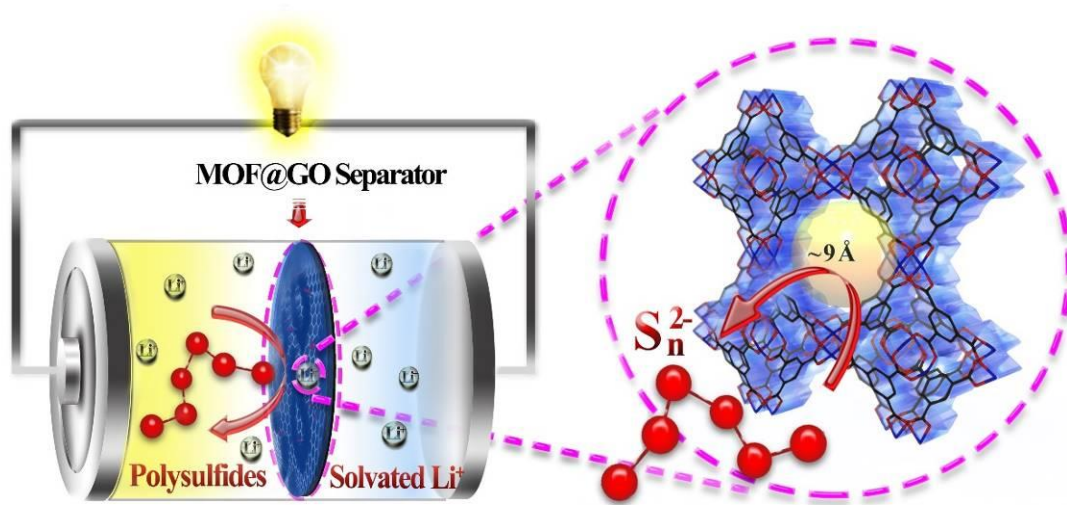
ionic sieve in lithium-sulfur batteries, which selectively sieves  $\text{Li}^+$  ions while efficiently suppressing undesired polysulfides migrating to the anode side. When a sulfur-containing mesoporous carbon material (approximately 70 wt% sulfur content) is used as cathode composites without elaborate synthesis or surface modification, a lithium-sulfur battery with a MOF-based separator exhibits a low capacity decay rate (0.019% per cycle over 1500 cycles). Moreover, there is approximately no capacity fading after the initial 100 cycles. Our approach demonstrates the potential for MOF-based materials as separators for energy storage applications.

## Appendix

### 1. Comprehensive understanding the advantageous effects of Zn-MOF@GO separator in lithium-sulfur batteries



2. Schematic mechanism of enhanced performance for Zn-MOF@GO separator in lithium-sulfur batteries.



## List of Research Results

### **JOURNAL PAPER**

First-author

[1] Songyan Bai, Xizheng Liu, Kai Zhu, Shichao Wu, Haoshen Zhou, “Metal-organic framework-based separator for lithium–sulfur batteries” *Nature Energy*, 2016,7,201694

[2] Songyan Bai, Kai Zhu, Shichao Wu, Yarong Wang, Jin Yi, Masayoshi Ishida, and Haoshen Zhou, “A long-life lithium-sulfur battery by integrating zinc-organic framework based separator” *Journal of Materials Chemistry A*, 2016, 4, 16812-16817

Co-authored

[1] Xizheng Liu<sup>1</sup>; De Li<sup>1</sup>, Songyan Bai and Haoshen Zhou, “Promotional recyclable Li-ion batteries by a magnetic binder with anti-vibration and non-fatigue performance” *Journal of Materials Chemistry A*, 2015, 3, 15403-15407

[2] Jin Yi; Shichao Wu, Songyan Bai, Yang Liu, Na Li and Haoshen Zhou, “Interfacial construction of Li<sub>2</sub>O<sub>2</sub> for a performance-improved polymer Li-O<sub>2</sub> battery” *Journal of Materials Chemistry A*, 2016, 4, 2403-2407

[3] Kai Zhu, Shaohua Guo, Jin Yi, Songyan Bai, Yingjin Wei, Gang Chen and Haoshen Zhou, “A new layered sodium molybdenum oxide anode for full intercalation-type sodium-ion batteries” *Journal of Materials Chemistry A*, 2015,3, 22012-22016

[4] Shichao Wu, Kai Zhu, Jing Tang, Kaiming Liao, Songyan Bai, Jin Yi, Yusuke Yamauchi, Masayoshi Ishida and Haoshen Zhou” “A long-life lithium ion oxygen battery based on commercial silicon particles as the anode” *Energy & Environmental Science*, 2016, 9, 3262-3271

### **PRESENTATIONS:**

[1] Songyan Bai, Haoshen Zhou, “The novel materials in rechargeable batteries with potential development”, International Conference on Green Energy and applications, Singapore, 2016 年, 03 月, 23 日-26 日 A0308 (oral)

## Acknowledgements

How time flies. It is the last moment for my doctor course...

First of all, I would like to offer my great thanks to my supervisor, Professor Haoshen Zhou, for his help and guidance without conservation. I wouldn't have completed my scientific research in my dissertation, without his recruit in his lab and the financial support. He is always encouraging me to conquer the culture gap, which helps me a lot in accommodating the daily life and academy in Japan. I can conduct many novel attempts in rechargeable batteries under his kind support and encouragement, because of the open-minded and motivated lab environment. In the last three years, I have learned much more in the field of energy-storing measurements.

I also want to express my grateful thanks to Professor Eunjoo Yoo, who has given me so much help on my graduation presentation. I also want to thank all the group members in Energy Interface Technology Group at AIST group members, Haijun Yu, Xizheng Liu, Kai Zhu, Shichao Wu, Jin Yi, Yarong Wang, Na Li, Yang Sun, Shaohua Guo, Kaiming Liao, Zhiping Song, Yang Liu and Qi Li, who help and support my research for their kind suggestions without hesitation. I would like also thank the Japanese staffs, Mr. Jun Okagaki and Hirokazu Kitaura et al, for their hard work.

Last but not least, I want to express my gratitude to my family members. My lovely wife, Jinying Liu, has sacrificed a lot for me in the last three years. Thank you very much. I also want to thank my father, mother and elder sister, who has worried a lot for my health and academic career. Right now, the most urgent thing I can't wait to do is to share my happiness with you. My dear family members, I did it. Thank you with my whole heart.